Centro de Investigación Científica y de Educación Superior de Ensenada, Baja California

Programa de Posgrado en Ciencias de la Tierra con Orientación en Geología

---

The interplay between deformation, erosion and sedimentation in the deep-water Mexican Ridges foldbelt, western Gulf of Mexico basin

Interacción entre deformación, erosión y sedimentación en el cinturón plegado de las Crestas Mexicanas, en el occidente del Golfo de México

Tesis

para cubrir parcialmente los requisitos necesarios para obtener el grado de

Doctor en Ciencias

Presenta:

Usama Ismael Yarbuh Lugo

Ensenada, Baja California, México

2015

Tesis defendida por

Usama Ismael Yarbuh Lugo

y aprobada por el siguiente comité

Dr. Juan Contreras Pérez
Director de tesis

Dr. Antonio González Fernández

Dr. Jesús Arturo Martín Barajas

Dr. Gustavo Tolson Jones

Dr. Ronald Michael Spelz Madero

Dr. Juan García Abdeslem
Coordinador del Posgrado en Ciencias de la Tierra

Dra. Rufina Hernández Martínez
Directora de Estudios de Posgrado

Abstract of the thesis presented by **Usama Ismael Yarbuh Lugo**, as a partial requirement to obtain the DOCTOR OF SCIENCE degree in EARTH SCIENCES, with orientation in GEOLOGY.

The Interplay Between Deformation, Erosion And Sedimentation In The Deep-Water Mexican Ridges Foldbelt, Western Gulf Of Mexico Basin

Abstract approved by:

_____

Dr. Juan Contreras Pérez
Director thesis

This study deals with a geometric and kinematic analysis that allowed us to derive the progression of the deformation of the Mexican Ridges fold belt (MRFB), western Gulf of Mexico. The database we used in this study was a high-resolution 2D seismic line of the MRFB, collected and processed by *Petróleos Mexicanos, Exploración y Producción* (PEMEX-PEP). Unlike previous studies that relied in stratigraphic relations to unravel fold kinematics, we use excess-area methods instead. From the excess-area plots for each of the folds comprising the MRFB, we estimate the shortening and the erosional degradation path of the seafloor deformed by folding. Previous authors analyzed stacking patterns of growth strata concluding deformation occurred in two stages that continue up to present times. While it is true that this contractional deformation system is still active, we conclude deformation started synchronously during the Late Miocene throughout the MRFB and not in two episodes as stated above. The reason for the seeming discrepancy is due to the copious sedimentation in the eastern section of the fold belt with respect to tectonic uplift. This hindered the development of onlap and thinning upward patterns that commonly signal the beginning of fold growth. During early fold growth, nearly constant thickness strata are deposited before a progressive unconformity develops. The delay, in turn, introduces a bias toward younger ages in the identification of the pregrowth/growth strata limit. Therefore, stacking geometries yield different values for the beginning of deformation depending on whether sedimentation rate is higher than uplift rate. We are also able to document changes of fundamental structural and kinematic parameters across this contractional system such as shortening and strain, tectonic uplift rate, sedimentation rate, and mass diffusion coefficient. Results indicate that in general these parameters decrease with distance from the continental slope to the distal part of the fold belt. In this study we also derive, from simple harmonic analysis, mathematical functions describing the folding process in the MRFB. From this analysis we obtain fold scaling laws and document the process of wavelength selection during fold development using Fourier transform. Fold growth is governed by two phenomena. One is the degree of amplification, and another is the selectivity of the amplification. Our results show that the MRFB involves two dominant wavelengths. One is the Biot's wavelength of ~ 9.4 km, and another one is a closely related secondary wavelength of ~ 8.0 km. Moreover, from Fourier analysis we observed that the amplitude of the fold train decreases with depth to the detachment surface, yet the maxima peaks in the spectra remain invariant with depth. The further spectral analysis carried out at a

structure scale, allowed us not only to derive the dominant wavelength of the folds independently, but also to establish, on one hand, the relationship between the amplitude and the depth to the detachment surface and, on the other hand, how amplitude relates to linear strain across the MRFB. Here, we were able to reconstruct the folding functions based on the values of the harmonic coefficients b_1, b_2 and b_3. From this analysis we derived two different fold shapes and deformation mechanisms involved in the formation of the MRFB. One is limb rotation by flexural slip folding, leading to pinched crest structures, namely cuspate-lobate anticlines, and another one is hinge migration leading to relatively low-strain sine-wave anticlines.

Keywords: Contractional deformation system, kinematics of deformation, fault-related folds, excess-area method, fold scaling laws, Fourier transform.

Resumen de la tesis de **Usama Ismael Yarbuh Lugo** presentada como requisito parcial para la obtención del grado de DOCTOR EN CIENCIAS en CIENCIAS DE LA TIERRA con orientación en GEOLOGÍA.

Interacción entre deformación, erosión y sedimentación en el cinturón plegado de las Crestas Mexicanas, en el occidente del Golfo de México

Resumen aprobado por:

_____

Dr. Juan Contreras Pérez
Director de tesis

En este trabajo se realizó un análisis geométrico y cinemático del cinturón plegado de las Crestas Mexicanas de aguas profundas (CPCM), en el occidente del Golfo de México, y así estimar la progresión de la deformación en este importante sistema de deformación contraccional. La base de datos que se utilizó para llevar a cabo este estudio es una línea sísmica de alta resolución en dos dimensiones del CPCM, adquirida y procesada por Petróleos Mexicanos, Exploración y Producción (PEMEX-PEP). A diferencia de estudios anteriores, que utilizaron patrones de apilamiento y otras relaciones estratigráficas, aquí se usa el método de exceso de área para cada una de las estructuras que conforman el CPCM. De los diagramas de exceso de área se logró estimar el acortamiento, el comienzo de la deformación y la degradación del fondo marino plegado. Autores anteriores analizaron los patrones de apilamiento de los estratos de crecimiento concluyendo que la deformación ocurrió en dos etapas y que el crecimiento de los pliegues continúa hasta la actualidad. Si bien se sabe que este sistema de deformación se encuentra aún activo, nuestros resultados muestran que la deformación comenzó sincrónicamente durante el Mioceno tardío en todo el CPCM y no en dos episodios. La razón de la discrepancia se debe a la copiosa sedimentación en la sección oriental del cinturón plegado respecto a la tasa de levantamiento tectónico. Esto impide el desarrollo de geometrías de adelgazamiento de capas y/o superficies tipo “onlap" hacia las crestas de los pliegues, fenómeno que comúnmente se utiliza como criterio para identificar el comienzo de la deformación. Durante el inicio de la deformación y crecimiento de pliegues, estratos de espesor casi constantes son depositados previo a la ocurrencia de una discordancia progresiva. Este retraso, a su vez, puede introducir sesgos hacia edades más jóvenes en la identificación del límite de los estratos de pre-crecimiento/crecimiento. Por lo tanto, las geometrías de apilamiento pueden producir diferentes valores en la estimación del inicio de la deformación. Nuestro análisis indica que la diferencia es función de la velocidad de sedimentación y la tasa de levantamiento. También se pudieron documentar los cambios de parámetros estructurales y cinemáticos fundamentales a través de este sistema compresivo, tales como el acortamiento y la distorsión, la tasa de levantamiento tectónico, la velocidad de sedimentación y el coeficiente de difusión de masa. Los resultados indican que en general estos parámetros disminuyen con la distancia desde el talud continental a la parte distal del cinturón plegado. En este estudio también se derivaron, a partir de

análisis armónico, funciones matemáticas que describen el proceso de plegamiento en el CPCM. Este análisis permitió derivar leyes de escalamiento que describen el crecimiento de los pliegues, y se documenta el proceso de selección de la longitud de onda durante el desarrollo de pliegues utilizando la transformada de Fourier. En general, el crecimiento del pliegue se rige por dos fenómenos: (1) el grado de amplificación, y (2) la selectividad de la amplificación. Los resultados muestran que en el CPCM se encuentran involucradas dos longitudes de onda dominantes. Una de ellas es la longitud de onda de Biot de ~ 9,4 km, y otra es una longitud de onda secundaria de ~ 8.0 km. Adicionalmente, a partir del análisis de Fourier se observó que la amplitud del tren disminuye con la profundidad de la superficie de despegue. Sin embargo, los picos máximos en los espectros se mantienen invariables con la profundidad. El análisis espectral llevado a cabo a escala de estructura, permitió derivar la longitud de onda dominante de los pliegues de forma independiente; además de establecer, por un lado, la relación entre la amplitud y la profundidad de la superficie de despegue y, por otra parte, cómo se relaciona la amplitud con la distorsión lineal a través del CPCM. De esta manera, se reconstruyeron las funciones de plegamiento basados en los valores resultantes de los coeficientes armónicos b_1, b_2 y b_3. A partir de este análisis se derivaron dos formas diferentes de pliegues y mecanismos de deformación involucrados en la formación del CPCM. Una de ellas es por rotación de los flancos de los pliegues por deslizamiento flexural, lo que genera estructuras con crestas apretadas, llamados pliegues cuspados-lobados, y otra es por migración de la charlena de los pliegues, lo que genera anticlinales de onda sinusoidal de baja distorsión relativa.

Palabras clave: Sistema de deformación contraccional, cinemática de la deformación, pliegues relacionados con fallas, método de exceso de área, leyes de escalamiento en pliegues, transformada de Fourier.

Dedication

This work is dedicated to…

the memory of my father Luis N. Yarbuh
my mother Ana Lugo
my brothers Omar and Anuar
my daughter Arianna Valentina
my sister in law Guadalupe A. de Yarbuh
my niece Firuze
my nephews Nauaf and Farid

Acknowledgements

I am grateful to my advisor Juan Contreras Pérez for the remarkable job during the development of this PhD project.

I am also grateful to my thesis committee, Antonio González Fernández, Jesús Arturo Martín Barajas, Gustavo Tolson Jones, and Ronald Michael Spelz Madero.

This research was supported by the National Council of Science and Technology of Mexico (CONACYT), which provided the author the scholarship No. 257044 as part of his PhD project.

I am also grateful to Petróleos Mexicanos Exploración y Producción (PEMEX-PEP) for providing the seismic section of the Mexican Ridges foldbelt, Gulf of Mexico.

I would like to thank Max Suter who was involved in the early stages of this research.

I am also thankful to my colleagues Karla Lara, Gina Villalobos, Claudia Quinteros, Andrea Lotero, Mario Fuentes, Armando Calderon, Clemente Gallardo, José Mojarro, and Sergio Arregui, for helpful advise during the development of this thesis.

Finally, I would like to thank reviewers François Roure, Rick Groshong and Nicolas Bellahsen for their thoughtful suggestions that improved significantly a paper submitted to Basin Research for its publication.

Table of content

List of figures

List of tables

Chapter 1

Synopsis (Spanish)

1.1. Introducción

En el margen pasivo al oeste del Golfo de México (GDM) se ha desarrollado un extenso sistema de fallas normales gravitacionales a lo largo de toda su plataforma continental (Fig. 1). Estas convergen a profundidad en una serie de superficies de despegue localizadas sobre capas salinas de edad Jurásico y lutitas sobrepresurizadas de edad Oligoceno (Rowan, 1997; Trudgill et al., 1999; Alzaga-Ruíz et al., 2009). Las superficies de despegue transfieren el movimiento normal del sistema extensional en un movimiento de contracción paralelo a la estratificación. Esto da como resultado que los sedimentos siliciclásticos del Neógeno sean desacoplados de las sucesiones subyacentes del Paleógeno y carbonatos del Mesozoico, formando así una serie de cinturones plegados de aguas profundas a lo largo del talud continental (Fig. 1).

1.2. Evolución tectónica y sedimentaria del Golfo de México

La etapa inicial de la fragmentación y separación de la Pangea para formar el GDM duró del orden de unos 46 Ma, desde el Triásico Tardío (210 Ma) hasta el Jurásico Medio Tardío (169 Ma) (Salvador, 1991). Este evento se puede evidenciar por la presencia de sedimentos lutíticos continentales que fueron depositados en grabenes estrechos aproximadamente paralelas a la actual línea de costa (Salvador, 1991). El proceso tectónico de Pangea prevaleció hacia el inicio del Jurásico Superior, época en la cual la sedimentación continental estuvo totalmente controlada por procesos tectónicos distensivos. El avance transgresivo de las aguas del pacífico hacia el oriente fue invadiendo el área del actual GDM para formar extensos cuerpos de aguas hipersalinas, con una circulación sumamente restringida y, quizá también un clima de tipo desértico, lo que favoreció el depósito de grandes volúmenes de evaporitas (Trudgill et al., 1999).

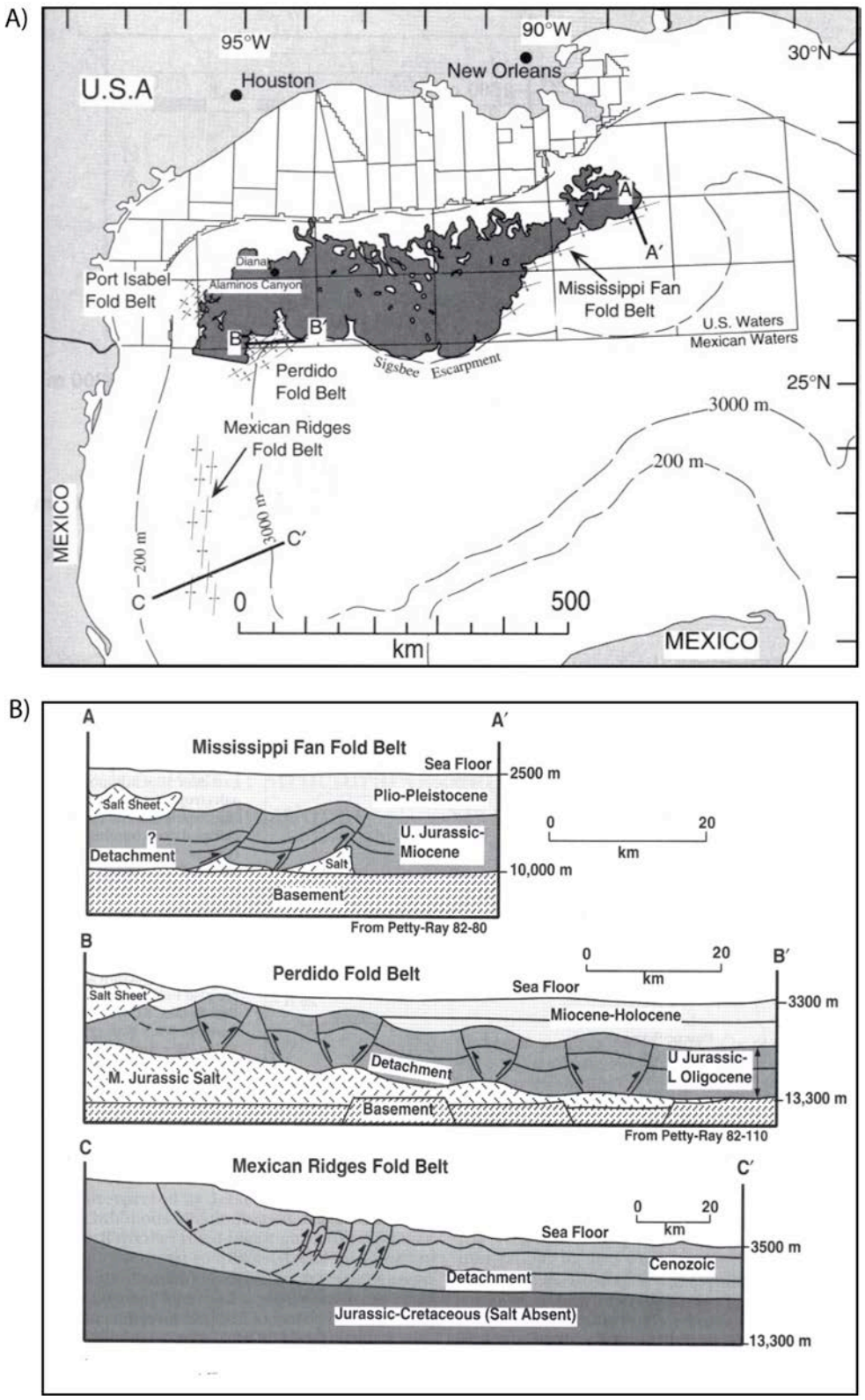

Figura 1. (A) Mapa regional de la porción noroccidental del Golfo de México, que muestra los cinturones plegados del Cenozoico y la extensión de sal alóctona (región gris oscuro); y (B) secciones transversales esquemáticas basado en datos sísmicos regionales del cinturón plegado del Abanico del Mississippi (sección AA'), el cinturón plegado de Perdido (sección BB') y el cinturón plegado de las Crestas Mexicana (seeción CC'). Modificado de Trudgill et al. (1999).

Después del episodio de extensión Jurásica y la apertura del GDM, numerosas plataformas carbonatadas se desarrollaron a lo largo del margen occidental del GDM durante la fase de subsidencia térmica, que progradaron hacia los dominios de cuencas adyacentes. Durante el Cretácico-Paleoceno tardío, la inversión de cuencas por el levantamiento de la Sierra Madre Oriental resultó en levantamiento tectónico y erosión de las unidades alóctonas. Este evento dio origen a una fuente importante de sedimentos que alimentaron la antefosa del sistema plegado, donde la carga litostática produjo la flexión de la litosfera en el antepaís.

A partir del Paleoceno, los sedimentos erosionados de la Sierra Madre Oriental fueron transportados hasta la cuenca del Golfo de México, donde la sedimentación clástica se fue alojando en grandes depocentros formados en el antepaís de la Sierra Madre Oriental y en las porciones sur y suroccidental del Golfo de México, en donde el Macizo de Chiapas aportó un gran volumen de sedimentos, mientras que sobre el Bloque Yucatán continuaba el depósito de carbonatos de plataforma somera (Roure et al., 2009).

La carga litostática y el flujo de los cuerpos de sal, trajo como resultado el desarrollo de un colapso gravitacional generalizado en el margen occidental y noroeste del Golfo de México. Sin embargo, otros autores han propuesto un control más profundo de la corteza terrestre en la dinámica del colapso gravitacional debido a una inversión de fallas de basamento, o incluso por convección del manto profundo, induciendo un basculamiento regional post-Laramídico de la litosfera de América del Norte (Leroy et al., 2008; Leroy y Rangin, 2008; Rangin et al., 2008; Roure et al., 2009).

1.3. Origen y evolución del cinturón plegado de las Crestas Mexicanas, en el occidente del Golfo de México.

Un ejemplo particular del amplio sistema de deformación contraccional en el GDM, es el cinturón plegado de las Crestas Mexicanas (CPCM), localizado frente a las costas del estado de Veracruz, en el cual el acortamiento principal se concentra las sucesiones Terciarias del talud continental, por encima de una zona de despegue basal compuesta por lutitas sobrepresurizadas del Paleógeno (Bryant et al., 1968; Garrison y Martin,

1973; Buffler et al., 1979; Alzaga-Ruiz et al., 2009; Salomón-Mora et al., 2009). Al oeste del cinturón, en la transición plataforma-talud continental, estas superficies de despegue actúan simultáneamente como una serie de fallas lístricas gravitacionales, que disectan los sedimentos de la plataforma continental de Tuxpan (Fig. 2). Este fenómeno dio origen al sistema extensional de Quetzalcóatl (SEQ) y a su contraparte compresional, el CPCM, durante el Mioceno, en la transición entre el talud continental y la planicie abisal (Román-Ramos et al., 2001, 2004). Entre las fallas normales de alto ángulo en el oeste y los anticlinales en el este, una amplia estructura tipo monoclinal de ~15 km de largo ha crecido progresivamente, dando lugar a un importante salto topográfico en la morfología del perfil del talud continental (Salomón-Mora et al., 2004).

Alzaga-Ruíz et al. (2009) y Salomón-Mora et al. (2009) utilizaron información de nueve pozos ubicados en la plataforma continental de Tuxpan para establecer la cronoestratigrafía de las sucesiones despegadas. Por otra parte, Vázquez-Meneses (2005), realizó un análisis detallado de la estructura de la velocidad sísmica del CPCM, mostrando que la estructura de velocidad es bastante homogénea con la profundidad. Los sedimentos siliciclásticos muestran intervalos de velocidad del orden de 2000 m/s, mientras que los carbonatos del Mesozoico muestran intervalos de velocidad de 3100 m/s. Sin embargo, hay una gran incertidumbre con respecto a las edades de las secuencias sísmicas en la parte oriental del CPCM debido a que no se cuenta con datos de perforación que permitan correlacionar los datos sísmicos con la estratigrafía disponible en la plataforma continental. A pesar de esto, Bryant et al., 1968; Garrison y Martin, 1973; Buffler et al., 1979; Alzaga-Ruiz et al., 2009; Salomón-Mora et al., 2009, lograron establecer la sismoestratigrafía con base en el carácter sísmico, la continuidad y la geometría interna de las sucesiones sedimentarias depositadas en la planicie abisal del GDM. Al igual que con la datación de las secuencias sísmicas, la litología de estas secuencias esta pobremente constreñida (Salomón-Mora et al., 2009). Se piensa que las secuencias estratigráficas consisten de sedimentos siliciclásticos del Neógeno, en su mayoría sedimentos turbidíticos hemipelágicos. Estas sucesiones siliciclásticas se desacoplaron de los carbonatos infrayacentes del Mesozoico, a lo largo de dos niveles estratigráficos: una zona basal de rocas arcillosas sobrepresurizadas de edad Paleógeno y otra secuencia lutítica a lo largo del límite Mioceno-Oligoceno (Alzaga-Ruíz et al., 2009).

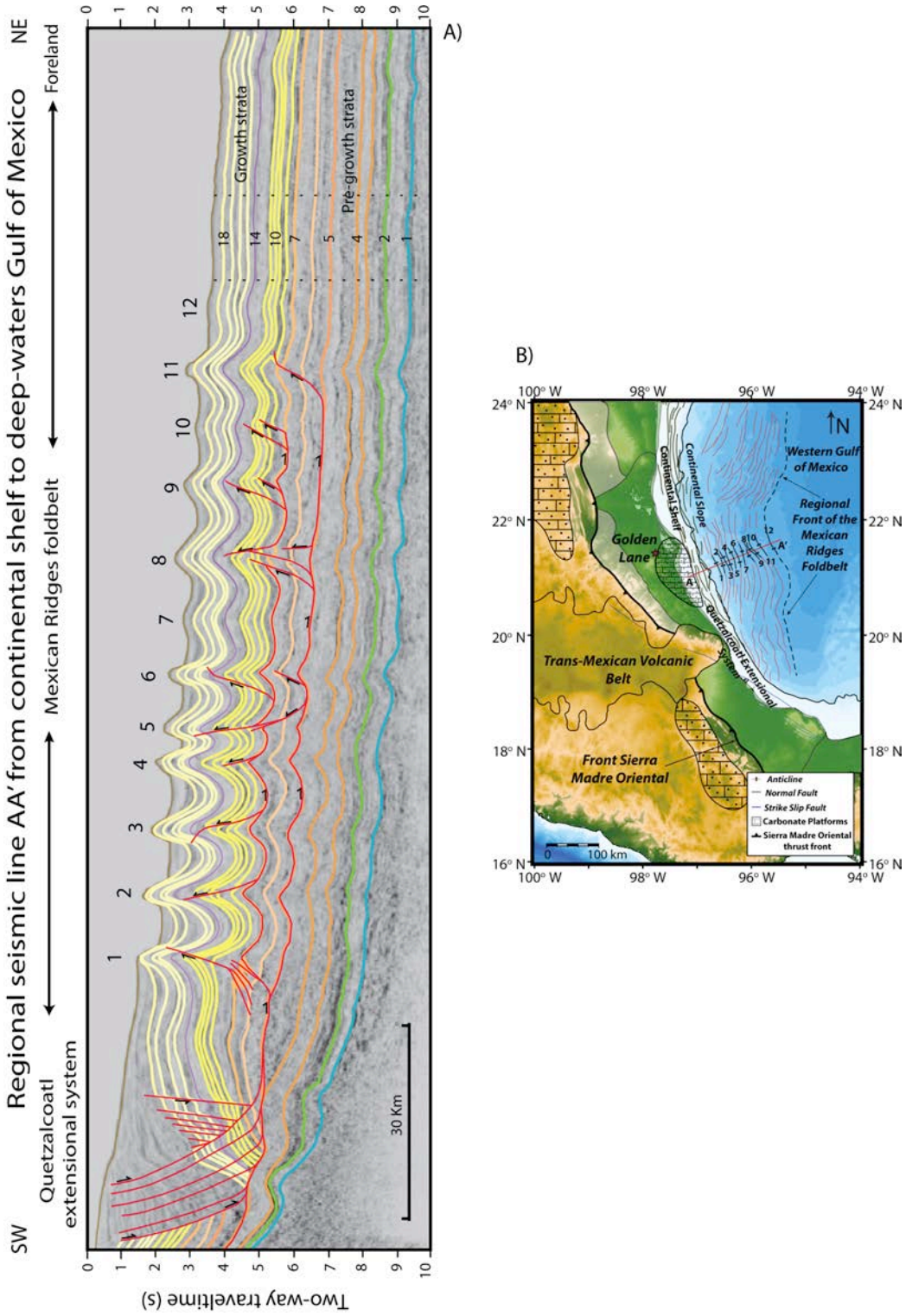

Figura 2. (A) Sección sísmica AA' a lo largo del cinturón plegado de las Crestas Mexicanas, al occidente del Golfo de México. La sección comprende una longitud horizontal de 180 km y tiene una penetración de 10 s de doble tiempo de viaje. El sistema extensional de Quetzalcóatl consiste en una serie de fallas normales que cortan a la plataforma continental. Este sistema extensional es la fuente de una serie de anticlinales en el talud continental. (B) Mapa de los elementos estructurales de la porción suroccidental del Golfo de México. La sección AA' corresponde a una sección sísmica del cinturón plegado de las Crestas Mexicana mostrado en (A). La línea sísmica tiene una exageración vertical de 1:3.5. Modificado de Le Roy et al., 2008.

Independientemente de las incertidumbres temporales, y con base en su estilo de deformación y geometría de apilamiento, se pueden identificar dos sucesiones estratigráficas en los sedimentos depositados por encima de la superficie de despegue basal en el CPCM: (1) estratos de pre-crecimiento, depositados antes del comienzo de la deformación, y (2) estratos de crecimiento depositados de forma sincrónica durante el plegamiento de estas estructuras. El primer paquete sedimentario se puede reconocer en el perfil sísmico como una serie de reflectores deformados por cizalla pura heterogénea formando pliegues similares, mientras que el paquete de sedimentos suprayacente muestra geometrías de adelgazamiento de capas y/o superficies tipo "onlap" hacia las crestas de los pliegues (Suppe, 1992; Hardy y Poblet, 1995; Poblet et al., 1997, 2004; Contreras, 2010). A partir de estas relaciones estratigráficas, Salomón-Mora et al. (2009) concluyeron que las estructuras más antiguas se desarrollaron en la parte occidental del CPGM, cerca del SEQ, y que se corresponden con edades del Mioceno tardío, seguido por el levantamiento de estructuras en la parte oriental del cinturón durante el Plioceno temprano. Estos autores también concluyeron que la deformación es activa y que los pliegues más recientes se están formando en las partes central y oriental del cinturón (véase también Suter, 1991).

La presente tesis esta dividida en cinco capítulos. El primer capítulo presenta una sinopsis en español; el capitulo 2 presenta una introducción a la arquitectura de los sistemas de deformación compresional; el capitulo 3 trata sobre la cinemática y dinámica de la sedimentación y erosión en el CPCM, en el occidente del GDM; el capitulo 4 trata sobre las leyes de escalamiento en pliegues y la selección de la longitud de onda en inestabilidades por plegamiento usando series de Fourier; en el capitulo 5 se presentan las conclusiones generales de la tesis.

1.4. Objetivos

1.4.1. Objetivos generales

- Determinar la cinemática y la dinámica de la sedimentación y erosión en el cinturón plegado de las Crestas Mexicanas, en el occidente del Golfo de México.

- Derivar las leyes de escalamiento en pliegues y la selección de la longitud de onda en inestabilidades por plegamiento usando series de Fourier.

1.4.2. Objetivos específicos

- Cuantificar el exceso de área que se produce en los estratos de pre-crecimiento y estratos de crecimientos en el CPCM, a partir de una sección sísmica de alta resolución en dos dimensiones.

- Establecer la evolución temporal y espacial de todo el sistema compresivo.

- Determinar las tasas de transporte de masa superficial a escala de cinturón plegado.

- Realizar un análisis armónico para predecir la forma de los pliegues y su cinemática de deformación.

- Derivar funciones matemáticas que describan el proceso de plegamiento en el CPCM

- Documentar el proceso de selección de longitud de onda durante el desarrollo de pliegues utilizando la transformada de Fourier.

1.5. Cinemática y dinámica de la sedimentación y erosión en el cinturón plegado de las Crestas Mexicanas, en el occidente del Golfo de México.

En este estudio se presenta un análisis de la interacción entre la deformación, la erosión y la sedimentación en el CPCM, en el margen occidental del GDM. Se cuantifica el exceso de área que se produce en los estratos de pre-crecimiento y estratos de crecimientos en una sección sísmica de alta resolución (Chamberlin, 1910; Epard y Groshong, 1993; Groshong y Epard, 1994; Bulnes y Poblet, 1999 y referencias ahí citadas). Utilizando la información cronoestratigráfica reportada en la literatura (*e.g.*

Salomón-Mora et al., 2009; Alzaga-Ruíz et al., 2009), se derivó la tasa de cambio promedio de acortamiento para cada uno de los pliegues desde el Mioceno tardío hasta la actualidad. Con esta información, se estableció la evolución temporal y espacial de este sistema compresivo. También se obtuvieron las tasas de transporte de masa superficial a escala de cinturón plegado. Se sabe que la tasa de flujo por unidad de área de las partículas sedimentarias ejerce un control primario sobre la arquitectura de los ambientes de formación de cuencas sedimentarias y regula la depositación de sucesiones sintectónicas. A pesar de su importancia, poco se sabe acerca de cómo el flujo de sedimentos varía con los procesos morfotectónicos y con las escalas de tiempo de sedimentación (Tucker y Slingerland, 1996; Allen y Heller, 2012, y referencias ahí citadas). En este análisis también se identifica el tiempo de retraso entre el inicio del levantamiento del CPCM y la subsecuente respuesta sedimentaria, lo que permite establecer con precisión el comienzo de la deformación en este sistema compresivo. Se muestra también que el retraso observado está controlado por el suministro de sedimentos hacia la cuenca, la tasa de levantamiento tectónico y la velocidad a la que la topografía plegada es degradada. Los resultados obtenidos a partir del análisis fueron validados utilizando el paquete de computo THRUST (Contreras, 2002, 2010) que simula tanto la deformación por compresión como por extensión y genera secciones transversales balanceadas.

Este trabajo es motivado por los resultados obtenidos por González-Mieres y Suppe (2006) y Hubert-Ferrari et al. (2007). Basado en el principio general de la mecánica del medio continuo de la conservación de la masa y el método de exceso de área, estos autores lograron cuantificar parámetros fundamentales de deformación, como son el acortamiento y la distorsión lineal, para una serie de pliegues aislados en varios cinturones de pliegues y cabalgaduras en todo el mundo. En este estudio se lleva a cabo un análisis similar para cada uno de los anticlinales que componen el CPCM, lo que permite documentar con gran precisión los cambios espaciales de la deformación a través de este importante sistema compresivo.

Pocos estudios han abordado el problema del tiempo de retraso de la depositación sintectónica en cuencas sedimentarias. En los pocos casos de estudio disponibles, los tiempos de retraso entre la ocurrencia de un evento de deformación y la respuesta

sedimentaria en estado estacionario son del orden de 10^5-10^6 años (Allen y Heller, 2012 y referencias ahí citadas). Dado que la amplificación de pliegues y su cinemática a menudo son inferidos por la geometría de los estratos de crecimiento (Suppe et al., 1992; Holl y Anastasio, 1993; Poblet, 2012 y referencias ahí citadas), los tiempos de retraso asociados con su depositación pueden distorsionar la cronología de los eventos inferidos.

1.5.1. Interpretación sísmica

En este trabajo se analizó un perfil sísmico regional del CPCM en el oeste del GDM. Los datos sísmicos fueron recolectados y procesados por Petróleos Mexicanos, Producción y Exploración (PEMEX-PEP). El perfil sísmico muestra tanto el QES como el MRFB; su extensión lateral es de ~170 km, tiene una penetración de ~10 s de tiempo doble de viaje (TDV) y está orientada NE-SW, perpendicular al fallamiento regional (Fig. 2). Para la conversión a profundidad de los datos sísmicos se utilizando intervalos de velocidades que han sido validados en estudios anteriores y en pozos en la plataforma continental del oeste del GDM (Vázquez-Meneses, 2005 y referencias ahí citadas). En el cinturón plegado que muestra la línea sísmica se pueden observar doce pliegues relacionados con fallas. De la línea sísmica se interpretaron veintidós reflectores de gran amplitud con buena continuidad lateral. Estos horizontes fueron numerados de la base a la cima, para luego asignar edades con base en la cronoestratigrafía propuesta por Salomón-Mora et al. (2009) y Alzaga-Ruíz et al. (2009). Asimismo, al igual que estos autores, se asumió que los horizontes sísmicos son límites de secuencia y por lo tanto se pueden considerar como líneas de tiempo estratigráficas. Preliminarmente, los reflectores 5-15 fueron asignados como estratos de pre-crecimiento, mientras que los horizontes 16-22 fueron asignados como sucesiones sintectónicas.

Los horizontes sísmicos interpretados fueron exportados a una serie de archivos de texto con la posición geográfica y la profundidad en TDV. Los reflectores se analizaron mediante una serie de programas de cómputo con rutinas de integración numérica y otros algoritmos de mínimos cuadrados que permitieron implementar el método de exceso de área. Por lo tanto, nuestros resultados son independientes de cualquier exageración vertical.

1.5.2. Método de exceso de área

El método de exceso de área (Epard y Groshong, 1993; Groshong y Epard, 1994; Bulnes y Poblet, 1999 y referencias citadas) se aplicó a cada estructura comenzando con los estratos de los carbonatos de aguas profundas identificados por Salomón-Mora et al. (2009), hasta el reflector del fondo marino. El método de exceso de área ayuda a verificar si una sección estructural está balanceada y proporciona información independiente acerca de la profundidad del nivel de despegue, el acortamiento y la distorsión lineal (Schlische et al., 2014). Este método se ha aplicado a pliegues relacionados con fallas en los anticlinales Tip Top en Wioming, USA, los anticlinales de Yaken, al sur de Tian Shan, India, entre otros (Epard y Groshong, 1993; Groshong y Epard, 1994; González-Mieres y Suppe, 2006, 2011; Hubert-Ferrari et al., 2007; Groshong et al., 2012; Wiltschko y Groshong, 2012). Como se muestra más adelante, este método también permite subdividir la estratigrafía en estratos de pre-crecimiento y estratos de crecimiento independientemente de la geometrías estratigráfica, el cual permite identificar el límite que marca objetivamente el inicio de la deformación.

El método de exceso de área utiliza las mediciones del área levantada, A_e, de un horizonte marcador *vs.* la profundidad por debajo de un nivel de referencia, h_0, para múltiples horizontes. En un diagrama de A_e *vs.* h (Fig. 3), los estratos de pre-crecimiento se ajustan formando una línea recta en donde el acortamiento u es el inverso de la pendiente de una ecuación lineal de mejor ajuste $h = m\,A_e + b$ (Epard y Groshong, 1993; Groshong y Epard, 1994; González-Mieres y Suppe, 2006; Hubert-Ferrari et al., 2007), donde m es la pendiente del modelo lineal y b (la ordenada al origen) es la profundidad de la superficie de despegue basal, h, por debajo del nivel de referencia h_0.

Dado que u es calculado a partir de una regresión lineal, se reporta en los diagramas valores del coeficiente de determinación, R^2, un parámetro estadístico que indica qué tan bien se ajustan los modelos a los datos; de esta manera, $R^2 = 1$ indica que el modelo lineal explica toda la variabilidad en los datos, mientras que un valor de cero indica que no existe relación entre la variable de respuesta (A_e) y el regresor (h).

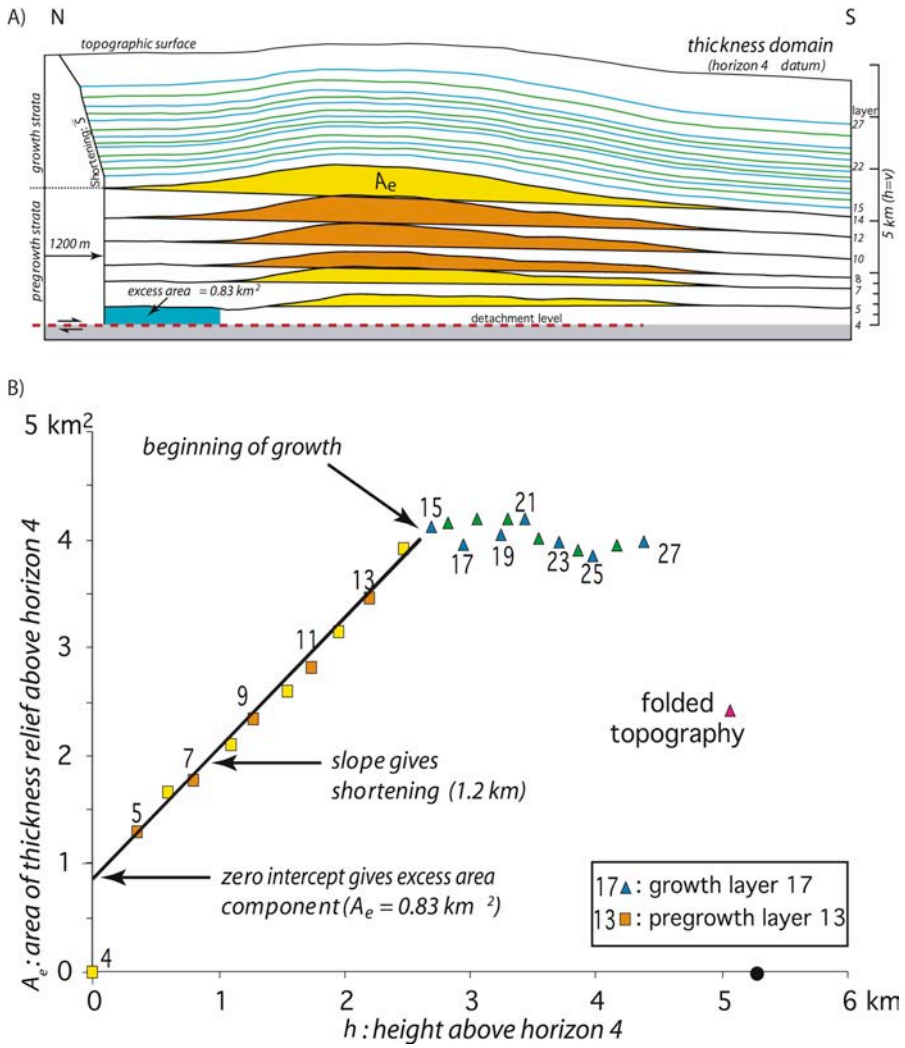

Figura 3. El método de exceso de área. (A) Interpretación de los anticlinales de Yaken, al sur de Tian Shan, India. (B) El área bajo la curva de las capas levantadas, A_e, se grafican en un diagrama *vs.* la altura sobre el nivel de despegue, *h*. Modificado de Hubert-Ferrari et al., 2007.

Si la sedimentación sintectónica es continua durante el proceso de amplificación de los pliegues, entonces los estratos de crecimiento proporcionarán un registro completo de la evolución estructural de los pliegues relacionados con fallas y su degradación. A pesar de que la depositación de los estratos de crecimiento está controlada por muchos factores, incluyendo la sedimentación y la tasa de levantamiento tectónico, erosión, subsidencia y la cinemática de los pliegues, entre otros (Hardy y Poblet, 1995), las sucesiones sintectónicas se caracterizan por dos rasgos principales. En primer lugar, las capas tienden a adelgazarse por encima de los altos estructurales (crestas o anticlinales) y se hacen más gruesos en las depresiones (valles o sinclinales). En segundo lugar, los estratos de crecimiento están generalmente menos plegadas que las

capas correspondientes a los estratos de pre-crecimiento. Estas características hacen que el límite entre los estratos de precrecimiento y los estratos de crecimiento sea fácil de reconocer en los diagramas A_e *vs.* h. Dado que los estratos sintectónicos están menos plegados que las secuencias pre-cinemáticas, el exceso de área crece más lentamente, lo que se traduce en un cambio en la pendiente de la relación lineal entre A_e y h (González-Mieres y Suppe, 2006; Hubert-Ferrari et al., 2007; Poblet et al., 2004).

1.5.3. Estimación del inicio de la deformación, tasas de levantamiento tectónico, tasas de sedimentación y degradación del fondo marino

Una vez que se identifica el límite entre los estratos de pre-crecimiento y los estratos de crecimiento, otro parámetro cinemático importante, el comienzo de la deformación, t_u, puede estimarse a partir de la cronoestratigrafía de los estratos de crecimiento y puede ser utilizado para estimar la tasa de levantamiento tectónico, v_u, y la tasa de sedimentación, s.

En nuestros análisis, la tasa de sedimentación contiene las contribuciones tanto de fuentes de sedimentos distales como locales producto de la degradación de las crestas de los pliegues. Para cuantificar este último efecto, se utiliza un modelo de difusión de la evolución topográfica en el que el transporte de masa superficial, j_m (flujo de sedimentos por unidad de área), es proporcional al gradiente de la topografía, donde el modelo de degradación esta limitado por la erosión de las crestas de los pliegues hacia los flancos del mismo (Culling, 1963; Carson y Kirkby, 1972).

1.6. Leyes de escalamiento en pliegues y la selección de la longitud de onda en inestabilidades por plegamiento usando series de Fourier.

Los pliegues son estructuras que se presentan por lo general en los sistemas de deformación por compresión. En un principio los pliegues presentan flancos de bajo ángulo, con una relación amplitud/longitud-de-onda pequeña. Conforme el acortamiento aumenta, las rocas dúctiles fluyen hacia el núcleo de la estructura, dando paso a la rotación de los flancos y a un aumento del ángulo de buzamiento de los mismos, aumentando así la razón amplitud/longitud-de-onda de las estructuras (Biot, 1961).

El análisis armónico es una herramienta robusta que se utiliza para predecir la forma de los pliegues y su cinemática de deformación (Biot, 1961; Norris, 1963; Harbaugh and Preston, 1965; Whitten, 1966; Chapple, 1968; Stabler, 1968; Hudleston, 1973; Stowe, 1988; Singh and Gairola, 1992; Srivastava and Gairola, 1997; Bastida et al., 1999; Fossen, 2010). La curva que describe una superficie plegada puede ser contrastada contra funciones matemáticas periódicas caracterizadas por términos geométricos como la amplitud y la longitud de onda. La transformada de Fourier es el procedimiento matemático que descompone una función en las frecuencias que integran dicha función. Esta metodología ha sido utilizada para cuantificar el proceso de plegamiento, con el cual contrasta los llamados modelos de juguete, en el sentido de que tratan de reducir el crecimiento de pliegues a su comportamiento esencial (Suppe, 2011 y referencias ahí citadas). Estos modelos numéricos no tratan de incluir todas las complejidades y las formas reales de los pliegues, sino que más bien se concentran en el estudio de las formas simplificadas de la ecuación de balance de masa en estos sistemas de deformación compresional ($A_e = u \times h$).

En este estudio se realiza un análisis de Fourier de la sección sísmica estudiada con el método del exceso de área descrito en la sección 1.5 (Bryant et al, 1968; Garrison y Martin, 1973; Buffler et al, 1979;. Alzaga-Ruiz et al, 2009; Salomón-Mora et al, 2009; Yarbuh y Contreras, 2015) y se derivan a partir del análisis armónico funciones matemáticas que describen el proceso de plegamiento en el CPCM, documentando el proceso de selección de la longitud de onda durante el desarrollo de pliegues. Las leyes de escalamiento son relaciones simples que muestran el comportamiento de las diferentes variables de un sistema en función de otros parámetros que describen su tamaño o forma. A pesar de su simplicidad, estas relaciones pueden capturar muchos de los atributos esenciales de un sistema que a primera vista podrían parecer complejos. En general, las leyes de escalamiento en pliegues permiten determinar los cambios en el estado de las secuencias estratigráficas que ocurren durante el crecimiento de los pliegues mismos.

El análisis armónico se realizó utilizando los datos sísmicos de la sección de estratos de precrecimiento descrita en la sección 1.5. Las sucesiones estratigráficas sometidas a análisis de Fourier corresponden a la sección de los estratos numerados de S_1 a S_9,

donde S_1 es el horizonte superior que marca el límite entre los estratos de pre-crecimiento y los estratos de crecimiento y S_9 es la superficie de despegue basal (Fig. 4). Las series espaciales tienen una extensión de 104 km de longitud y en conjunto forman una sección transversal de ~4 s de profundidad en TDV.

El análisis espectral se llevó a cabo de dos maneras diferentes: (1) un análisis armónico general a escala de todo el CPCM; y (2) un análisis espectral para cada uno de los pliegues individuales que conforman el CPCM. Esta última permite no sólo derivar la longitud de onda dominante de los pliegues de forma independiente, sino también establece, por un lado, la relación entre la amplitud, R_s, y la profundidad a la superficie de despegue, h, y, por otra parte, cómo R_s se relaciona con la distorsión lineal, ε_x, en todo el CPCM. Los valores de ε_x para cada estructura se derivan en el capítulo 3 de la presente tesis.

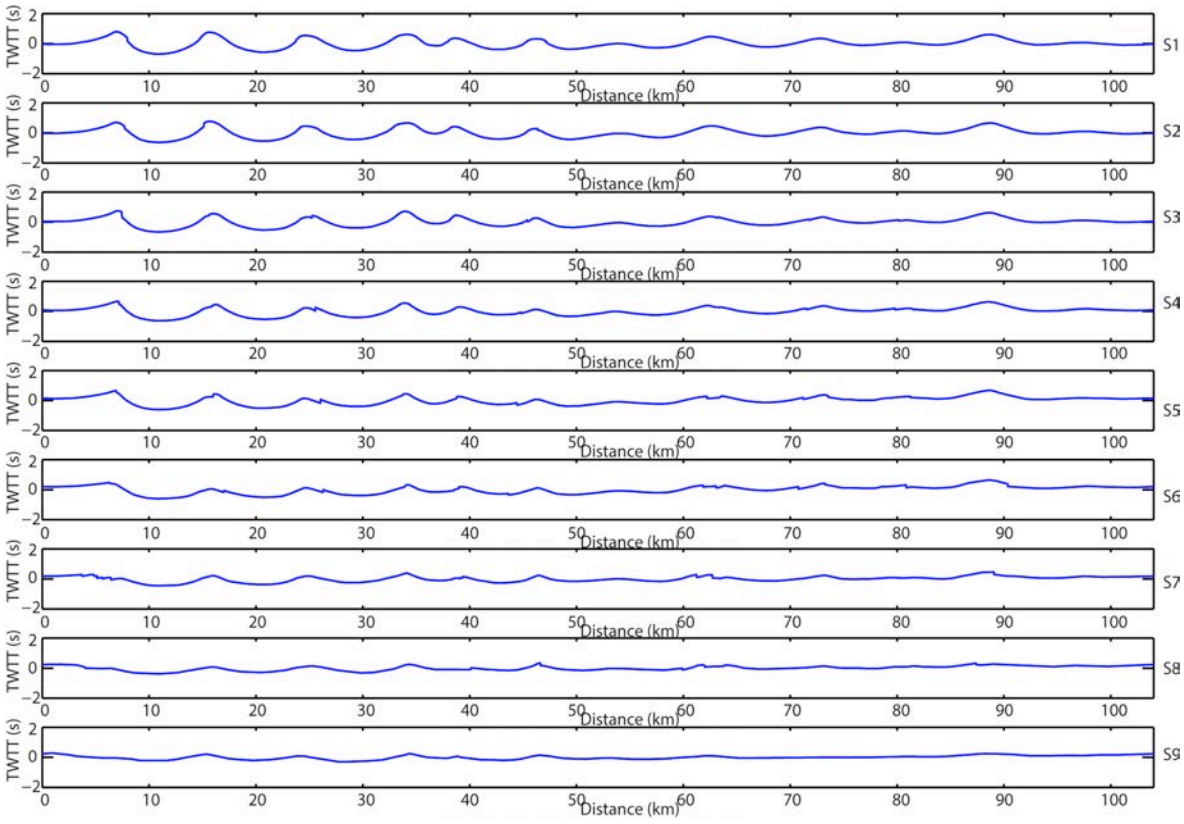

Figura 4. Horizontes sometidos a análisis de Fourier. Los horizontes están numerados de S_1 a S_9.

Además de este análisis, también se utilizaron los coeficientes de Fourier resultantes b_1, b_2 y b_3 para establecer la geometría general de los anticlinales basada en la clasificación de los pliegues propuestas por Hudleston (1973; Fig. 5).

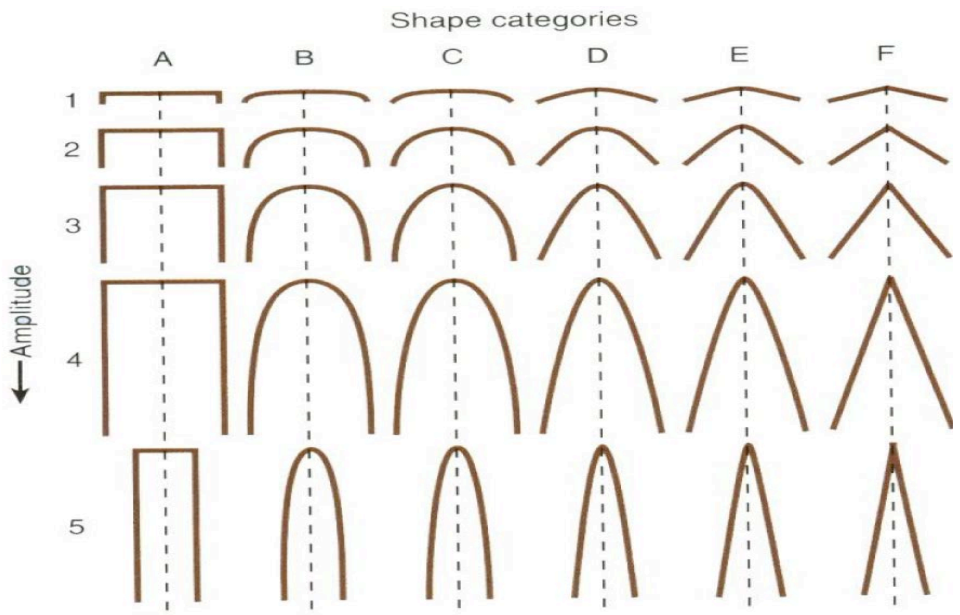

Figura 5. Clasificación de pliegues basada en su forma. La columna A se corresponde con pliegues tipo "caja", mientras que la columna F se corresponde con pliegues tipo "chevron". Tomado de Hudleston (1973).

1.7. Discusión y conclusiones generales

El análisis sobre la cinemática y dinámica de la sedimentación y erosión en el CPCM, en el occidente del GDM revela que la tasa de levantamiento tectónico del cinturón es de ~0.21 mm año^{-1}. Asumiendo que la denudación se encuentra en estado estacionario, se pueden distinguir sedimentos derivados localmente y sedimentos derivados de fuentes distales continentales. La tasa de sedimentación de ambas fuentes en esta porción del GDM, es de ~0.23 mm año^{-1}. La constante de difusividad de masa, un parámetro que controla la tasa de degradación del fondo marino es de ~0.42 m^2 año^{-1}, la cual es un valor característico de movimientos de masa rápidos y episódicos (Martin y Church, 1997; Yarbuh y Contreras, 2015).

Los resultados de este análisis muestran que los valores mencionados en el párrafo anterior no son constantes. Las estructuras cercanas a la plataforma continental del GDM están siendo levantadas mas rápidamente y están siendo degradadas con mayor intensidad, mientras que en las estructuras desarrolladas en las partes mas distales de la cuenca, la sedimentación sobrepasa el levantamiento tectónico. Los resultados muestran también que la deformación del CPCM comenzó de manera sincrónica

durante el Mioceno tardío, y que los sedimentos que se corresponden con los estratos de crecimiento están compuestos principalmente de sedimentos turbidíticos, sedimentos hemipelágicos, arenas y arcillas (Alzaga-Ruiz et al., 2009; Salomón-Mora et al., 2009; Yarbuh y Contreras, 2015).

A escala de cinturón, el CPCM exhibe dos longitudes de onda dominantes. Una de ellas es la longitud de onda de la Biot de ~ 9,4 kilometros (Biot, 1961) y otra es una longitud de onda secundaria de ~ 8.0 km. A escala de estructura individual, los coeficientes armónicos b_1 y b_3 controlan la forma de los pliegues (relaciones b_3/b_2). Además, se demuestra la importancia de la contribución del coeficiente armónico b_2 en el control de la geometría del pliegue. De este análisis se observan dos formas de pliegues: (1) las estructuras cercanas a la plataforma continental se corresponden con anticlinales cuspados-lobados (Ramsay, 1967), mientras que (2) las estructuras en el talud continental, cerca de la planicie abisal, se corresponden con anticlinales de onda sinusoidal. El principal mecanismo de amplificación de pliegues para el primer grupo de estructuras es por rotación de los flancos de los pliegues, lo que conlleva a las estructuras con crestas apretadas. Esto podría atribuirse a la contribución del coeficiente armónico b_2, cuya influencia crece con el aumento de la distorsión lineal. Por otro lado, la migración de la charnela podría ser el mecanismo de deformación dominante en la evolución del segundo grupo de anticlinales, donde los coeficientes armónicos b_2 y b_3 no contribuyen en la formación de los pliegues y la distorsión lineal es relativamente baja.

Por último, los resultados del análisis de Fourier revelan que la amplitud de los pliegues se incrementan a lo largo de la superficie axial siguiendo una relación lineal entre R_s y h. Del mismo modo, se puede observar que la amplitud aumenta linealmente con la distorsión. Ésta es una ley de crecimiento de pliegues que surge de la conservación de masa. Sin embargo, las longitudes de onda seleccionadas permanecen invariables con la profundidad.

Chapter 2

Introduction

2.1. Architecture of contractional deformation systems

Contractional deformation structures like fold-and-thrust belts form when rocks are shortened by tectonic or gravitational forces (Fossen, 2010). Structurally, these deformation systems involve two different styles: thin-skin and thick-skin deformation (Fig. 6). The thick-skinned deformation style refers to crustal shortening involving basement rocks and deep-seated faults. This occurs in orogens in which the crust has been shortened horizontally and thickened vertically (Shiner, 2004; Fossen, 2005). The thin-skinned deformation, on the other hand, is a style often observed at convergent tectonic boundaries, which occurs in shallow thrust faults without involvement of basement rocks (Davidson et al., 1997). The thin-skinned deformation style is typical of many fold-and-thrust belts developed in the foreland of a collisional zone, in the back-arc of a continental volcanic arc (Hatcher, 2007), and in deep-water passive continental margins (Morley, 2011). However, the distinctions between thin-and-thick-skinned styles are somewhat fuzzy (Nemcok, 2009).

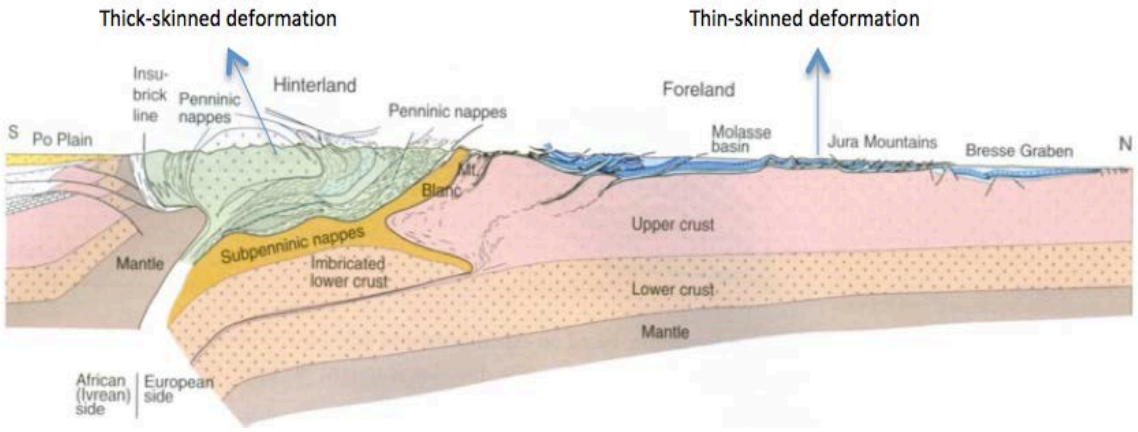

Figure 6. Cross-section through the Alps, Western Europe, showing the thin-skinned foreland deformation in the north (right), and the more pervasive and complicated deformation in the hinterland. Imbrication of the lower crust is indicated, based on seismic information. From Fossen (2010).

Deep-water fold and thrust belts are actually several different structural sub-styles considered together. There are at least three sub-styles in active and passive margins with very different driving mechanisms, structural and stratigraphic histories, hydrocarbon system characteristics, and therefore very different hydrocarbon potential. On active margins, subduction-driven accretionary prisms are created by shearing of sediments of the subducted plate (Kruger et al, 2009) Examples of active margin structures involved in thrust belts are seen in the Appalachians, Andes and Alps (Nemcok et al., 2009). On passive margins three types of gravity-driven extensional-compressional linked systems predominate. Among these systems we can further discriminate between salt-and-shale dominated systems. Gravitational collapse of shale-dominated sediment piles produces linked extension-compression "couples," with a deep-water fold and thrust belts at the distal margin (Rowan et al., 2004; Kruger et al, 2009). Massive salt gliding deep-water fold and thrust belts possess an added complexity in that they grade continuously updip into a salt-tectonic domain (Kruger et al, 2009). Examples of passive margin fold-and-thrust belts include the passive margin of the eastern Brazil, the passive margin of the western Africa, the Niger and Nile Delta, the Amazon Fan, and the passive margin of the Gulf of Mexico (Morley, 2011).

At finer scales, thrustbelts are made up of trends of folds and faulted blocks intimately related both in space and time. Fault-related folds are classified in three broad types of structures based on their geometry, kinematics, and sometimes-mechanical properties, namely (1) fault-propagation folds, (2) fault-bend folds, and (3) detachment folds (Fig. 7). These anticlines are economically important because they may store major hydrocarbon and mineral accumulations. Therefore, it is important to establish fold kinematics to test the position of source rocks, migration routes, and the formation of structural traps (Buchanan, 1996).

Progression of deformation in fault-related folds are thought to be the product of specific boundary conditions and rheological response of sedimentary rocks. However, little is known about how these folds lose amplitude with depth and how they evolve in time. As discussed previously, the development of fault-related folds depends in a complex way of different boundary and initial conditions present in foreland, back-arc and deep-water basins. For example, detachment folds are formed in stratified media with strong

rheological contrast among layers. In contrast, fault-bend folds and fault-propagation folds, require brittle rocks for them to evolve. Furthermore, fault-bend folds are formed by ramps connecting two mechanically weak layers of, say, shale.

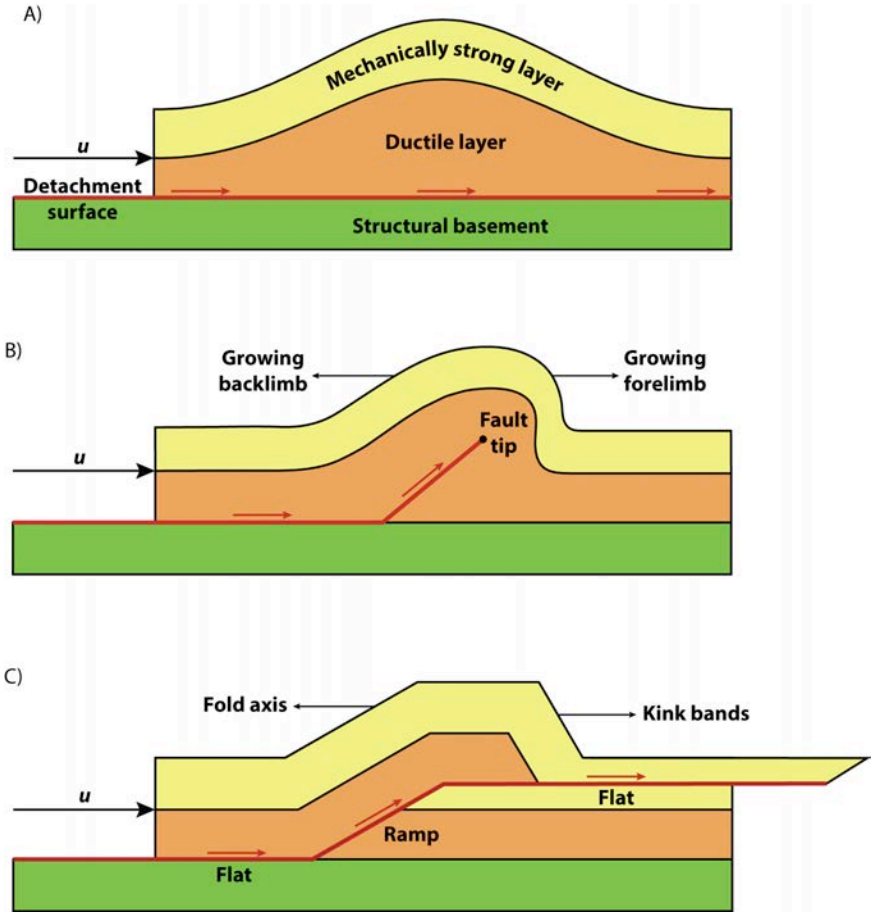

Figure 7. Scheme of the structural elements of fault-related folds. (A) Detachment folds; (B) fault-propagation folds, and (3) fault-bend folds. *u* is the linear shortening.

The term gravity tectonics is generally restricted to the downward sliding of large portions of rocks and sediments, notably of continental margin deposits resting on weak salt or overpressured shale (Fossen, 2010). For example, the Mexican Ridges foldbelt, a contractional deformation system located in the passive continental margin of the western Gulf of Mexico, offshore the Veracruz state, is associated with the deformation of Tertiary continental shelf and upper slope sediments by gravity sliding above a regional Oligocene shale detachment. Sediments are detached from underlying Mesozoic carbonates along 500 km of the Quetzalcoatl extensional system (Fig. 2). The resulting deformation is characterized by a series of fault-related folds, namely

detachment folds and fault-propagation folds, covering a large part of the deep-water continental slope (Salomón-Mora et al., 2009).

In this study we analyze a regional 2D seismic section of the Mexican Ridges foldbelt (MRFB), western Gulf of Mexico (GOM), and construct excess-area diagrams for each of the structures comprising the foldbelt to estimate the magnitude of shortening, the onset of folding, and the degradation of the folded seafloor (Chamberlin, 1910; Epard and Groshong, 1993; Groshong and Epard, 1994; Bulnes and Poblet, 1999 and references therein). From the chronostratigraphy reported in the literature (Salomón-Mora et al., 2009; Alzaga-Ruíz et al., 2009) we derive rates of tectonic and superficial mass transport and illustrate how they change across the MRFB. With this information we further analyze the interplay between deformation, erosion and sedimentation in this contractional deformation system.

Our work is motivated by the results obtained by González-Mieres and Suppe (2006) and Hubert-Ferrari et al. (2007). Based on the general principle of the conservation of mass and the excess-area method, we quantify fundamental deformation parameters, such as shortening and linear strain, for each of the thrust-related anticlines in the MRFB, which allows us to document with great accuracy spatial changes in deformation across this important contractional system.

The kinematic analysis presented here is the first study conducted at a foldbelt scale. The geometric analysis and the excess-area method allowed us to constrain how the flow rate per unit area of sedimentary particles exerts a primary control on the architecture of depositional environments and regulates the deposition of syntectonic successions in this type of structures (Tucker and Slingerland, 1996; Allen and Heller, 2012, and references therein). Then, we identify the lag time between the onset of uplift in the MRFB and the subsequent sedimentary response, which enabled us to establish with precision the beginning of deformation in this deep-water contractional system.

We finally validate our results with the THRUST software package (Contreras, 2002; Contreras, 2010). The structural evolution model of the deep-water MRFB presented here assumes that rocks behave as an incompressible deformable material and its kinematics is governed by the continuum mechanics of the conservation of mass.

Fold scaling laws are simple relations that show the behavior of different variables in a contractional system. Despite their simplicity, these relations capture many of the essential attributes of folding that at first glance may seem complex. Following the work by Biot (1961); Norris (1963); Harbaugh and Preston (1965); Whitten (1966); Chapple (1968); Stabler (1968); Hudleston (1973); Stowe (1988); Singh and Gairola (1992); Srivastava and Gairola (1997); Bastida et al. (1999) and Fossen (2010), we also derived fold scaling laws and document the process of wavelength selection during folding instability in the MRFB derived from Fourier analysis. The curve describing a folded surface can be expanded in a Fourier series, which is a mathematical procedure that breaks down a function into the frequencies that make it up, in which case we apply terms such as amplitude and wavelength. In this regard, the dominant wavelength (Biot, 1961) appears in the form of more or less regular sinusoidal waves. The latter is the wavelength of fastest rate of growth under the tectonic forces making up the MRFB. With the information available we were able to establish how anticlines acquire amplitude with depth and whether the growth of anticlines involves one or more dominant wavelengths.

The present thesis is divided in five chapters. The first chapter contains a brief synopsis written in Spanish; the present chapter 2 provides an introduction to the architecture of contractional deformation systems; chapter 3 discusses the kinematics and dynamics of sedimentation and erosion in the deep-water MRFB, western GOM basin; chapter 4 deals with fold scaling laws and the wavelength selection during folding instability derived from Fourier analysis; chapter 5 provides the general conclusions.

2.2. Objectives

2.2.1 General objectives

- Establish the kinematics and dynamics of sedimentation and erosion in the deep-water Mexican Ridges foldbelt, western Gulf of Mexico basin.

- Derive fold scaling laws and the wavelength selection during folding instability derived from Fourier analysis.

2.2.2. Specific objectives

- Quantify the excess-area occurring in the pregrowth and growth strata imaged in a high-resolution, two-dimensional (2D) seismic data of the MRFB.

- Constrain the temporal and spatial evolution of the entire MRFB.

- Derive the superficial mass transport rates at a foldbelt scale.

- Conduct a harmonic analysis to predict the shape of the folds and the kinematics of deformation of the MRFB.

- Derive mathematical functions describing the folding process in the MRFB.

- Document the process of wavelength selection during fold growth for the using the Fourier transform.

Chapter 3

The kinematics and dynamics of sedimentation and erosion in the deep-water Mexican Ridges foldbelt, western Gulf of Mexico basin.

3.1. Introduction

The passive margin of the western Gulf of Mexico (GOM) displays an extensive system of gravity-driven normal faults along its continental shelf, which merge at depth into a series of detachments along autochthonous Jurassic salt and overpressured Oligocene shale (Figs. 8 and 9; Rowan, 1997; Trudgill et al., 1999; Alzaga-Ruíz et al., 2009). The detachments transfer dip-slip motion from this extensional system into contraction motion parallel to the stratification. As a result, the Neogene siliciclastic sediments are decoupled from the underlying Paleogene successions and Mesozoic carbonates, and form a series of compressional deep-water foldbelts on the continental slope of the western GOM. A particular example of this broad contractional deformation system is the Mexican Ridges foldbelt (MRFB) offshore of the Veracruz state (Figs. 2, 8 and 9) in which the principal shortening occurs above a deep detachment zone located in Paleogene shale (Salomón-Mora et al., 2009; Alzaga-Ruíz et al., 2009).

In this study we analyze the kinematics and dynamics of sedimentation and erosion in the deep-water MRFB in the western GOM basin. We focus on examining the excess area of the pregrowth and growth strata imaged in a high-resolution, two-dimensional (2D) seismic data (Chamberlin, 1910; Epard and Groshong, 1993; Groshong and Epard, 1994; Bulnes and Poblet, 1999 and references therein).

Combining our results with chronostratigraphic information reported in the literature (*e.g.*, Salomón-Mora et al., 2009; Alzaga-Ruíz et al., 2009), we derive the average rate of change of shortening for each of the folds of the MRFB from the Late Miocene to the Present. With this information, we are able to constrain the temporal and spatial evolution of the entire fold train. Furthermore, we derive, perhaps for the first time in the literature, superficial mass transport rates at a fold-belt scale. The flow rate per unit area of sedimentary particles exerts a primary control on the architecture of depositional

environments and regulates the deposition of syntectonic successions. Despite its importance, little is known about how sediment flux varies in morphotectonic processes and at sedimentation time scales (Tucker and Slingerland, 1996; Allen and Heller, 2012, and references therein). In our analysis we also identify the lag time between the onset of uplift in the MRFB and the subsequent sedimentary response, which enables us to establish with precision the beginning of deformation in this deep-water contractional system. We demonstrate the observed lag is controlled by the supply of sediments into the basin, the tectonic uplift rate, and the rate at which the folded topography is degraded. We also validate our results using the THRUST software package (Contreras, 2002; Contreras, 2010).

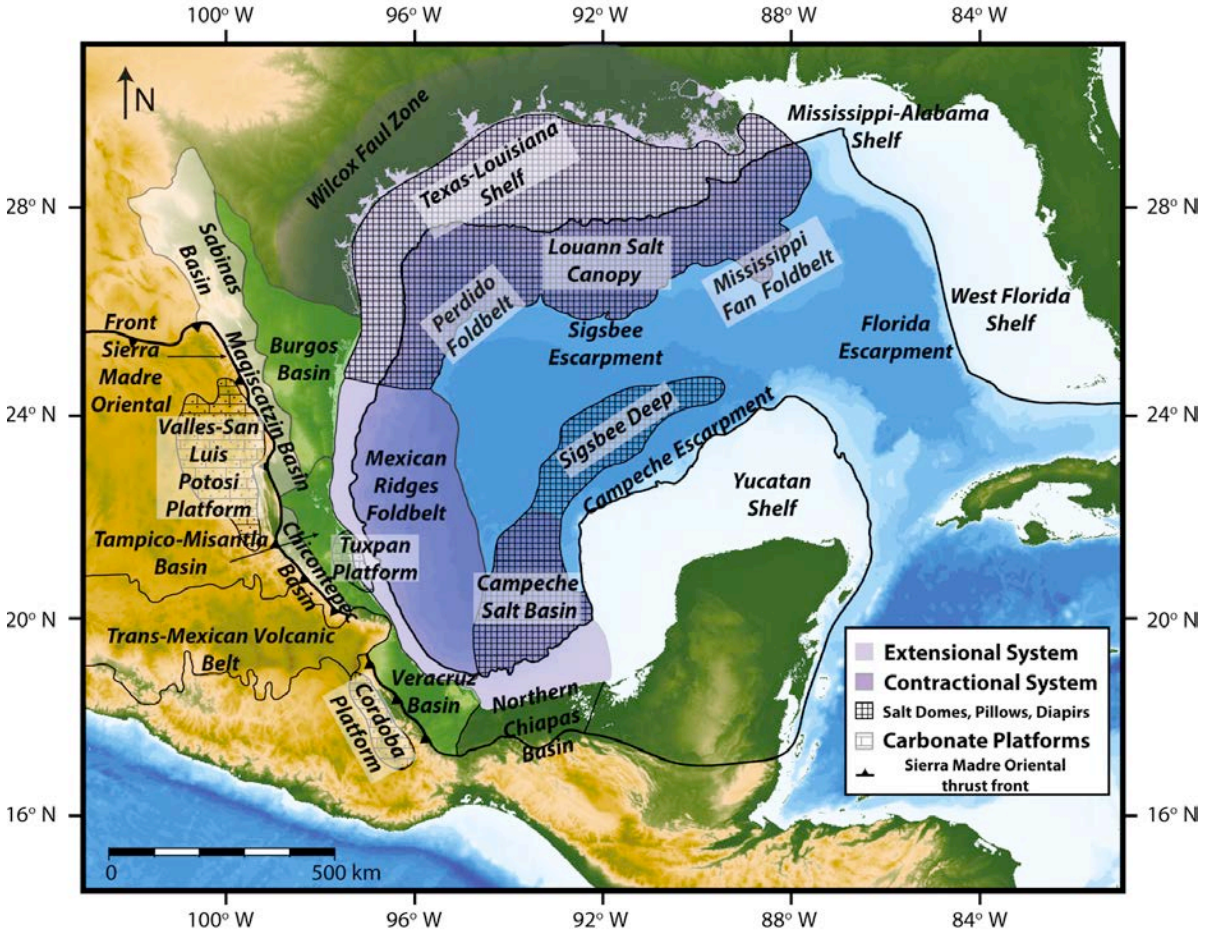

Figure 8. Map showing the main physiographic provinces and contractional systems of the GOM Basin. The Mexican Ridges foldbelt is located on the western continental slope of the basin. It is bordered by the continental shelf to the west, the abyssal plain to the east, the Perdido and Port Isabel foldbelts to the north, and the Campeche salt basin to the south. Check patterns correspond to the extent of the Jurassic salt; light purple colored area corresponds to the Neogene listric normal faults located along the continental shelf. Dark purple colored area corresponds to the deep water foldbelts (modified from Le Roy et al., 2008).

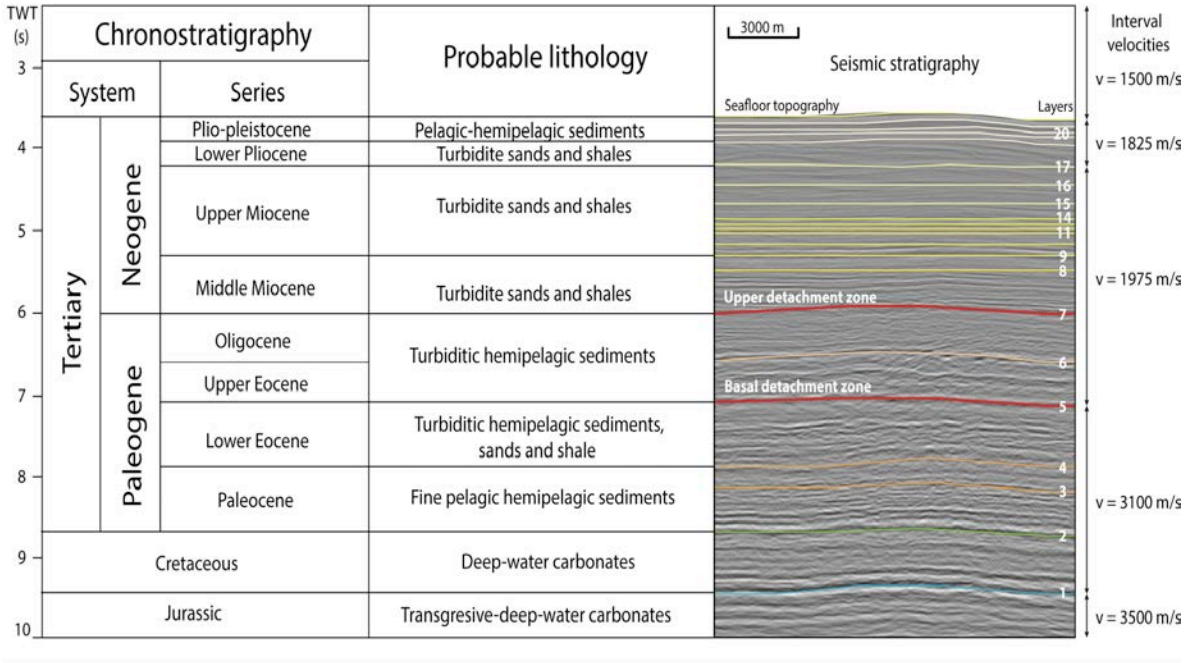

Figure 9. Stratigraphy of the Mexican Ridges foldbelt. The white numerals on the right side hand of the seismic image indicate the horizons interpreted in (A). Notice that horizon 5 marks the most basal detachment surface of the Mexican Ridges foldbelt (modified from Salomón-Mora et al., 2009 and Alzaga-Ruiz et al., 2009).

Our work is motivated by the results obtained by González-Mieres and Suppe (2006) and Hubert-Ferrari et al. (2007). Based on the general principle in continuum mechanics of the conservation of mass and the excess-area method, these authors quantified fundamental deformation parameters, such as shortening and linear strain, for a series of isolated detachment folds in several fold-and-thrust belts worldwide. Here, we carry out a similar analysis for each of the thrust-related anticlines in the MRFB, which allows us to document with great accuracy spatial changes in deformation across this important contractional system. Moreover, few studies have addressed the problem of syntectonic depositional time lags across basins. In the few case studies available, the lag times between the occurrence of a deformation event and a steady-state sedimentary response are in the order of 10^5-10^6 years (Allen and Heller, 2012). Since the duration of fold amplification and fold kinematics histories are often inferred from growth strata (Suppe et al., 1992; Holl and Anastasio, 1993; Poblet, 2012 and references therein), time lags associated with their deposition may distort the inferred chronology of events.

3.2. Geological background

The Gulf of Mexico has long tectonic and sedimentary history that spans from Mesozoic times to the present. The following is summary of what we presently know about this history and is based on the work by Roure et al. (2009). After Jurassic rifting and opening of the GOM, numerous carbonate platforms formed during the late Mesozoic episode of thermal subsidence along the western margin of the GOM that prograded toward intervening basinal domains (Figs. 2 and 8). During the Late Cretaceous-Paleocene, basin inversion by the growth of the Sierra Madre Oriental thrust belt resulted in tectonic uplift and unroofing of the allochtonous units. This event provided an important source of sediments that fed the adjacent foredeep, where coeval tectonic loading accounted for the flexure of the foreland lithosphere. From Oligocene onwards, erosional products of the Sierra Madre Oriental were transported to the GOM basin, where large volumes of siliciclastic successions were progressively deposited across the margin. This resulted in the development of a generalized gravitational collapse of both the western and northwestern margins of the GOM (Figs. 2 and 8). However, these two areas display contrasting structural styles, being mostly driven by the mobility of the Jurassic salt in Texas (Fiduk et al., 1999; Rowan et al., 1999a,b; Trudgill et al., 1999), whereas undercompacted and overpressured Eocene clays are assumed to control the localization of the deformation offshore Veracruz in south-eastern Mexico (Roure et al., 2009 and references therein). Nevertheless, other authors have proposed a deeper crustal control on the dynamics of gravitational collapse by the inversion of basement faults, or even by a deeper mantle convection at the rear of the Pacific subduction, inducing a post-Laramian regional tilt of the North American lithosphere (Leroy et al., 2008; Leroy and Rangin, 2008; Rangin et al., 2008; Roure et al., 2009).

Within this geologic context the MRFB formed in Tertiary continental slope successions of the western GOM, offshore of the Veracruz State (Fig. 2). It consists of approximately 12 fault-related folds detached along overpressured shale horizons (Figs. 2 and 9; Bryant et al., 1968; Garrison and Martin, 1973; Buffler et al., 1979; Alzaga-Ruíz et al., 2009; Salomón-Mora et al., 2009). To the west of the fold-thrust belt, in the continental platform-to-slope transition, these surfaces act simultaneously as a series of listric, gravity-driven normal faults that dissect the sediments of the Tuxpan continental shelf.

This gave rise in the Miocene to the Quetzalcoatl extensional system (QES) and a coeval foldbelt in the transition between the slope and the abyssal plain (Román-Ramos et al., 2001, 2004). Between the high-angle normal faults in the west, and the thrust anticlines in the east, a wide rollover structure ~15 km long has grown progressively, resulting in a major topographic break in the morphology of the slope profile (Fig. 2; Salomón-Mora et al., 2009).

Alzaga-Ruíz et al. (2009) and Salomón-Mora et al. (2009) used information from nine wells located on the Tuxpan continental shelf to establish the chronostratigraphy of the detached successions (Figure 9 synthetizes their results). Vazquez-Meneses (2005), on the other hand, made a detailed analysis of the seismic velocity structure of the MRFB showing the velocity structure is quite homogeneous. The siliciclastic sediments display interval velocities in the order of 2000 m/s, whereas the Mesozoic carbonates display interval velocities of 3100 m/s. However, some uncertainties remain regarding the ages of the seismic sequences in the eastern part of the MRFB because no drilling data link the seismics there with stratigraphy. Those authors also established the seismostratigraphy based on the seismic character, continuity, and internal geometry of successions deposited in the GOM's abyssal plain. As with the dating of the seismic sequences, the assignment of lithology for these sequences is sketchy (Salomón-Mora et al., 2009). The sequences are thought to consist of Neogene siliciclastic sediments, mostly turbiditic hemipelagic sediments, detached from the underlying Mesozoic carbonates along two stratigraphic levels: a basal Paleogene zone of overpressured argillaceous rocks and another one along the Miocene-Oligocene sequence boundary (Fig. 9; Alzaga-Ruíz et al., 2009).

Independent of these uncertainties, two stratigraphic successions can be identified in the folded sediments of the MRFB based on their deformation style and stacking patterns (Fig. 10): pregrowth strata, deposited prior to folding, and growth strata deposited synchronously with folding. The former set of layers can be recognized in the seismic-reflection profile as a series of reflectors that are deformed mostly by heterogeneous pure shear forming similar folds, whereas the latter strata display thinning sets and/or onlap surfaces towards fold crests (Figs. 2 and 10; Suppe et al., 1992; Hardy and Poblet, 1995; Poblet et al., 1997, 2004; Contreras, 2010). From those

stratigraphic relations, Salomón-Mora et al. (2009) concluded that the oldest structures are of Late Miocene age and developed in the western part of the MRFB near the QES (folds 1-6 in Figs. 2 and 9) followed by the rise of the structures of the eastern part of the fold train during the Early Pliocene (folds 7-12 in Figs. 2 and 9). Those authors also concluded that folding is still active, and the most recent folds are being formed in the central and eastern parts of the belt (see also Suter, 1991).

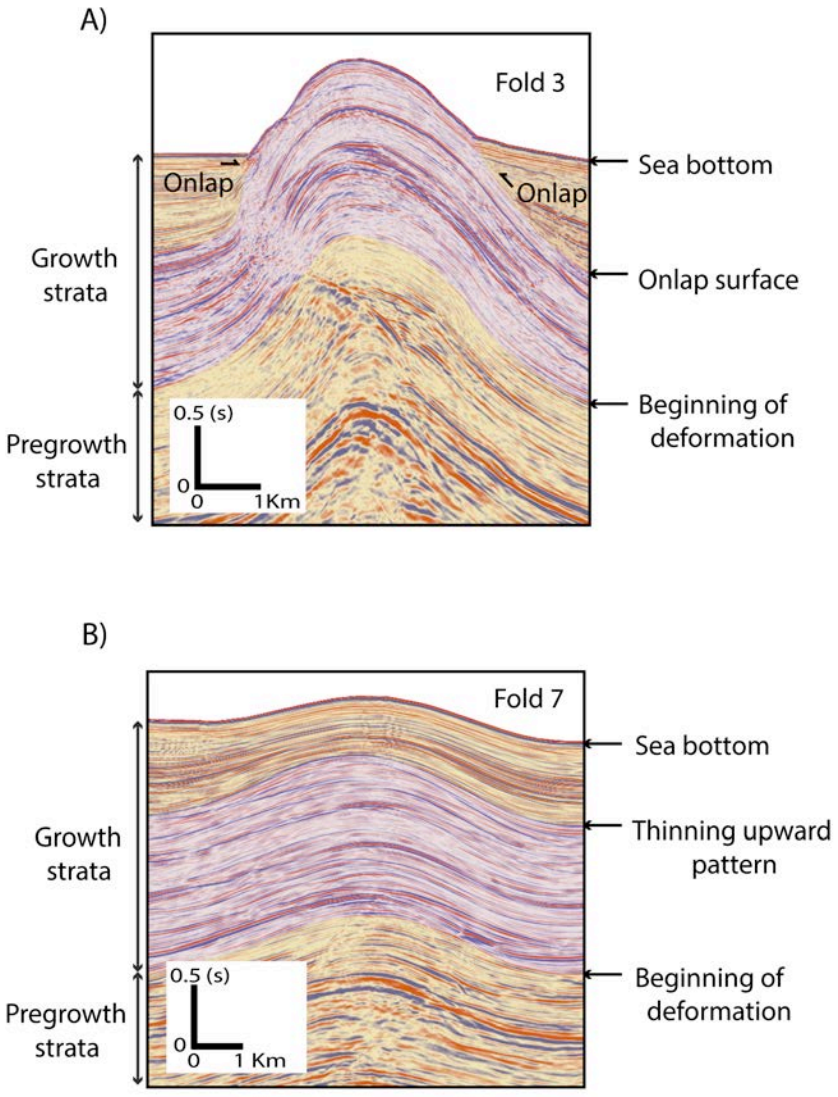

Figure 10. These figures illustrate the growth-strata geometries observed in the Mexican Ridges foldbelt. The stratigraphy consists of two successions: the pregrowth strata, deposited previous to folding, with a thickness of ~3.57 s of two-way travel time (partially shown in figures), and growth strata, deposited synchronously with folding, which appear as thinning sets or onlapping toward the fold crests, with a maximum thickness of ~0.85 s. In (A) we observe the development of onlap patterns toward the limbs of the structure. Thus, we can infer the sedimentation rate, *s*, is less than tectonic uplift rate, v_u. In (B), on the other hand, we observe development of thinning upward patterns covering the crest of the structure. By contrast, we infer that sedimentation rate, *s*, is greater than tectonic uplift rate, v_u.

3.3. Data and seismic interpretation

We analyzed a regional seismic-reflection profile of the MRFB in the western Gulf of Mexico basin (Fig. 2). The seismic data were collected and processed by Petróleos Mexicanos, Producción y Exploración (PEMEX-PEP). The seismic profile images both, the QES and the MRFB; it is ~180 km-long, has a penetration of ~10 s of two-way travel time (TWTT); and is oriented NE-SW, perpendicular to the regional strike. We carried out a depth conversion of the seismic line using interval velocities, which have been validated from previous studies and wells in the continental platform of the western GOM basin (Vazquez-Meneses, 2005 and references therein).

The interval velocities used in the depth conversion are shown in the seismostratigraphic column in Figure 9. The fold train in the seismic profile comprises twelve fault-related folds, numbered sequentially in Figs. 2. The seismics further resolved twenty-two high-amplitude reflectors with good lateral continuity. The horizons were numbered from base to top (Figs. 2 and 9), then, based on the chronostratigraphy proposed by Salomón-Mora et al. (2009) and Alzaga-Ruíz et al. (2009) we assigned ages to them. Moreover, following these authors, we assume the seismic horizons are sequence boundaries that can be considered stratigraphic time lines. Preliminary, reflectors 5-15 were assigned to the pregrowth section, whereas horizons 16-22 were assigned to the syntectonic successions (Fig. 9). The resulting structural model of the MRFB is shown in Figure 2.

The depth converted seismic horizons (Figs. 2 and 9) were exported from the seismic interpretation platform to a series of text files with information of relative geographic position and depth. The reflectors were then analyzed by a series of computer scripts with numerical integration and other least squares algorithms that allowed us to implement the excess-area method. Thus, our results are independent of any vertical exaggeration.

3.4. Style of folding

We now describe the overall geometry and style of these structures as well as the

geometry of syntectonic sediments (Figs. 2 and 7).

3.4.1. Detachment folds

Classical detachment folds are readily identified in the PEMEX-PEP seismic line of the MRFB (see folds 4, 6, 7, 9, 10, 11 and 12 in Figs. 2 and 7). These structures present simple geometries and are good examples of symmetric, low amplitude detachment anticlines (Jamison, 1987; Mitra, 2002; Contreras, 2010). The folds are detached in a shale horizon located at the base of the Upper Eocene (Figs. 2 and 9). Through direct measurements of the digitized seismic reflectors (horizons 1-22 in Figs. 2 and 9), we determined the wavelength of the structures varies from 7.2 to 9.1 km, the interlimb angle ranges between 3 and 25 degrees, and the structural relief varies from 254 to 1800 m. These values agree with those reported by Tharp and Scarbrough (1994), and Salomón-Mora et al. (2009). Strain in those structures is accommodated in a continuous and smooth fashion; none of the folds have sharp hinges or angular geometries. Folds 4, 6, 9 and 11, however, display disharmonic geometries in their cores.

The growth strata display a strong lateral symmetry indicating that the structures grew by acquiring amplitude as shortening was accommodated by folding. The synkinematic successions show thinning-upward patterns toward the crests of the folds, except for fold number four and eleven, which developed onlap patterns on both of its limbs. Mass wasting at the crest of these structures can be observed in the seismic profile (Fig. 2). This can be recognized as an abrupt change in slope at the limbs, where the crest losses continuity and become steeper.

3.4.2. Fault-propagation folds

Structures 1, 2, 3, 5, and 8 (see Figs. 2 and 7) present asymmetric geometries with sharp hinges; the forelimbs are much steeper and narrower than in the detachment folds described above. Asymmetry in those folds is due to thrust faults in the core of the folds. Faults propagate up section transferring slip into folding by means of trishear (Erslev, 1991; Hardy and Ford, 1997; Allmendinger, 1998). Notice that the propagating faults form both, backthrusts and forward thrust ramps. The wavelength of the structures

varies from 5.8 to 10.3 km, interlimb angles ranges between 12.8 to 27.5 degrees, and structural relief ranges from 1300 m up to 2650 m.

The geometry of synkinematic successions is also asymmetric, which indicates a tectonic control on sedimentation and accommodation space. In general, the stacking patterns of the syntectonic successions are characterized by the development of onlap surfaces on both limbs that change to a progressive unconformity toward the crest of the anticlines. Fold 8, however, is an exception, as it presents symmetric growth strata and thinning upward toward the crest of the fold, similar to the syntectonic sediments observed on the detachment folds. Fold 2 is also an exception as the crest of the structure is eroded.

3.5. Methods

The structural model discussed in the previous section is the base of our geometrical analysis; the excess-area method (Epard and Groshong, 1993; Groshong and Epard, 1994; Bulnes and Poblet, 1999 and references therein) was applied to each structure starting from deep-water carbonates identified by Salomón-Mora et al. (2009) located at horizon 1, to the sea-bottom topography located at horizon 22 (Figs. 2 and 9). The excess-area method can help verify whether a structural interpretation is balanced and provides independent information about the detachment depth, shortening and linear strain (Schlische et al., 2014). Previous workers have applied the method to fault-related folds (Epard and Groshong, 1993; Groshong and Epard, 1994; González-Mieres and Suppe, 2006, 2011; Groshong et al., 2012; Wiltschko and Groshong, 2012). As we will se below, the method also allows us to subdivide the stratigraphy into pregrowth strata and growth strata, marking the onset of deformation.

Before discussing further details of the excess-area method, we will define some simple geometrical concepts, which are illustrated in Figure 11. Fold wavelength, *L,* is the distance between two consecutive fold crests or synclines, whereas the shortening, *u*, is the amount of contraction of the fold (Fig. 11). These two quantities are related to one another in the following way:

$$u = L_0 - L, \qquad (1)$$

where L_0 is the initial wavelength of the fold, which is a function of the rheology of the stratigraphic successions and their thickness (Biot, 1961; Tharp and Scarbrough, 1994). The change in length or shape can be expressed in terms of linear strain, ε_x (in percent), which is the ratio of the total deformation to the initial dimensions of the fold

$$\varepsilon_x = \frac{u}{u+L} \times 100. \qquad (2)$$

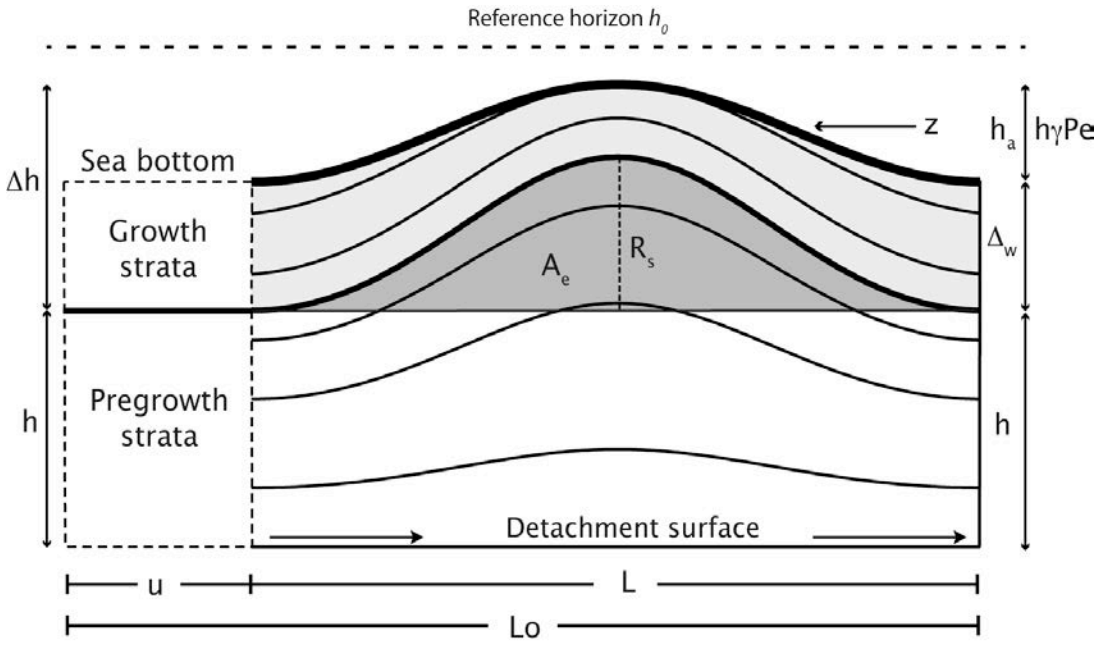

Figure 11. Sketch showing the structural parameters of detachment folds. *L*, is the wavelength of the fold; R_s, is the maximum structural relief or amplitude of the fold; A_e, is the area uplifted by folding; *h*, is the height above detachment surface; h_0, is a regional reference level; *u*, is the linear shortening; and *Lo*, is the initial wavelength. The sketch also shows the geometrical meaning of various dimensional and non-dimensional quantities that control the deposition of growth strata: Δh, is the change in topography due to folding, erosion, and sedimentation; Δw, is the thickness of syntectonic successions; h_a, is the amplitude of the folded topography; *z* is the elevation of the ocean floor; g, is the aspect ratio of the fold; *Pe*, is the Péclet number, the ratio between the mass flux due to tectonic uplift and the mass flux by erosion and sedimentation.

The structural relief, R_s, is the amplitude of the fold (Fig. 11), that is, the distance between the fold crest and the original stratigraphic position of the uplifted beds. Another parameter in Figure 11 is *h*, the depth of the detachment surface with respect to the original stratigraphic position as found in the synclines. Often this depth is referred with respect to an arbitrary datum (h_0 in Fig. 11). The excess area, A_e, is defined as the integral of the uplifted beds (Fig. 11). These parameters are related to each other by

means of the general principle in continuum mechanics of the conservation of mass

$$A_e = u \times h. \quad (3)$$

This means the area lost by shortening must be equal to the area uplifted by deformation (Chamberlin, 1910; Laubscher, 1971, 1977; Suter, 1981, Epard and Groshong, 1993). The excess-area method utilizes measurements of excess area, A_e, of a marker horizon versus the depth below the reference level, h_0, for multiple horizons. Pregrowth strata yield a straight line (green solid line in the plots of Fig. 12). We can estimate the shortening u in a A_e *vs.* h plot from the inverse slope of a best-fit linear equation $y = mx + b$ (Epard and Groshong, 1993; Groshong and Epard, 1994; González-Mieres and Suppe, 2006; Hubert-Ferrari et al., 2007), where m is the slope of the linear model and b (the y-intercept to the origin) is the is the depth of the basal detachment below the reference level h_0. In this way:

$$u = m = \Delta A_e / \Delta h. \quad (4)$$

Since u is being derived from a best-fit model, we report in our plots (Fig. 12) values of the coefficient of determination, R^2, a statistical parameter that indicates how well the models fit the data; thus, $R^2 = 1$ indicates that the linear model explains all variability in the data, whereas a value of zero indicates no relation exists between the response variable (A_e) and the regressor (h).

If syntectonic sedimentation is continuous during the fold amplification process, then growth strata provide a complete record of the structural development of fault-related folds and their degradation. Even though the deposition of growth strata is controlled by many factors including sedimentation and fold amplification rate, erosion, subsidence, and fold kinematics, among others (Hardy and Poblet, 1995), the syntectonic successions are characterized by two main features. Firstly, they thin above structural highs and thicken in depressed areas, and secondly they are generally less folded than the pregrowth beds. Those features make the limit between the pregrowth and growth strata straightforward to be recognized in A_e *vs.* h plots (Figs. 10 and 12). Given that synkinematic strata are less folded than the pre-kinematic sequences, the excess area

grows more slowly for the former beds (blue solid line in the plots of Fig. 12), which manifests itself as a change in slope in an otherwise linear relation between A_e and h (González-Mieres and Suppe, 2006; Hubert-Ferrari et al., 2007; Poblet et al., 2004; Fig. 12).

A)

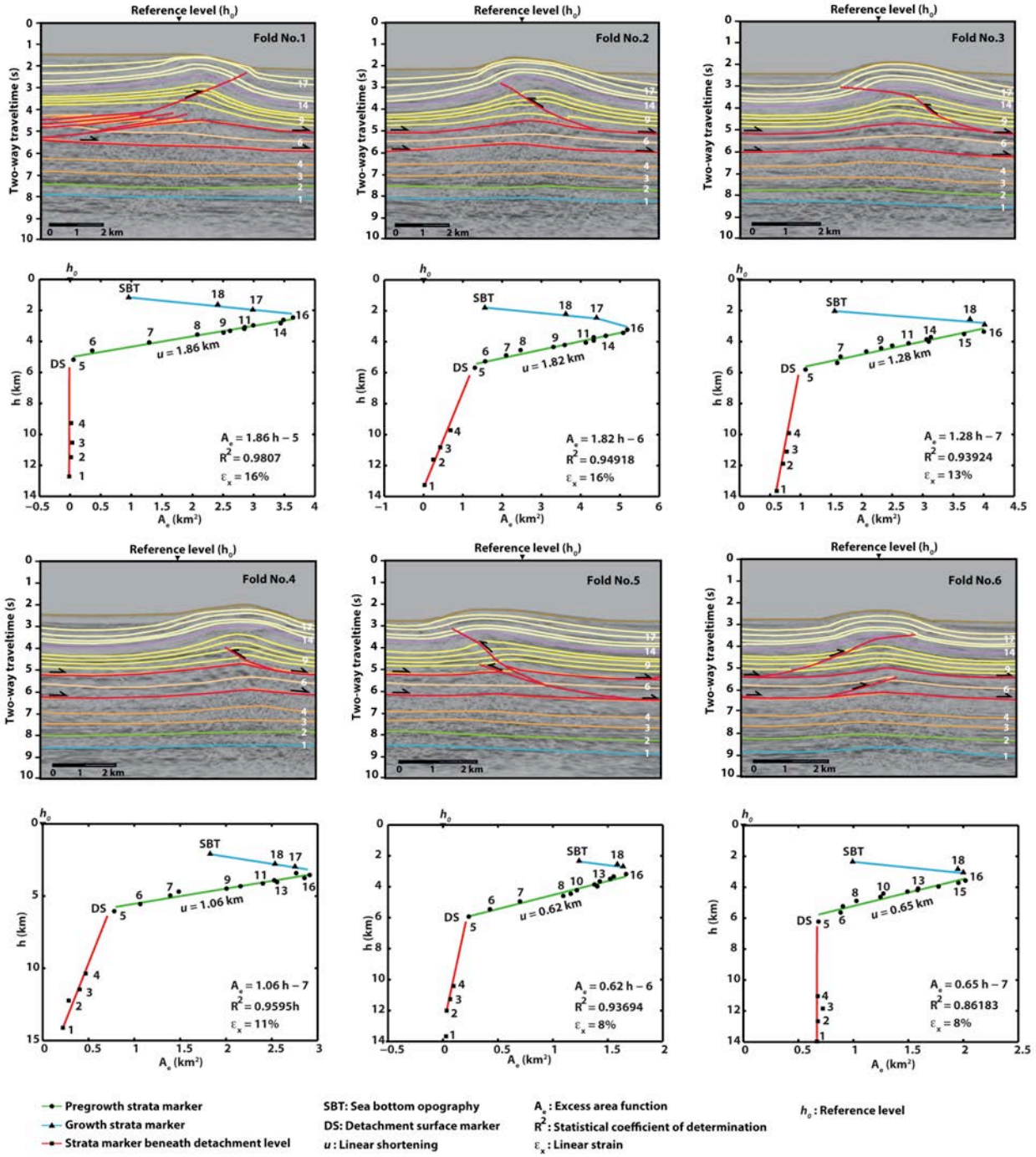

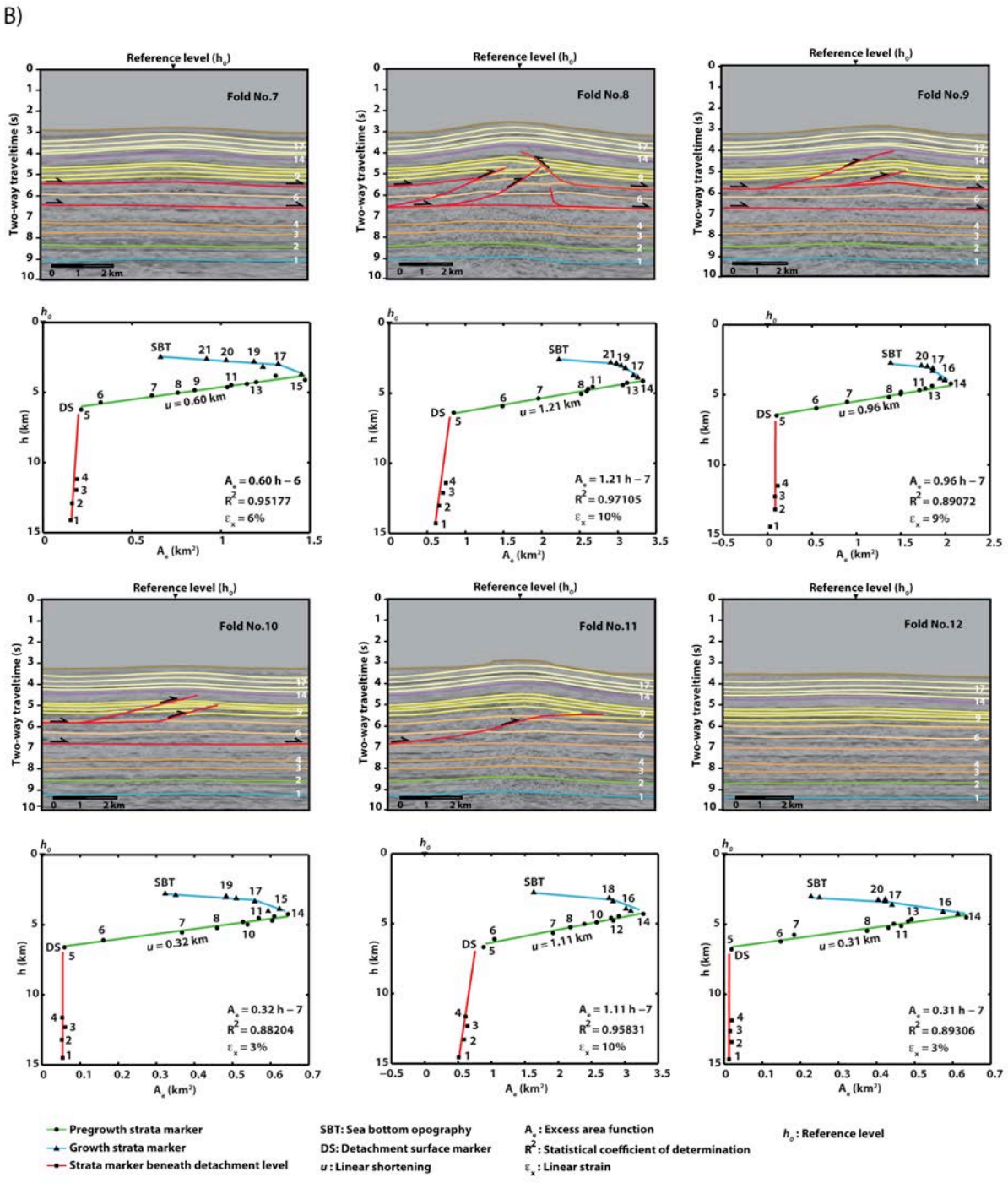

Figure 12. Plots of area of structural relief, A_e, as a function of h. The slope is obtained by a best-fit line model of the relation $A_e = u \times h$, and quantifies the magnitude of linear shortening, u. The break-down of the linear relation marks the onset of folding. For folds 1-6, the beginning of growth is observed around horizon 15 (Upper Miocene), whereas for folds 7-12 at horizon 14 (Upper Miocene). Further, notice the presence of a regional detachment surface located near horizon 5 (Lower Eocene-Upper-Eocene; see Fig. 9).

Once the boundary between pregrowth and growth strata has been identified in this manner, another important kinematic parameter, the onset of uplift (denoted here by t_u),

can be estimated from the chronostratigraphy of the growth strata (Fig. 10) and can be used to resolve the tectonic uplift rate, v_u, and the sedimentation rate, s, by means of the following expressions:

$$v_u = R_s / t_u , \quad (5)$$

$$s = \Delta w / t_u , \quad (6)$$

where Δw is the thickness of growth strata ponded in the synclines (Fig. 10).

Notice equation (6) contains the contributions from both far sediment sources and local sources from degradation of adjacent fold crests. To quantify this latter effect, we use a diffusion model of topography evolution in which the superficial mass transport, j_m (rate of sediment flow per unit area), is proportional to the gradient of the topography under transport-limited conditions (Culling, 1963; Carson and Kirkby, 1972)

$$j_m = \rho k \frac{\partial z}{\partial x} . \quad (7)$$

In expression (7), z is the elevation of the ocean floor (Fig. 11), ρ is the mass density of sediments, and k is the coefficient of superficial mass diffusivity. Here, we are principally concerned with estimating k, a critical parameter that describes the rate at which uplifted cross-sectional area is transported downslope by erosion and transport of sediments. Under steady-state conditions, k can be estimated by means of the relation

$$k = (l \times v_u) / Pe. \quad (8)$$

In equation (8) l is the characteristic wavelength of the fold, and Pe is the Péclet number, a non-dimensional quantity given by the ratio between the mass flux due to tectonic uplift and the diffusion of mass by erosion and sedimentation (Willett and Brandon, 2002). The characteristic wavelength is simply $l = L/2\pi$.

Now, from Figure 11 it can be appreciated that the amplitude of the folded topography, h_a, has a direct geometrical interpretation in terms of Pe (Contreras, 2010). Using this

interpretation we can solve for this later parameter

$$Pe = h_a / \gamma h, \quad (9)$$

where h, once again, is the thickness of pregrowth strata. $\gamma = l/h$ is the aspect ratio of the region. Substituting this relation in (9) simplifies Pe to $Pe = h_a / l$. Therefore, in the context of contractional deformation, Pe is simply the ratio between the amplitude of the folded topography and the characteristic wavelength of the fold. Once again, expression (9) is valid only if the topography is in steady state, *i.e.*, uplift and erosion are in equilibrium. Consequently, in our computations of k it is implicit that mass fluxes in the MRFB are in a state of balance. In the discussion section, we will address whether the seafloor morphology is in steady state.

3.6. Results

Figures 13-19 summarize our results; they indicate that in general deformation decreases with distance from the continental slope to the distal part of the foldbelt (Fig. 13). Since uplift occurred simultaneously (Fig. 14), the rate of deformation closely mirrors strain (Fig. 15). The spatial variations in superficial mass transport (Figs. 16 and 18) follow a similar spatial pattern. The sediment flux declines with distance from the continental slope to the abyssal plain (see figures bellow in section 3.6.2).

3.6.1. Structural analysis of pregrowth strata

In general, the linear fittings of the excess-area exhibit little dispersion and overall high values for R^2, from 0.86 to 0.98 (Fig. 13). The slope of those plots indicates the linear shortening, u, range from 300 to 1900 m, giving a total tectonic transport of 11.8 km (Fig. 13). This value also corresponds with the amount of down-slope translation observed in the QES (see discussion below). The fold wavelengths vary from 5800 to 10300 m, and have a combined length of 99 km. Moreover, Figure 13b shows that for folds 1-4 near the QES, linear strain is ~15% whereas for folds 5-12, on the continental slope of the GOM, strain drops to a value of ~10%.

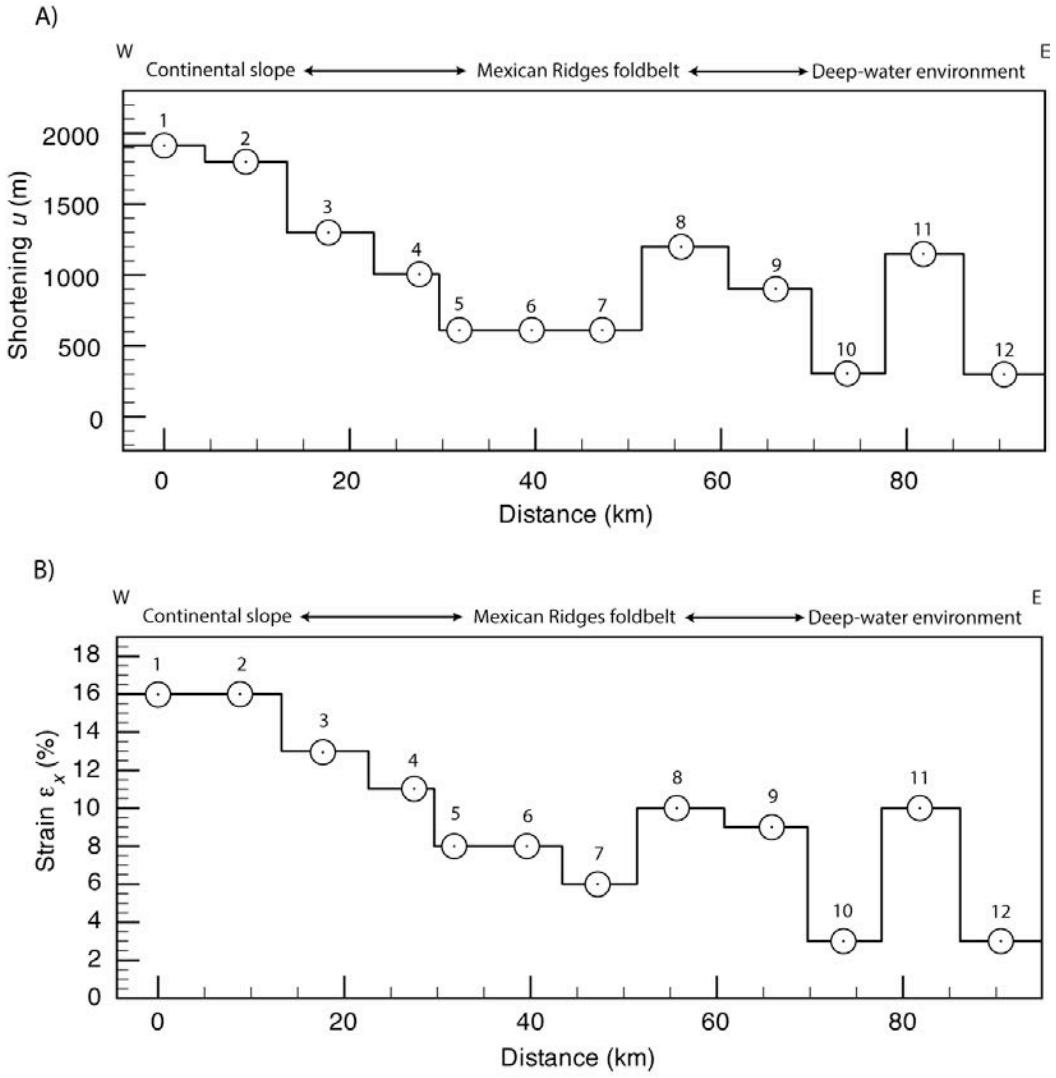

Figure 13. Plots of (A) linear shortening, *u*, and (B) linear strain, ε_x, across the Mexican Ridges foldbelt. Notice that the magnitude of *u* decreases with distance across the foldbelt. The behavior of linear strain, ε_x, closely follows that of *u*. This is, ε_x, is high for folds near the Quetzalcoatl Extensional System, and low in the distal part of the belt.

The initial wavelength, L_o of folds (Eqn. 1), on the other hand, varies from 6300 to 11700 m, and its sum gives an undeformed length of ~111 km for the compressional system. By taking into account that the extensional domain is 30 km (including the rollover developed in the hanging-wall block), we constrain the initial length of the entire paired extensional-compressional system to ~140 km (Figs. 2). In a subsequent section we use these values to construct a balanced cross-section of this gravity-driven deformation system.

To assess whether the structures of the MRFB satisfy conservation of area and how shortening is accommodated with depth, we now analyze the intercepts of both the *x*

and *y* axes of the A_e *vs. h* plots. As stated before, the *y*-intercept is the depth of the basal detachment below the reference level h_0 (Fig. 11), whereas the A_e-intercept indicates whether structures are closed systems. Our analysis suggests that only one regional detachment surface exists, and is found in the vicinity of reflector 5 (~6 km depth; Lower Eocene-Upper-Eocene boundary; Figs. 2, 9 and and 12). The majority of evidence does not support the existence of the inferred upper detachment shown in Figures 2 and 9. For folds 1, 2, 5, 9, 10 and 12, their A_e-intercepts cross the excess area at near zero values (Fig. 12), suggesting these structures are area balanced. On the other hand, the remaining folds (3, 4, 6, 7, 8 and 11) are thrust anticlines whose A_e-intercepts cross the excess area axis at nonzero values. This effect can be interpreted in four different ways: (1) diapiric shale flow into the core of the folds (Hubert-Ferrari et al., 2007); (2) a deeper detachment surface (Bulnes and Poblet, 1999); (3) a velocity pull-up effect in the seismic data (Yilmaz, 2001); and (4) the basal decollemet is not planar but just could be refolded (Fig. 2; Roure, et al., 2009). We can rule out flow from beneath synclines into the anticlines because this effect occurs erratically throughout the foldbelt. The same argument can be used to rule out the deeper detachment. This leaves a velocity pull up, which we think is the most likely explanation, and the possibility of detached sedimentary cover above inverted underlying features. Our results, however, do not offer support for the latter interpretation because extension is balanced against contraction (see kinematic model section below). Thus, there is no evidence of any additional regional compression competing with the gravitational collapse of the margin.

The positive linear relation between A_e and *h* breaks down systematically around deposition of horizon 15 (~ 3-4 km-depth), marking the onset of folding, t_u, and the pregrowth/growth strata limit (Figs. 12 and 14). This horizon falls between the base of the Upper Miocene and the Mio-Pliocene limit (see Fig. 14). To constrain further the age of deformation, we interpolated the age of horizon 15 with respect to the age of those limits (5.3 and 11.2 Ma) assuming a constant sedimentation rate. Based on this, we were able to determine the onset of folding t_u at ~8.0 Myr, which is approximately 1.5-3 Myr earlier than in previous estimates (Salomón-Mora et al., 2009).

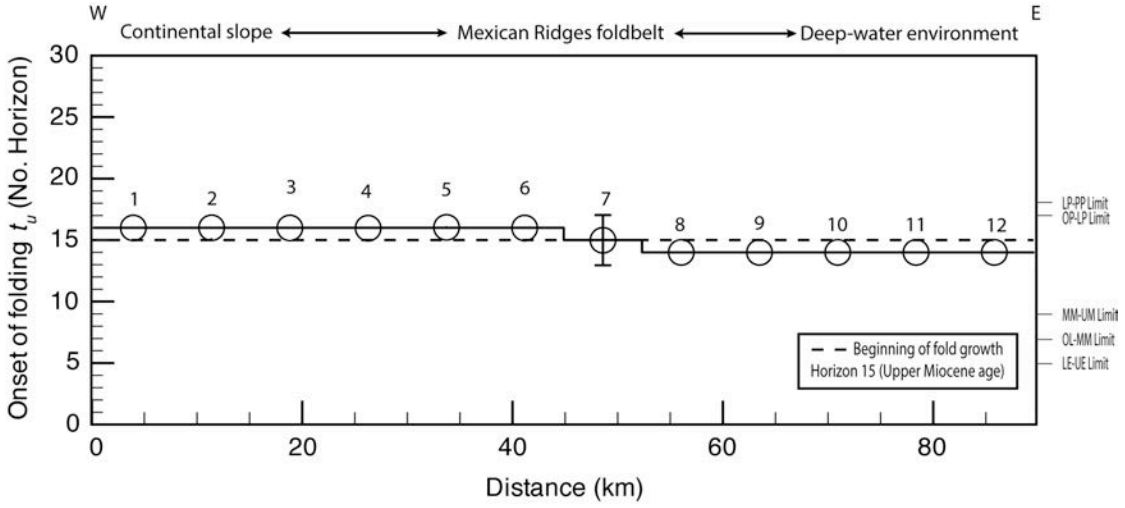

Figure 14. Here, we plot the beginning of growth of each of the fold-related folds of the Mexican Ridges foldbelt (obtained from Fig. 12) as a function of distance across the foldbelt. Folding started simultaneously approximately during the deposition of horizon 15 (Upper Miocene; see Fig. 9). Abbreviations are as follows: PA: Paleocene, LE: Lower Eocene, UE: Upper Eocene, OL: Oligocene, MM: Middle Miocene, UM: Upper Miocene, LP: Lower Pliocene, PP: Plio-Pleistocene.

Finally, the maximum structural relief of the MRFB structures, R_s, ranges from 250 to 2650 m, with a mean value of ~1400 m. By substituting our estimations of t_u and R_s in equation (5) we were able to constrain the uplift rate of the each of the folds making up the MRFB, which is shown in Figure 15. The rate of uplift decreases across the MRFB in the eastward direction ~30% and has a mean value of ~0.21 mm/yr.

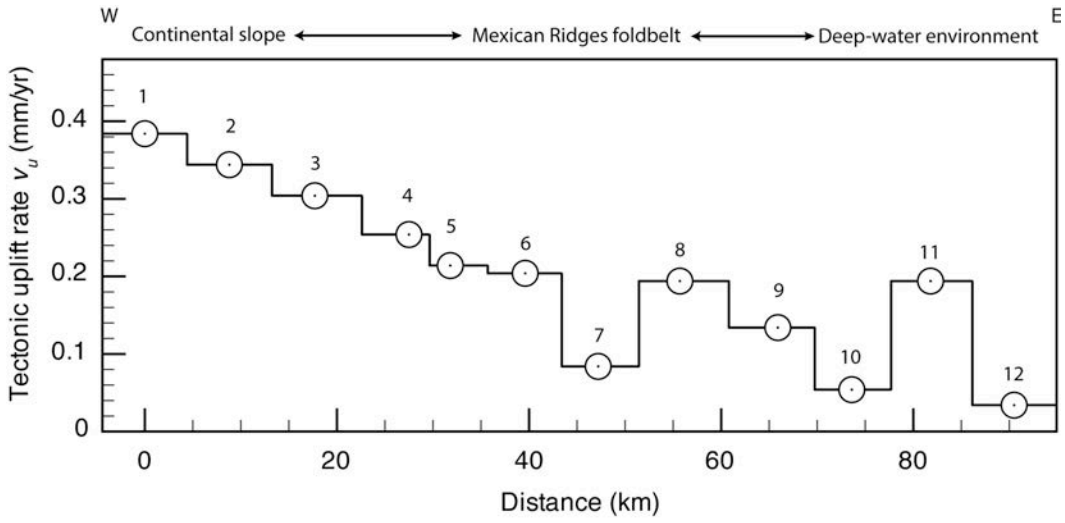

Figure 15. Plot of the tectonic uplift rate, v_u, as a function of distance across the foldbelt. v_u was calculated from the ratio between the maximum structural relief, R_s and the onset of folding (~ 8.0 Myr, see details in main text). v_u decreases from 0.39 mm/yr in the western part of the belt, on the continental slope, to 0.04 mm/yr in the east near the abyssal plain.

3.6.2. Structural analysis of growth strata

Two types of sediments were considered in our analysis of growth strata: sediments derived from distant sources (deposited horizontally), and sediments derived locally by diffusion of topography (deposited laterally from the crests of anticlines to adjacent synclines). The sedimentation rate in our analysis includes sediments from both sources; this parameter is derived from the thickness of syntectonic sediments deposited in the synclines, and the time elapsed since the onset of deformation. The thickness of growth strata varies from 0.7 to 1.3 s of TWTT (Figs. 2, 9, 10). Our depth conversion (Fig. 9) shows the thickness of growth strata, Δw, of these highly porous, water saturated sediments ranges from 1300 to 2400 m. In this way, the sedimentation rate in the synclines, *s*, varies from 0.18 up to 0.32 mm/yr, and has a mean value of 0.23 mm/yr. A plot of changes in sedimentation rate across the MRFB is shown in Figure 16; sedimentation is the highest close the Tuxpan continental shelf, where discharge is large, and decreases with distance, reaching minimum values in the deep-water section of the foldbelt.

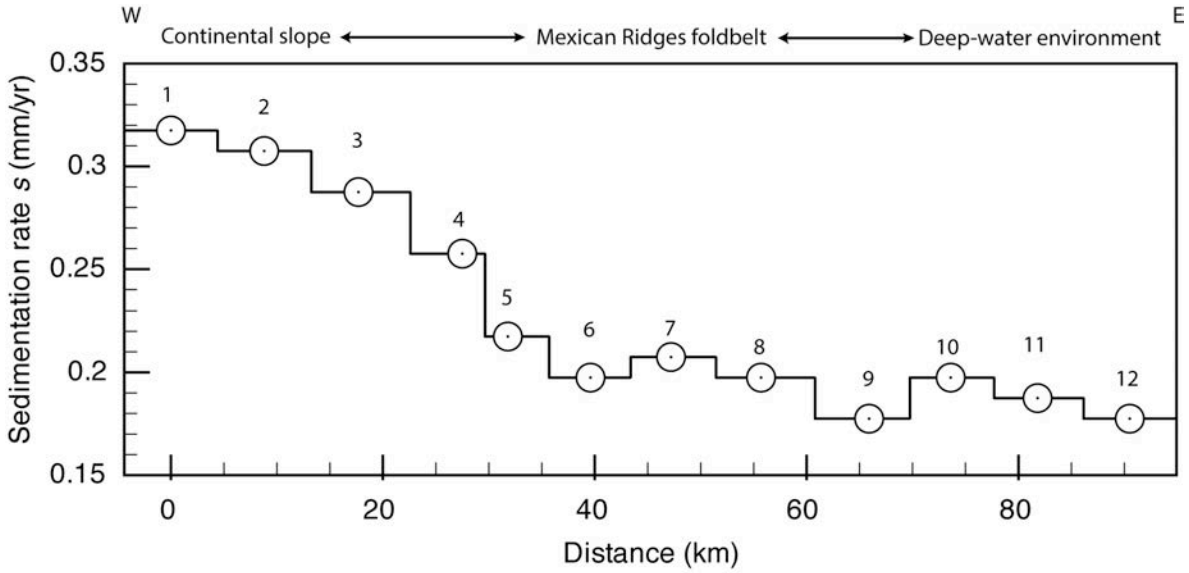

Figure 16. Plots of the far-source sedimentation rate, *s*, with distance across the foldbelt. *s*, was estimated based on equation (10). For folds 1-5, the far-source sediments decrease with distance, while from structure 6 onward, sedimentation rate remains nearly constant.

The above results suggest that changes in growth stratal geometries are expected across the basin as the rate of sedimentation is an important parameter that controls the development of stratal patterns (*e.g.*, Hardy and Poblet, 1995; Poblet, 2012). For folds

1-6, in the western section of the MRFB, the stacking patterns of syntectonic successions are characterized by onlaping on both limbs (Fig. 10a), whereas for folds 7-12, in the eastern section, development of thinning-upward patterns is observed (Fig. 10b). The onlapping relation indicates that the tectonic uplift rate, v_u, is greater than the sedimentation rate, s, which is corroborated by the plots of the ratio between s and v_u shown in Figure 17 (see also Fig. 10a). By contrast, the thinning-upward pattern indicates that the syntectonic sedimentation rate, s, is greater than the fold uplift rate, v_u, which again is confirmed by the ratio between these two parameters (Figs. 10b and 17).

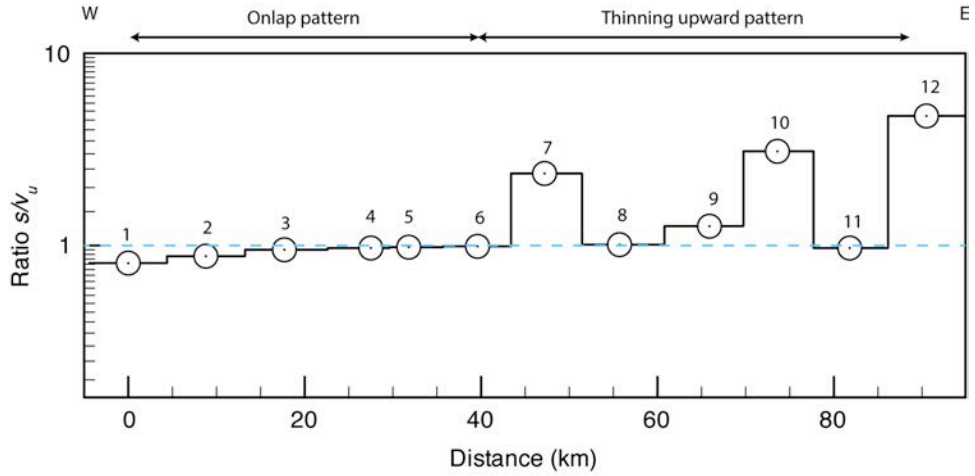

Figure 17. This figure illustrates changes in the ratio s/v_u across the Mexican Ridges foldbelt. Where the sedimentation rate is greater than tectonic uplift ($s/v_u > 1$), thinning upward patterns develop covering the crest of the folds (folds 7-12), whereas $s/v_u < 1$, results in the development of onlap geometries toward the crest of the folds (Folds 1-6).

On the other hand, our estimates for the mass diffusion coefficient, k, in the MRFB vary from 0.19 to 0.87 m^2/yr and have a mean value of 0.42 m^2/yr (Fig. 18a). Figure 18b illustrates the normalized sediment flux J_m/ρ across the MRFB as predicted by equation (7). To calculate the gradient $\partial z/\partial x$ we used the sea bottom reflection, which we converted to depth z using a seismic velocity of 1500 m/s; J_m/ρ was filtered with a three-point running average to smooth results. It can be appreciated that maxima in superficial mass transport are observed at the eastern limbs (leading edge of anticlines), which means that transport is dominantly eastward. The eastern limbs are being degraded faster than the western ones, which result in an asymmetric seafloor topography with steeper slopes on the west side of the anticlines. Also notice that the sediment flow decreases eastward, possibly due to a drop in energy in the sedimentary environment,

effect embodied in *k* (Fig. 18a), and by the slower rates of uplift in the eastern section (Fig. 15).

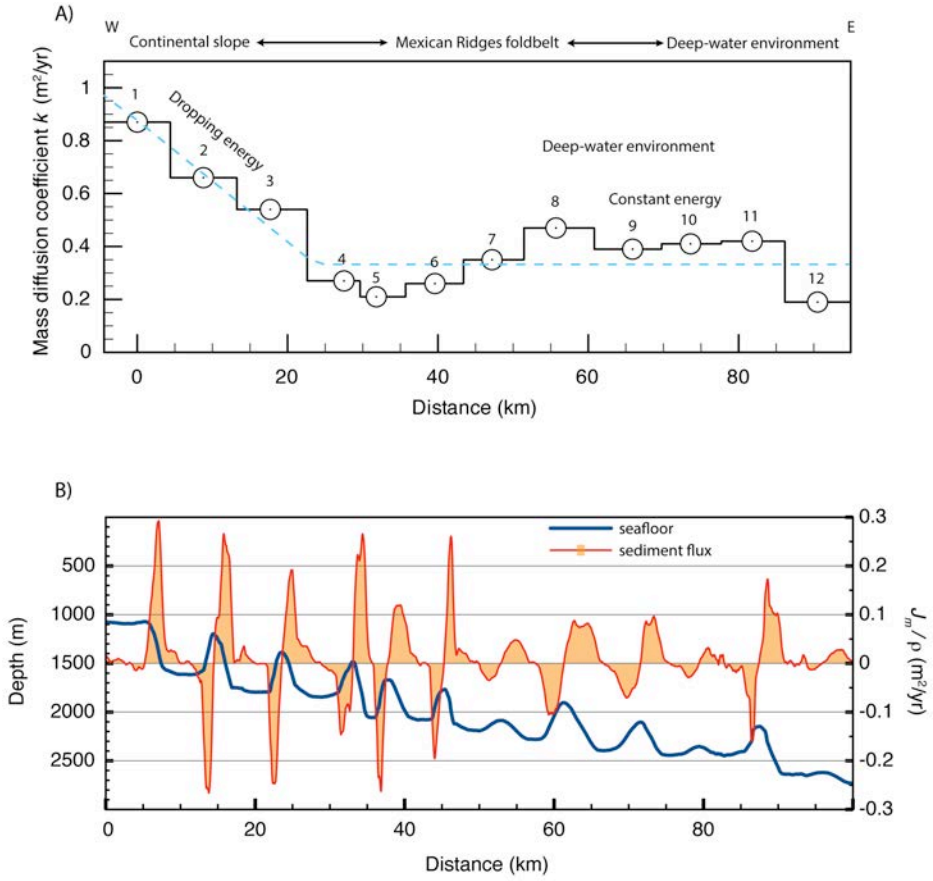

Figure 18. (A) Changes in the mass diffusion coefficient, *k*, across the Mexican Ridges foldbelt. The coefficient varies from 0.87 m^2/yr near the Quetzalcoatl Extensional System, to 0.19 to m^2/yr near the abyssal plain. Notice that for folds 1-4, *k* drops continuously to a value of ~0.3 m^2/yr, but then remains broadly constant toward deep-water environments. The drop in *k* likely reflects changes in energy in the sedimentary environment. (B) Changes in normalized sediment flux across the Mexican Ridges foldbelt. Blue line indicates bathymetry. Positive values indicate flux to the east, negative values flux to the west. See text for details.

3.7. Discussion

3.7.1 Kinematic model

To validate our results, we performed a cross-sectional kinematic simulation to match the structures observed in the QES and the MRFB (Fig. 19a). The simulation was performed using the THRUST software package (Contreras and Sutter, 1990; Contreras, 1991, 2002, 2010); the equations upon which the software is based, consider rocks as

an incompressible deformable material, and its kinematics satisfies the continuity equation. Therefore, area is conserved, and balanced cross-sections are obtained with the program. The model also considers the following boundary conditions: (i) the vertical flux across the core of the fold is described by a cosine function, (ii) the horizontal flux due to transport along a basal detachment remains constant with depth, and (iii) the depth of the detachment remains fixed. Since the software carries out a forward simulation based on initial conditions (Contreras, 2002), we can also obtain the geometry of the reference state (palinspastic cross-section; Fig. 19b). The program can also model the accumulation of growth strata and the degradation of the topography created by folding. These processes are approximated by means of the transport-diffusion equation. The specific values used for each fold are shown in Figure 19. The modeled region is 140 km long, and the simulation starts after the deposition of horizon 15 (Late Miocene; Figs. 2 and 9). The left system boundary is placed in the footwall of the QES, whereas the right boundary is located in the foreland of the MRFB, which is essentially stationary.

Our simulation fits both, the observed structural style as well as the overall geometry of the growth strata. We can appreciate in Figure 19a that the structural model obtained with the THRUST package is in good agreement with the section shown in Figure 19a. Our modeling results lend support to both our structural model and the parameters that control superficial mass transport estimated here. Perhaps more importantly, our cross-sectional balancing and restoration exercise demonstrate that the total shortening accommodated in the MRFB equals the total extension in the QES (Fig. 19b). Previous studies have addressed the mismatch between extension and contractional slip on paired, gravity-driven deformation systems (Bulnes and Poblet, 1999; González-Mieres and Suppe, 2006; Butler and Paton, 2010 and references therein). Observations made by these authors show a significant amount of additional strain (up to 25%) is required for cumulative shortening in the contractional domain to balance the net down-slip motion higher on the continental shelf (*e.g.* Butler and Paton, 2010). The additional shortening, not seen in the excess-area measurements, can be explained most plausibly as horizontal tectonic compaction, volume loss, and other penetrative deformation mechanisms (González-Mieres and Suppe, 2006; Butler and Paton, 2010). The discrepancy in area-balance can also be a product of the failure of the

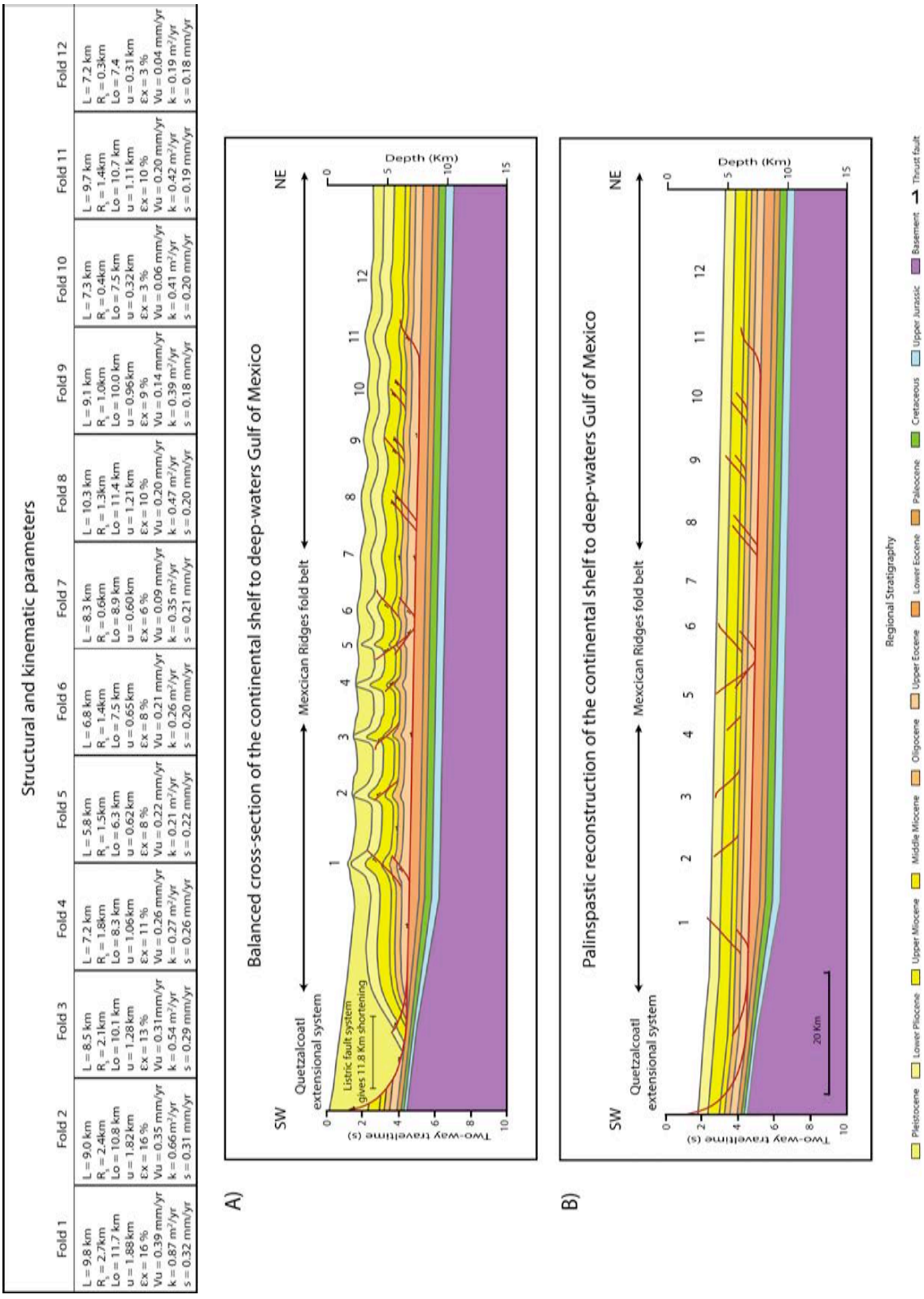

Figure 19. Balanced cross-section and palinspastic reconstruction of the MRFB based on the parameter values obtained from the structural analysis (upper table). The simulation was carried out using the THRUST kinematic forward modeling program (Contreras and Sutter, 1990; Contreras, 1991; Contreras, 2002; Contreras, 2010; see text for details).

detachment-depth prediction (Bulnes and Poblet, 1999). Those phenomena, however, are missing or appear to be negligible in the MRFB since we can recognize all the deformation. This might be attributed to the low-strain observed in the MRFB.

Other studies have evidenced a Neogene deep-rooted deformation zone below the main basal detachment surface in the area (horizon 5; Figs. 2 and 9). They suggest that a deep-seated reverse fault zone can be interpreted and is result of a Neogene transpressive dextral motion that could have triggered gravity sliding along the Mexican Gulf margin (Le Roy et al, 2008). This event has been recognized in the basement of the Veracruz and Campeche basins, as well as along the eastern margin of the GOM (Fig. 2). Moreover, an analysis of the seismic activity in the GOM suggests that an event recorded on May 2007 in the western margin of the Gulf of Mexico, off Tuxpan, with a magnitude Mw = 5.5, is product of a dextral transpressional stress state (Franco et al., 2013). Although it is thought that a part of the up-slope gravity-driven extension and coeval compression are the result of true compression (Roure et al. 2009), we have evidenced that such component likely is a small fraction of the total shortening accommodated in the MRFB since both the QES and MRFB are area-balanced.

3.7.2. Dynamics of the deposition of growth strata and the delay of the sedimentary response to folding

We now discuss how changes in superficial mass transport control the deposition of growth strata across the MRFB. Previously, we noted changes in uplift rate and mass flux throughout the continental slope resulted in growth strata of contrasting stacking geometries. On one hand, rapid uplift rates and low superficial mass transport-to-uplift rates gave rise to uncovered anticlines alongside onlap patterns on both limbs (folds 1-6; Figs. 10a, 17 and 20b). On the other hand, slow uplift rates and fast superficial mass transport-to-uplift rates resulted in covered anticlines with thinning upward patterns toward their crests (folds 7-12; Figs. 10b, 17 and 20a). Salomón-Mora et al. (2009) and Alzaga-Ruíz et al. (2009) used these stratigraphic relations to establish the boundary between pre-tectonic and syntectonic successions (details of the method can be found in Poblet, 2012 and references therein) and concluded that fold amplification in the MRFB occurred in two stages. According to these authors, deformation in the western

part of the foldbelt started in the Upper Miocene, whereas in the eastern part deformation initiated in the Lower Pliocene. However, as can be appreciated in Figure 14, fold development started synchronously across the foldbelt around the time horizon 15 was deposited (Late Miocene; Fig. 9).

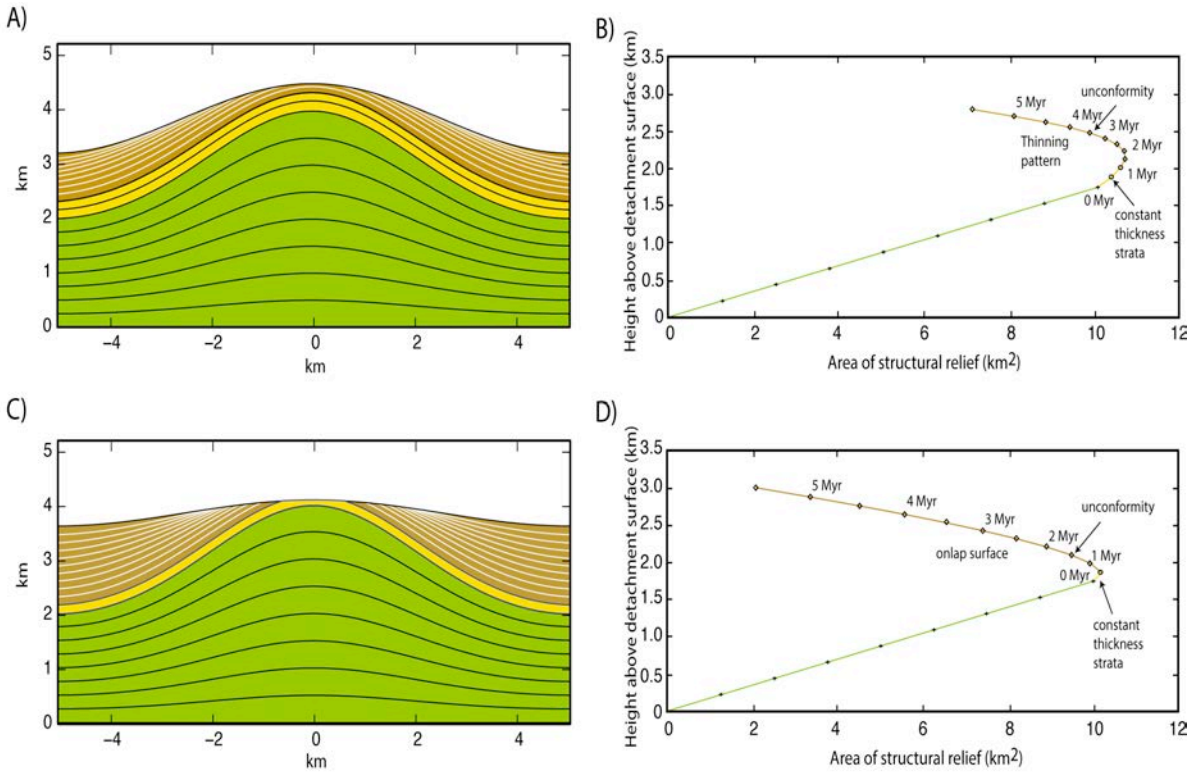

Figure 20. (A and C) Numerical simulations of the syntectonic stratigraphy of growing detachment folds. (B and D) The area of structural relief, A_e, is plotted versus the height above the detachment surface, h, of the pregrowth strata (green successions) and growth strata (yellow and tan successions) shown in (A) and (C). Model parameters for (A) are mass diffusivity, k, 2 m^2/yr; tectonic uplift rate, v_u, 0.25 mm/yr; and sedimentation rate, s, 0.3 mm/yr. Similarly, parameters for (C) are mass diffusivity, k, 10 m^2/yr; tectonic uplift rate, v_u, 0.25 mm/yr; and sedimentation rate, s, 0.21 mm/yr. Observe that in model (B), the sedimentation rate, s, is greater that the tectonic uplift rate, whereas in model (D), the response of sedimentation is low with respect to v_u. The layer boundaries between the growth strata represent time lines every 0.5 Myr. In both plots, 0 Myr corresponds to the onset of folding. Results show that in model (B), growth strata initially display deposition of strata with nearly constant thickness (yellow beds), followed by a gradual thinning upward patterns on timelines toward the crest of the structure (tan beds). An unconformity develops after 3.5 Myr. In model (C), on the other hand, growth strata display a shorter period of virtually constant-thickness sedimentation, followed by the development of a progressive unconformity, and finally, onlap patterns after 3.5 Myr.

The discrepancy detailed above can be understood in terms of a delay in the sedimentary response to folding (Tucker and Slingerland, 1996; Contreras, 2010; Allen and Heller, 2012 and references therein). The model in Figure 20 explains the key idea.

It shows that growth strata are deposited conformably in the initial stage of fold development, which results in the deposition of successions of virtually constant thickness that are indistinguishable from the pre-kinematic strata. The model also shows that as folding progresses, the rate of degradation increases and the thickness of growth strata decreases, which results in thinning-upward patterns toward the crest of the structure. Subsequently, a progressive unconformity appears on the crest, and bundles of strata with onlap geometries are laid down on the limbs of the fold.

Our model matches the observations made in the MRFB (Figs. 2, 10 and 20). In figure 10 we have identified for folds 3 and 7 the pregrowth/growth limit according to the excess area method; in the figure we have also identified as well the stratigraphic surfaces that mark the development of stacking geometries (onlap surface and thinning upward pattern). Notice that the pregrowth/growth limit lies ~1.3 s of TWTT (~2.5 km; Fig. 12) below the onlap/thinning-upward surfaces. What is more, these horizons are separated by a stratigraphic package of practically constant thickness as the model predicts. Thus, stacking geometries do not develop instantaneously; instead there is a lag time between the beginning of deformation and the development of stratal geometries.

We estimate now the lag time between folding and sedimentation based on the chronostratigraphy proposed by Salamón-Mora et al. (2009) and Alzaga-Ruíz et al. (2009) for the MRFB. Our calculations, however, likely contain large uncertainties because of the limited stratigraphic control. In the western part of the belt (folds 1-5 in Fig. 2), onlap geometries are observed around horizon 17 (Upper Miocene-Lower Pliocene boundary; Figs. 9, 10a). However, as stated above, our analysis indicates that the beginning fold growth occurred on average around deposition of horizon 15 (Late Miocene, Fig. 9). If we assume a constant sedimentation rate during the Late Miocene, the time elapsed between fold growth and development of onlap is in the order of 1.5 Myr. In contrast, in the eastern part of the belt (folds 6-12 in Fig. 2), thinning upward geometries are observed around deposition of horizon 18 (Lower Pliocene-Plio-Pleistocene boundary; Figs. 9 and 10b). Thus, it took an additional 1.7 Myr for this thinning upward pattern to develop with respect to the onlap observed in the western part of the MRFB. The delay in the eastern part of the MRFB was in the order of 3 Myr.

The delay documented here is in good agreement with analyses in other foreland basins, resulting in lag times in the order of 10^5-10^6 yr in the response of sedimentation to tectonics (Allen and Heller, 2012). For example, simulations of sediment fluxes carried out by Tucker and Slingerland (1996) in similar tectonic environments reveal lag times of about 400,000 years.

3.7.3. Implications for mass transport processes and topographic evolution

The excess-area method is a more robust estimator of the onset of folding than stacking patterns because excess area is directly related to mass transport. To see why, we need to consider the following relation describing erosion rate

$$\frac{\partial z}{\partial t} = -\frac{1}{\rho}\frac{\partial j_m}{\partial x} + s, \tag{10}$$

where z is the elevation of the topography with respect to an arbitrary datum (*e.g.,* the synclines) and j_m is the superficial mass transport (Eqn. 7). If we assume s is constant, and upon integration of relation (3.9) along the fold wavelength we obtain

$$\dot{A}_e = \int_{-L/2}^{L/2} \frac{\partial z}{\partial t}\, dx = -\frac{2}{\rho} j_m(L/2) + sL. \tag{11}$$

In this last expression, $\dot{A}_e$ is the rate at which excess area is lost due to erosion, and $j_m(L/2)$ is the superficial mass transport leaving the fold through the synclines. Upon further integration of equation (10), now with respect to time, we can finally obtain A_e. What is important, however, is that A_e is directly related to superficial mass transport. Moreover, from equation (7) it can be appreciated that j_m is not a function of time and, consequently, A_e is not affected by lag times.

The main simplifying assumption behind our results of the degradation of the topography is that the folded seabed is in steady state. This is a rather constrictive condition because such a state requires folds accrued structural relief at a constant rate, and a constant climatic forcing, which further implies constant erosion and sedimentation

through time (Whipple, 2001; Willett and Brandon, 2002). In this regard, we have shown in preceding paragraphs the areal relations of growth strata provide constraints on the rates at which uplift, erosion, and sedimentation operate since A_e is the net effect of slip consumed by folding and changes in primary stratigraphic thickness brought about by superficial mass transport (Fig. 20 and Eqn. 10). Moreover, experimental results and observations in natural detachment folds (*e.g.*, González-Mieres and Suppe, 2011; Schlische et al., 2014) demonstrated excess area relations for sedimentary units deposited under constant deformation and sedimentation rates lie in a smooth and continuous, monotonically decreasing curve with respect to A_e not unlike those in the models illustrated in Figure 20, whose equation assume precisely these conditions (Contreras, 2010). In spite of the limited resolution of the temporal information, the observational data for the growth strata in the MRFB shown in Figure 12 follow this general trend hinting that the assumptions underlying our results are reasonable. Conversely, abrupt changes in both thickness and shape of strata deposited in non-equilibrium conditions (*i.e.*, episodic growth and change in climatic forcing) result in a convolved curve recording the dynamics of the interplay between erosion, sedimentation, and deformation (González-Mieres and Suppe, 2011; Schlische et al., 2014).

Finally, we would like to point out that even though the overall seafloor topography of the MRFB appears smooth, which is characteristic of continuous erosion by diffusion, we noticed in section 3.6.1 that the degradation of the topography is controlled by mass wasting processes at the crests of the anticlines. During early fold growth, highly mobile, fine-grain sediments accumulate on their crests. As fold growth continues, interlimb angles increase, and gravitational instabilities develop, the sediments tend to be removed by slumping, grain flows and by a range of gravity processes (Morley, 2007 and references therein). Previous independent studies demonstrate that the values of k reported here are characteristic of rapid episodic mass movements (Martin and Church, 1997). Therefore, these values are in agreement with the general context of the deposition of sediments in deep-water foldbelts, which further validates our results.

3.8. Conclusions

The MRFB is a contractional deformation system comprising a series of fault-related folds across the continental slope of the western GOM. The structures located proximal to the continental slope are asymmetric, back-thrust anticlines, whereas the distal structures are symmetric, low-amplitude detachment folds.

Excess-area measurements for each of the thrust-related folds allowed us to reconstruct the deformation of the MRFB and QES (Fig. 19). The geometrical analysis indicates rheological contrasts in the stratigraphy gave rise to a regional detachment surface located at the Lower Eocene-Upper Eocene boundary (horizon 5; Fig. 12 and 19). We estimate the linear shortening across the foldbelt is 11.8 km. This value also corresponds with the total extension in the QES. The anticlines have wavelengths that fluctuate from 5800 to 10300 m and a combined length of 99 km, whereas the length of the undeformed section is ~111-km. Taking into account the length of the QES section (~30 km, including the rollover developed in the hanging-wall block), the initial length of the entire extensional-compressional system amounts to ~140 km (Fig. 2 and 19).

We also documented lateral changes in fundamental kinematic parameters across the MRFB. In general, parameter values tend to decrease with distance from the continental slope to the distal parts of the foldbelt. The linear strain accommodated by the folds is ~15% near the QES but drops to a value of ~10% in the distal parts of the MRFB. The tectonic uplift rate, v_u, changes from ~0.04 to ~0.39 mm/yr. The mass diffusivity constant, k, varies from ~0.19 to ~0.87 m^2/yr. The sedimentation rate, s, varies from ~0.18 to ~0.32 mm/yr (Figs. 13, 15, 16 and 18).

By combining our analysis with chronostratigraphic information from previous authors (Salomón-Mora et al., 2009; Alzaga-Ruíz et al., 2009), we established that the onset of folding occurred in a single event during the Upper Miocene throughout the MRFB at ~8 Myr, though our estimation likely contain a significant error due to large stratigraphic uncertainties. Moreover, our analysis reveals a lag time in the development of growth strata. The development of growth strata is relatively fast in the folds near the Tuxpan continental shelf, which are being uplifted rapidly and degraded vigorously. Under these conditions, the stratigraphic relations tend to give only a broad estimate of the limit

between pre-tectonic and syntectonic successions when compared to the excess-area method, which is more accurate. On the other hand, the development of growth strata took twice as much time for folds near the abyssal plain, which are being uplifted at a slower rate and where degradation is less intense. Consequently, the delay takes there considerably more time, and the use of stratigraphic relations introduce an even more pronounced bias toward younger ages in the identification of the onset of folding.

Chapter 4

Fold scaling laws and the wavelength selection during folding instability derived from Fourier analysis.

4.1. Introduction

Folds are complex structures that generally develop in layered media with strong rheological contrast among their layers. When strata is subjected to compression in a direction tangent to the layers, a periodic bending instability occurs, whose amplitude grows rapidly with time forming a train of material waves (Biot, 1961,1964; Smith, 1977). Initially, folds have low dip-angle limbs with a small amplitude-wavelength ratio. As shortening increases, ductile rocks flow toward the core of the structures, giving way to limb rotation and hinge migration, resulting in an increase of the dip-angle limbs, from the basal layer to the crest of the fold.

Harmonic analysis is a powerful tool in the analysis of fold growth. Indeed, the curve describing a folded surface can be analyzed by means of the Fourier transform. Several authors have used this method to quantify fold geometry (Biot, 1961; Norris, 1963; Harbaugh and Preston, 1965; Whitten, 1966; Chapple, 1968; Stabler, 1968; Hudleston, 1973; Stowe, 1988; Singh and Gairola, 1992; Srivastava and Gairola, 1997; Bastida et al., 1999; Tripathi and Gairola, 1999; Fossen, 2010). This approach, however, has been overlooked in the literature in favor of the so-called toy models, in the sense of trying to reduce the fold growth to its essential behavior (Suppe, 2011 and references therein). These models do not attempt to include all the complexities and the real forms of the folds, but rather focus on the study of simplified forms of the mass/layer-length balance equation.

In this study we analyze the seismic section of the Mexican Ridges fold belt (MRFB) presented in chapter 3, and derive from simple harmonic analysis, mathematical functions describing the folding process. We also derive fold scaling laws and document the process of wavelength selection during fold development using Fourier transform. Scaling laws are simple relations that illustrate the behavior of different variables of a

system depending on other parameters describing its size or shape. Despite their simplicity, these relations capture many of the essential attributes of a system that at first glance may seem complex. In general, fold scaling laws allow us to determine changes occurring during fold growth.

The MRFB is an important contractional deformation system located in the continental slope of the western Gulf of Mexico basin (GOM; Bryant et al., 1968; Garrison and Martin, 1973; Buffler et al., 1979; Alzaga-Ruiz et al., 2009; Salomón-Mora et al., 2009; Yarbuh and Contreras, 2015), which is thought to harbor up to 50 billion barrels of oil. Thus, it is of strategic importance to Mexico to understand the fold growth process, to further test the position of source rocks, migration routes, and the formation of structural traps (Buchanan, 1996). In this particular geologic setting, anticlines grow due to gravitational forces acting in the continental shelf, which gave rise to the Quetzalcoatl extensional system (QES; Román-Ramos et al., 2001, 2004). As a result, Neogene siliciclastic sediments of the continental slope are decoupled from the underlying Paleogene successions and Mesozoic carbonates, accomodating a tectonic transport of ~12 km. Shortening is distributed along a single regional basal detachment surface located at ~6 km-depth consisting of overpressured shale material. This gave rise to a train of twelve consecutive buckle folds that developed synchronously during the Late Miocene. The MRFB have an average strain that ranges from 3% up to 15%, and structures grow at rates of ~0.21 mm/yr (Yarbuh and Contreras, 2015).

4.2. Fourier analysis of folded structures

A Fourier series consists of an infinite series of trigonometric terms. Because of the periodicity of trigonometric functions, this series is useful in the investigation of several periodic physical phenomena including folds (Tripathi and Gairola, 1999 and references therein). More formally, the Fourier series decomposes any periodic function into a set of simple oscillating functions, namely sines and cosines, which can be represented by:

$$f(x) = \frac{a_0}{2} + \sum_{n=1}^{\infty} [a_n \cos(\frac{n\pi x}{L}) + b_n \sin(\frac{n\pi x}{L})] \quad (12)$$

where a_n and b_n are constants, n is an integer and x is a variable with value between 0

and π.

For a quarter wavelength unit of a fold (Fig. 21; Stabler, 1968), which in the present work correspond to the half wavelength, $\frac{L}{2}$, all cosine terms, even number terms and the constant, a_0, are zero (Stabler, 1968) and the Fourier series then can be reduced to:

$$f_{(x)} = \sum_{n=1}^{\infty} b_n \sin(\frac{n\pi x}{L}) \quad (13)$$

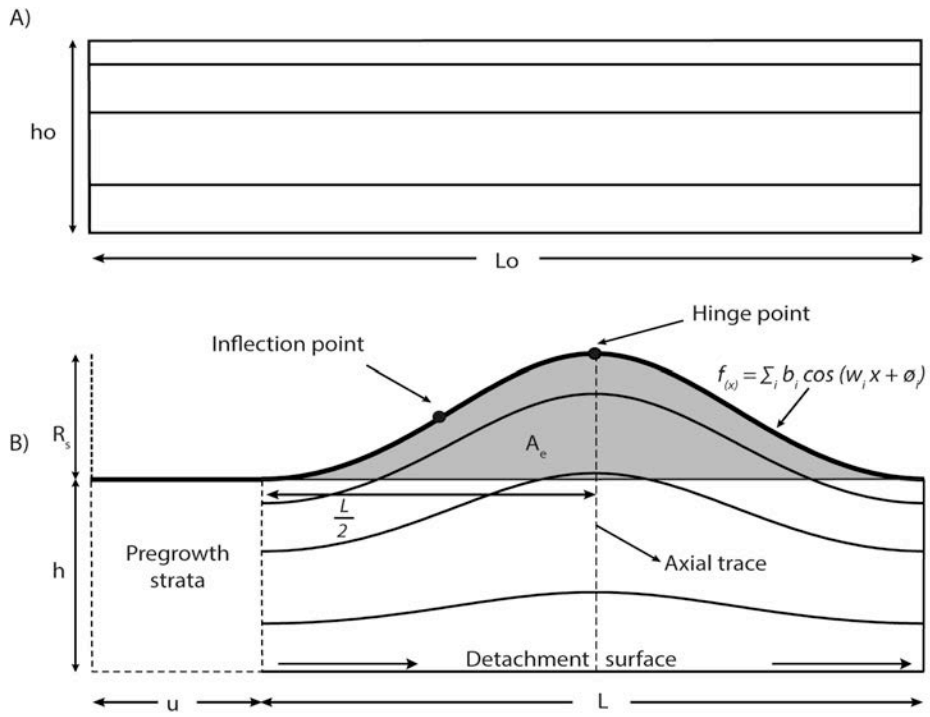

Figure 21. Sketch showing the geometrical parameters of detachment folds used in this work. (A) Succession of sedimentary layers initially has a planar geometry with initial dimensions h_0 and L_0. (B) A detachment fold is formed with a wavelength L. u is the shortening, the depth of the detachment surface is h, the excess area is A_e, and the amplitude is R_s. Notice the axial trace is the distance from $\frac{L}{2}$ to the hinge point. $f_{(x)}$ is the function describing the geometry of the folded strata, where b_i is the amplitude of each component of the cosine; w_i is a geometric coefficient ($w_i = 2\pi / L_i$) containing the wavelength, L; and ϕ_i is the phase angle of each wavelet containing the series.

Biot (1961) and Norris (1963) were the first authors to suggest the use of Fourier analysis for the study of folds. Since then, different methods and applications have been applied in the description of fold geometry, where a mathematical function is fitted to a given folded surface. This approach has proved useful in the classification of folds (*e.g.*, Harbaugh and Preston, 1965; Whitten, 1966; Chapple, 1968; Stabler, 1968; Hudleston,

1973; Stowe, 1988; Singh and Gairola, 1992; Srivastava and Gairola, 1997; Bastida et al., 1999).

This Fourier series will describe any fold shape between a point of zero curvature (inflexion point) and the point of maximum curvature (hinge point; see Fig. 21). Moreover, this series converges rapidly, so it is sufficient to consider only the first coefficients b_1 and b_3 in the description of folds. The series then becomes:

$$f_{(x)} \approx b_1 \sin\left(\frac{\pi x}{L}\right) + b_2 \sin\left(\frac{2\pi x}{L}\right) + b_3 \sin\left(\frac{3\pi x}{L}\right) \quad (14)$$

Hudleston (1973) used these Fourier coefficients to classify the profile shape of folded surfaces through a graphical representation of b_1 *vs.* b_3. Based on this method, this author came up with a visual classification system for fold shape, deriving six types of standard shapes, from types A (box folds) to F (chevron folds), and five standard amplitudes (Fig 5). Unfortunately, the use of two Fourier coefficients gives only a rough approximation to the functions that describe fold morphologies (Stowe, 1988; Aller et al., 2004), and offers no information about how those shapes came into existence.

The evaluation of the coefficients b_1 and b_3 in the Fourier series has been further dealt with by several workers (Stabler, 1968; Stowe, 1988; Srivastava and Gairola, 1997). Tripathi and Gairola (1999) concluded that symmetry of anticlines had been limited to a qualitative distinction between symmetrical or asymmetrical folds. In their analysis they bring forward quantitative measurements of the asymmetry of folds. With this information, they proposed a classification of folds based on a concept of the degree of asymmetry deduced from Fourier coefficients defining the shape and size of the two limbs of the fold.

Beyond this purely geometrical application, the theory of folding presented by Biot (1961) shows that during fold growth, a sharply defined wavelength is associated with the buckling instability. This wavelength grows at the fastest rate and is generally referred to as the dominant wavelength. After sufficient time, the dominant wavelength appears in the form of a more or less regular sinusoidal wave. The Biot's wavelength is function of the material properties and the thickness of the folded strata.

4.3. Methods

The key idea of the analysis presented here is as follows: consider a succession of layers initially having a rectangular geometry with initial dimensions h_0 and L_0, which is shortened to a distance u (Fig. 21). In response, rocks deform leading to a fold with amplitude R_s, which is the structural relief of the fold. Our objective now is to constrain the kinematics of fold growth using simple harmonic analysis, and derive from spectral analysis fold scaling laws and other analytical mathematical relations describing folding, and the process of wavelength selection during fold development.

The harmonic analysis was performed on the seismic data of the pregrowth strata section of the MRFB presented in chapter 3 (Fig. 22). The horizons subjected to Fourier analysis are those between the upper horizon, S_1, which marks the pregrowth-growth-strata boundary, and S_9, which correspond to the basal detachment surface. The spatial series have a length of 104-km and altogether form a succession of ~4 s thick measured in two-way travel time (TWTT), and is oriented NE-SW, perpendicular to the strike of the structures (Fig 22).

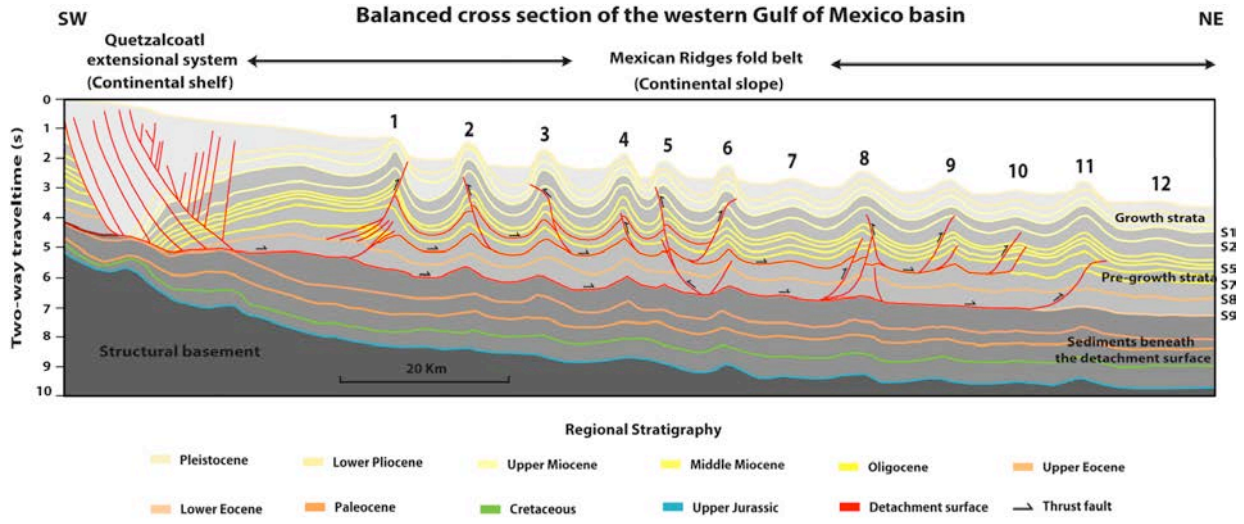

Figure 22. Balanced cross section of the MRFB. It consists of three successions: the dark gray color section corresponds to the structural basement of age previous to Jurassic; the middle gray color section comprises the sediments beneath the detachment surface of Upper Jurassic-Paleocene age; the light gray section is the fold train. Notice, the latter section includes the pregrowth strata, which are sediments deposited prior to folding, and the growth strata section, which are sediments deposited synchronously during folding. Layer S_1 marks the pregrowth-growth-strata boundary, and layer S_9 correspond to the basal detachment surface.

In Fourier analysis, equidistant data sampling is needed along the series. In our case we interpolated our spatial signal every 10 m, for a total length of 10401 data points. Because the MRFB is found in the continental slope of the GOM, and has a regional slope of ~3°, the folded layers were adjusted to a horizontal cero-reference axis. This is necessary in order to eliminate artifices in the Fourier analysis (Fig. 4), namely, zero wave numbers that concentrate energy of the regional slope.

The objective now, is to derive analytical mathematical functions describing the growth of the MRFB using the Fourier series as follows:

$$f_{(x)} = \sum_i b_i \cos(w_i x + \phi_i) \qquad (15)$$

where $f_{(x)}$ is the function describing the fold under analysis; b_i is the amplitude of each component of the cosine; w_i is a geometric coefficient ($w_i = 2\pi / L$) containing the wavelength, L; and ϕ_i is the phase angle of each wavelet containing the series. We first obtain the distribution of amplitudes, a_i, with respect the wave number using the fast Fourier transform algorithm (FFT). By creating amplitude-wave-number spectra, we are able to determine the dominant wave number, λ_x. The Biot's dominant wavelength, L_x, is simply the inverse of λ_x.

The spectral analysis was performed in two different ways. (1) We conducted a harmonic analysis at a foldbelt scale; and (2) spectral analysis for each of the folds making up the MRFB. The latter information allowed us not only to derive the dominant wavelength of the folds independently, but also to establish, on one hand, the relationship between the amplitude, R_s, and the depth to the detachment surface, h, and, on the other hand, how R_s relates to linear strain, ε_x across the MRFB. Values of ε_x for each fold comprising the MRFB were derived in chapter 3. In addition to this analysis, we also use the resulting Fourier harmonic coefficients b_1 and b_3 to establish the general fold geometry based on the classification of folds proposed by Hudleston, 1973.

4.4. Results

We now describe all the parameters of the sinusoidal function, $f_{(x)}$, described in Eqn. 15, yield by our harmonic analysis. First, we obtain the dominant wavelength, L_x, of the fold train. The energy-wave-number spectra of the spatial series are shown in Figure 23a. Specifically, we plotted the power spectral density (PSD), which tells us how power is distributed over the wave number components (Fig. 23a). The resulting PSD distribution shows that power is concentrated at a dominant wave number, λ_a = 0.1058 (km^{-1}), which corresponds to a dominant wavelength, L_a, of 9.4 km for the entire MRFB. Also, in the energy-wave-number spectra, we observe a second maximum concentration of energy at the wave number λ_b = 0.125 (km^{-1}), which corresponds to a second dominant wavelength, L_b of 8.0 km. Further note that the peak corresponding with the wave number λ_e = 0.0096 (km^{-1}) is the wavelength of the entire fold belt (L_e = 104 km). Our graph also reveals that the energy of the fold train decreases with depth from S_1 to S_9 (Fig. 23a), yet the maxima peaks in PSD corresponding with wave numbers λ_a and λ_b remain invariant with depth. That is, bed shape is similar in the direction of the axial trace. Such folds are called harmonic, whereas those in which wavelength and shape change along the axial trace, or die out in this direction are said to be disharmonic (Fossen, 2010).

The second parameter in Eqn. 15 is the phase. The resulting phase spectrum of the spatial series of the entire MRFB is shown in Figure 23b. In this figure we plotted the phases values from our Fourier analysis *vs.* the wave number. The corresponding phase for the dominant wavelength, L_a, is ϕ_a = 2.2, whereas the second dominant wavelength, L_b, has a phase, ϕ_b *of* 0.14 (Fig. 23b). This means that these two wavetrains are in close constructive interference, and the effects of disharmonic and lift-off layers are not observed in the structures of the MRFB. Good examples of the latter effects are observed in the Jura Mountains, where the structural style corresponds with a high-strain disharmonic foldbelt (Mitra, 2002 and references therein).

The third parameter in Eqn. 15 is the amplitude, R_s. Since the Fourier transform returns energy values for each wave number (Fig. 23a), it is necessary to apply the inverse Fourier transform for both λ_a and λ_b in order to obtain the amplitude of each term, a_i, in

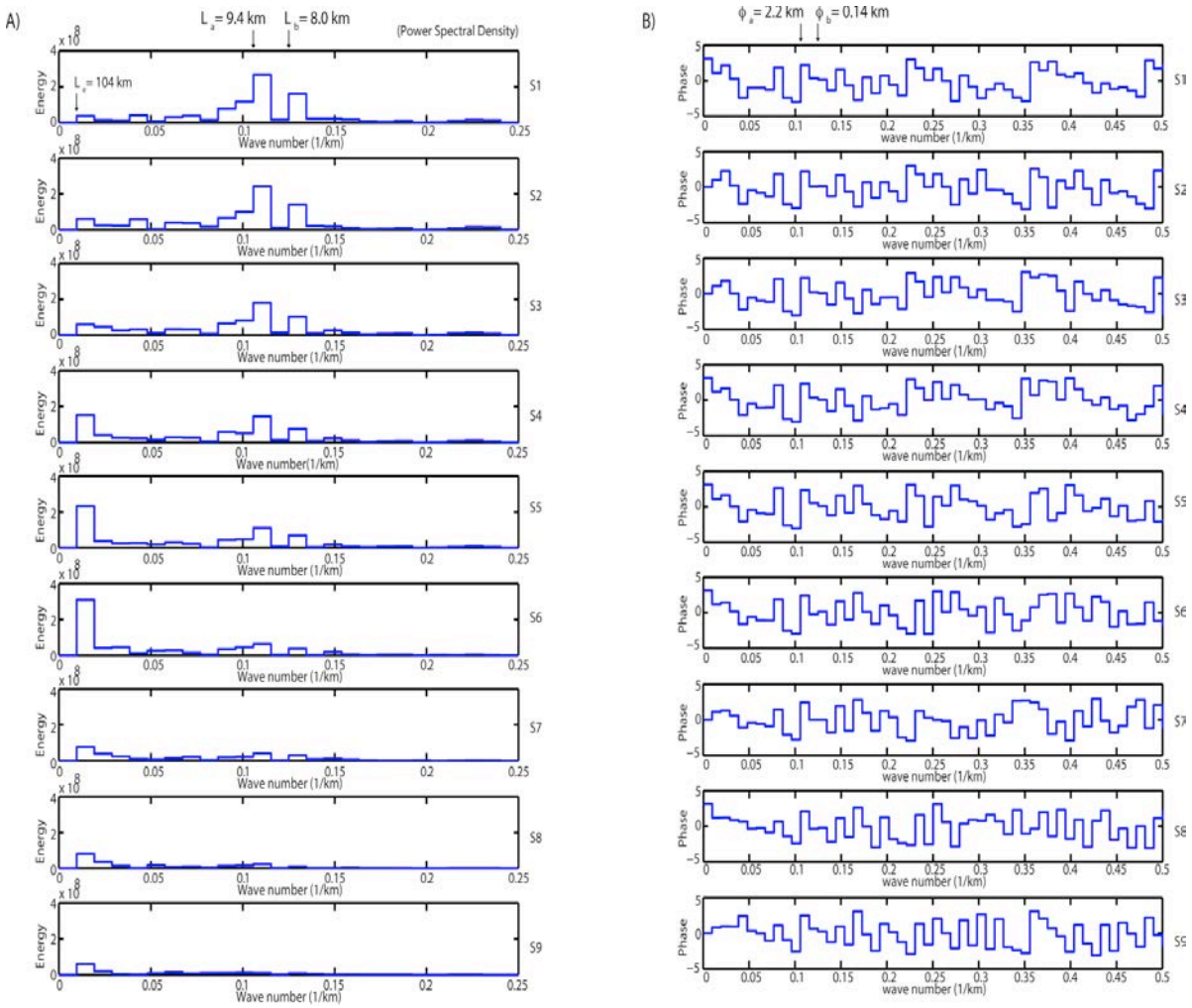

Figure 23. (A) Power spectral density spectra and (B) phase spectra for each of the series comprising the pregrowth section of the MRFB (see Fig. 4.3).

the series (Fig. 24). For the series containing the dominant wavelength, L_a, we observe the amplitude ranges between 0.2 to 1.0 s of TWTT (Fig. 24), whereas for L_b, amplitude varies from 0.1 to 0.5 s of TWTT (Fig. 24). We observe amplitude decreases monotonically with depth from S_1 to S_9 (Fig. 24; see discussion below). Here, we do not attempt to show the all the functions describing folding for each series $S_{1\text{-}9}$. However, we would like to show as an example the relation, $f_{(x)}$, for the series S_1, which is the most representative layer of the entire foldbelt containing the highest amplitudes. The resulting functions for both the Biot's wavelength and the secondary wavelength are:

$$f_{(x1)} = \cos\ (0.66x + 2.2) \tag{16}$$

$$f_{(x2)} = 0.5\cos\ (0.78x + 0.14) \tag{17}$$

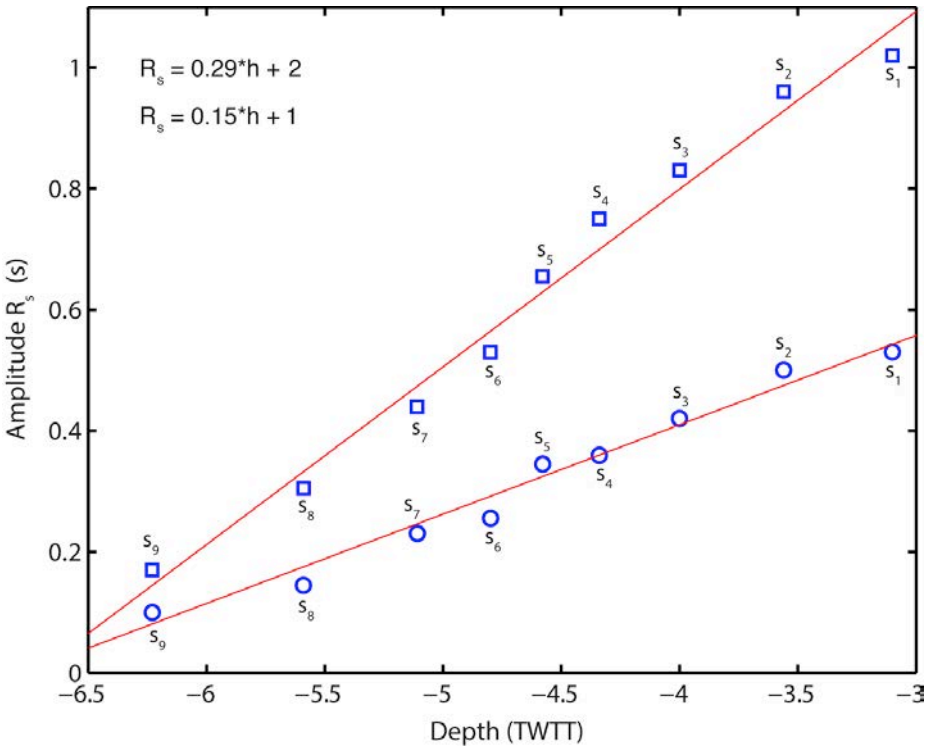

Figure 24. Plots of the amplitude, Rs, and the depth to detachment surface, h, for both the Biot's dominant wavelength and a closely related secondary wavelength. Notice the amplitude decreases from S_1 to S_9. Also notice that the slope of the linear relation is greater for the Biot's wavelength, suggesting that greater amplitudes carry greater energy.

In addition to the spectral analysis carried out at a foldbelt scale, we also perform the same spectral analysis for each isolated fold. In general, the dominant wavelength, $L_{1\text{-}12}$, ranges from 9.93 to 5.95 km. Amplitude ranges from 0.02 to 1.60 s of TWTT, where higher amplitudes correspond to S_1 and lower amplitudes correspond to S_9. Table I synthetizes our results.

In Figures 25 and 26 we show details of the Fourier analysis for folds number two and eight. We selected these two folds for further discussion because they are good examples of high-strain and low-strain detachment folds respectively, and thus give important clues of how fold shape changes with increasing strain (see discussion bellow). For fold number two, the amplitude, R_s, corresponding to the Biot's wavelength is in the order of 1.5 s. This is the value corresponding to the harmonic coefficient b_1 (Fig. 25a). The amplitudes corresponding to the harmonic coefficients b_2 and b_3 are 0.5 and 0.25 s of TWTT respectively. Figure 25b illustrates the phase values corresponding to the wave

Table 1. Summarize table of values of amplitude, wavelength and phase for each of the fold making up the MRFB.

	Fold 1	Fold 2	Fold 3	Fold 4	Fold 5	Fold 6	Fold 7	Fold 8	Fold 9	Fold 10	Fold 11	Fold 12
Layer S1												
Amplitude (s of TWTT)	1.3	1.6	1.3	1.1	0.7	0.9	0.4	0.9	0.6	0.2	0.8	0.2
Wavelength (km)	9.6	9.8	8.5	7.4	5.9	6.5	8.6	9.9	9.3	6.6	9.9	7.1
Phase	2.9	3.1	-3.1	2.5	-2.4	3.0	-3.1	-3.0	-3.1	-3.0	-2.9	-2.6
Layer S2												
Amplitude (s of TWTT)	1.5	1.5	1.1	1.1	0.7	0.8	0.4	0.9	0.6	0.3	0.9	0.2
Wavelength (km)	9.6	9.8	8.5	7.4	5.9	6.5	8.6	9.9	9.3	6.6	9.9	7.1
Phase	2.9	3.1	-3.0	2.5	-2.2	3.0	3.0	-3.0	-3.1	-3.0	-2.9	-2.7
Layer S3												
Amplitude (s of TWTT)	1.1	1.3	1.0	1.1	0.7	0.7	0.3	0.7	0.5	0.2	0.8	0.2
Wavelength (km)	9.6	9.8	8.5	7.4	5.9	6.5	8.6	9.9	9.3	6.6	9.9	7.1
Phase	3.0	3.0	3.0	2.5	-2.5	4.0	3.1	-3.0	3.1	-3.0	-2.9	-2.7
Layer S4												
Amplitude (s of TWTT)	1.0	1.1	0.9	1.0	0.6	0.5	0.3	0.7	0.5	0.2	0.7	0.2
Wavelength (km)	9.6	9.8	8.5	7.4	5.9	6.5	8.6	9.9	9.3	6.6	9.9	7.1
Phase	3.1	3.0	3.0	2.6	-2.7	3.0	-3.0	-2.9	3.0	-3.0	-2.9	-3.0
Layer S5												
Amplitude (s of TWTT)	1.0	1.1	0.7	0.8	0.6	0.4	0.3	0.5	0.4	0.2	0.7	0.1
Wavelength (km)	9.6	9.8	8.5	7.4	5.9	6.5	8.6	9.9	9.3	6.6	9.9	7.1
Phase	-3.1	3.0	-3.1	2.5	-2.7	2.8	3.0	-3.0	-3.1	-3.0	-2.9	-2.7
Layer S6												
Amplitude (s of TWTT)	0.8	0.7	0.6	0.6	0.5	0.5	0.2	0.5	0.3	0.2	0.7	0.1
Wavelength (km)	9.6	9.8	8.5	7.4	5.9	6.5	8.6	9.9	9.3	6.6	9.9	7.1
Phase	-2.9	3.0	3.1	2.3	-3.0	2.8	3.0	-2.9	3.1	-2.7	-2.8	-3.1
Layer S7												
Amplitude (s of TWTT)	0.3	0.7	0.6	0.6	0.3	0.5	0.2	0.4	0.3	0.1	0.5	0.1
Wavelength (km)	9.6	9.8	8.5	7.4	5.9	6.5	8.6	9.9	9.3	6.6	9.9	7.1
Phase	-2.6	3.1	-3.0	2.6	-3.0	2.7	3.0	-2.6	3.0	3.0	-2.8	-3.0
Layer S8												
Amplitude (s of TWTT)	0.1	0.5	0.5	0.5	0.1	0.4	0.2	0.3	0.2	0.1	0.2	0.1
Wavelength (km)	9.6	9.8	8.5	7.4	5.9	6.5	8.6	9.9	9.3	6.6	9.9	7.1
Phase	-1.6	-3.0	-3.0	2.1	2.1	2.7	2.6	-3.1	3.0	2.9	-2.9	-1.9
Layer S9												
Amplitude (s of TWTT)	0.06	0.47	0.4	0.39	0.14	0.34	0.07	0.21	0.02	0.04	0.22	0.02
Wavelength (km)	9.6	9.8	8.5	7.4	5.9	6.5	8.6	9.9	9.3	6.6	9.9	7.1

number distribution. Observe the value of ø varies for each corresponding wave number. The first coefficient is ~π, the second coefficient is ~0, and the third coefficient is ~ -π. As we will see, these values are of importance in describing fold growth. We were able to reconstruct the folding functions based on the values of the harmonic coefficients b_1, b_2 and b_3 shown in Figure 25 and 26. The resulting function, $f_{(x)}$, for fold number two is shown in Figure 4.6c. Notice the fold has an absolute ratio b_3/b_1 of ~0.167. According to Hudleston (1972), negative values of this ratio correspond to cuspate-lobate structures (Ramsay, 1967), in which synclines are broad and flat-bottomed whereas anticlines exhibit pinched crests (Smith, 1979). Analogously, for fold number 8 (Fig. 26), the amplitude corresponding to the Biot's wavelength is in the order of 0.9 s. Once again, this is the value of the harmonic cefficient b_1 (Fig. 26a). The amplitudes corresponding to

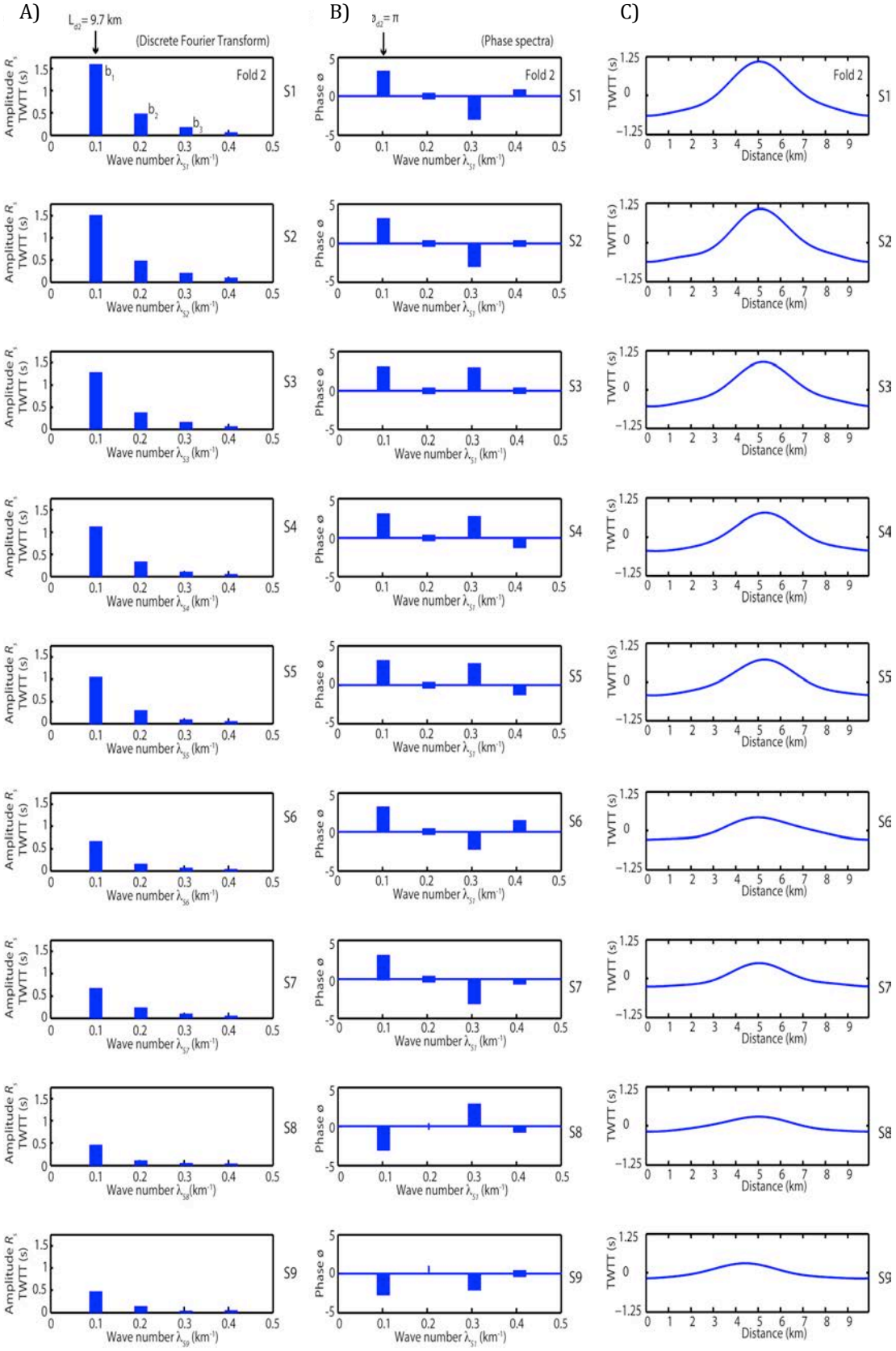

Figure 25. (A) Amplitude-wave-number spectra of folded layers for Fold No. 2 (see Fig. 4.2), and (B) its corresponding phase-wave-number spectra. (C) Resulting sinusoidal function of each layer making up Fold No. 2.

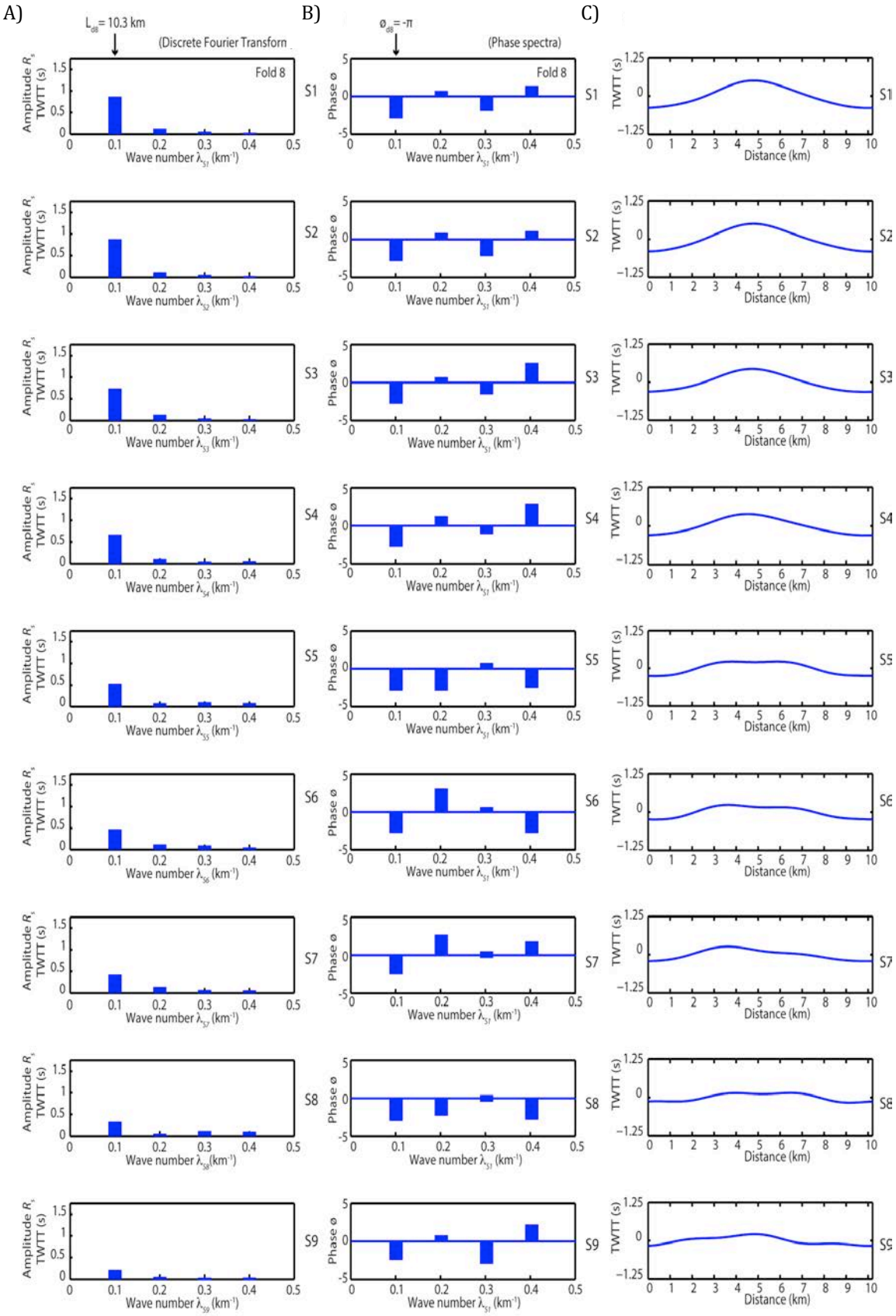

Figure 26. (A) Amplitude-wave-number spectra of folded layers for Fold No. 8 (see Fig. 22), and (B) its corresponding phase-wave-number spectra. (C) Resulting sinusoidal function of each layer making up Fold No. 8.

the harmonic coefficients b_2 and b_3 are 0.1 and ~0 s of TWTT respectively. Clearly, in this latter case such small coefficients do not contribute in further construction of the fold shape. This fold, thus, exhibit a strong sinusoidal geometry (Hudleston, 1972). Also observe that values of ø varies from ~ 0 to ~π (Fig. 26b). Once again, with the information in the wave-number spectra, we were able to construct functions for each of the harmonic coefficients b_1, b_2 and b_3 (Fig. 26c).

To further illustrate the behavior of the folds with respect to depth, *h*, and how amplitude varies with respect to the linear strain, ε_x, we now plot the values of R_s against *h* and ε_x for the twelve fault-related folds using log-log diagrams (Figs. 27 and 28). Results show that amplitude, R_s, increases along the axial trace following a linear relation between R_s and *h* (Fig. 27). Similarly, it can be observed in Figure 28, amplitude increases linearly with strain. Thus, R_s scale both as

$$R_s \sim h \tag{18}$$

$$R_s \sim \varepsilon_x. \tag{19}$$

4.5. Discussion

In general, fold growth is governed by two phenomena: (1) the degree of amplification, *i.e*., the magnitude of the factor by which a certain wavelength amplitude initially present in the layer is multiplied after a given time; and (2) the selectivity of the amplification, which can be characterized by the bandwidth representing those wavelengths that are selectively amplified (Biot, 1961). Thus, to unravel the folding process we need to analyze these two phenomena separately. We begin our discussion by focusing on how fold amplitude grows as a function of size and strain (scaling laws Eqns. 18 and 19). These growths laws arise from the conservation of mass. To see why, consider the excess-area method (Chamberlin, 1910; Epard and Groshong, 1993; Groshong and Epard, 1994; Bulnes and Poblet, 1999 and references therein), which relates the area of uplifted beds and the height above a reference horizon and postulates that the area lost by shortening must be equal to the area uplifted by deformation

$$A_e = u \times h; \quad (20)$$

If we express $A_e = \gamma\ x\ R_s\ x\ L$, where γ is a non-dimensional constant related to the geometry of the fold. For example, for a chevron fold $\gamma \approx \frac{1}{2}$, whereas for a box fold $\gamma \approx 1$. These values will give the area of a triangle and a rectangle, respectively. On the other hand, our results indicate the dominant wavelength, L, is constant, in average, across the MRFB. Then, we can express the conservation of area relation (Eqn. 20) in the following way:

$$A_e = u \times h = \gamma\ x\ R_s\ x\ L; \quad (21)$$

From this relation we can conclude that $R_s \sim h$.

Our results also show that folds having greater strain, ε_x, result in greater amplitudes. Indeed, R_s, must also scale linearly with ε_x (scaling law Eqn. 19). If we re-arrange Eqn. 21 in the following way:

$$R_s = \frac{u \times h}{\gamma\ x\ L}, \quad (22)$$

and recalling that the linear strain $\varepsilon_x = u / L$, then we can conclude

$$R_s = \frac{\varepsilon_x\ x\ h}{\gamma} \quad (23)$$

Results demonstrate that the linear relations above are valid for structures with linear strain values up to 15%. For high-strain anticlines, the presence of space problems in the core of the structures and the formation of disharmonic folds and significant penetrative deformation (Mitra, 2002 and references therein) might result in a break down of this law. The upper limit at which it remains valid needs further investigation.

From the amplitude-wave-number spectra we observe that all folds making up the MRFB are expressed as harmonic series, in the sense that the wave-number distribution are integer multiples of the dominant wave number. We also have seen the amplitude

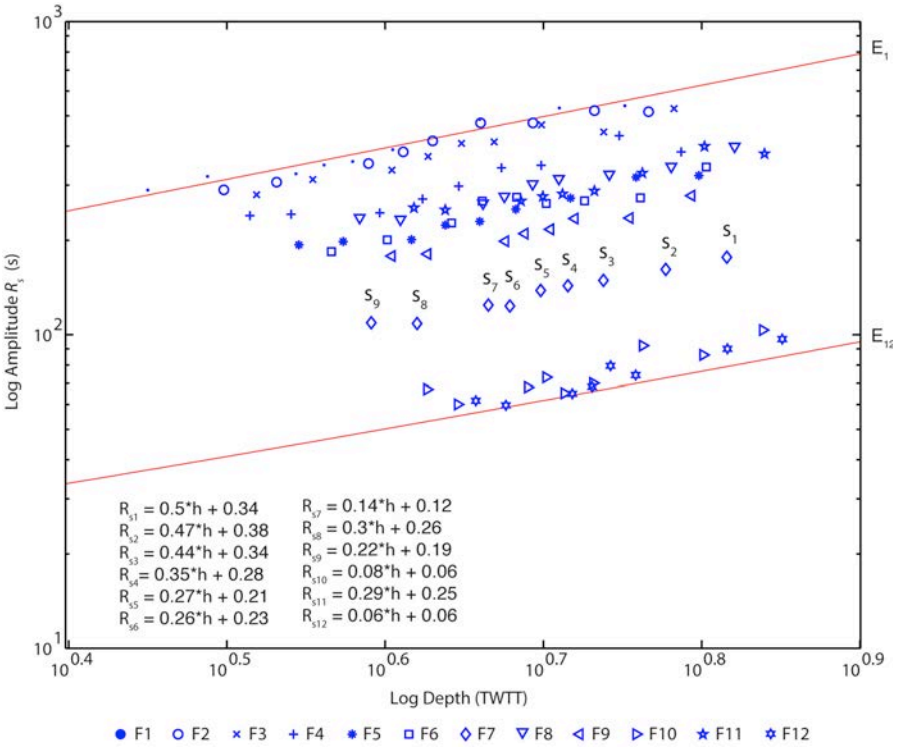

Figure 27. Summary diagram of the amplitude, R_s *vs.* the depth to the detachment surface, *h*, for each of the folds making up the MRFB, using the amplitudes obtained from the harmonic analysis. $F_{1\text{-}12}$ are the fold number label. $S_{1\text{-}12}$ are the layer labels. Plots also shows a best-fit linear model, which points out amplitude acquired by folding scales as the depth-to-detachment surface.

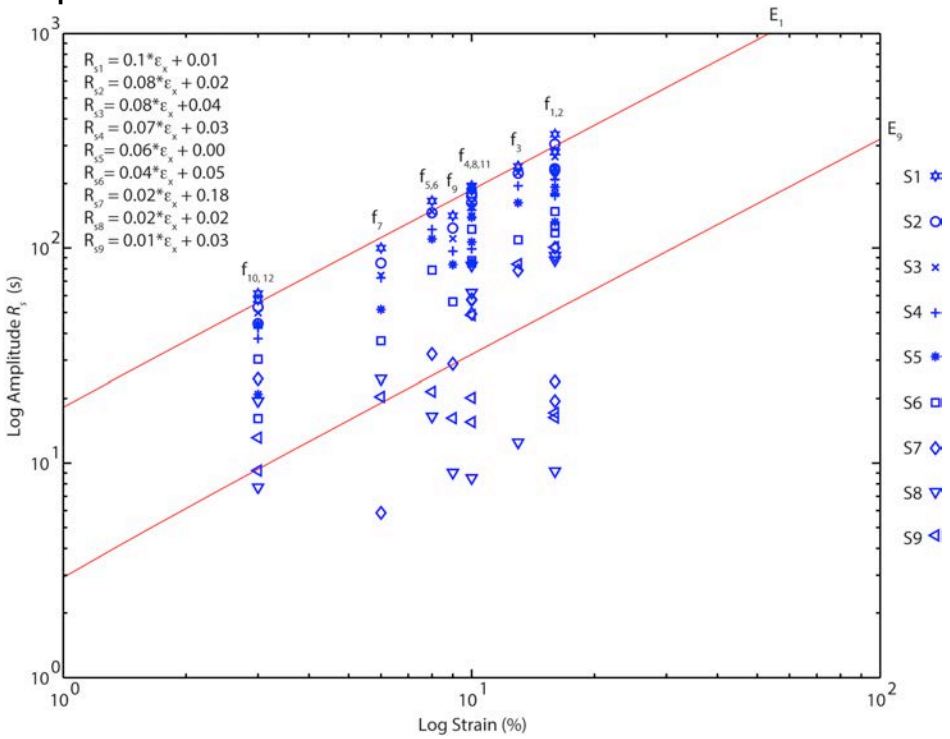

Figure 28. Summary diagram of the amplitude, R_s *vs.* the linear strain, ε_x, for each of the folds making up the MRFB. It is noteworthy that amplitude scales as the linear strain ε_x. Also notice that the slope of the best-fit line model decreases from ε_x~16 to 3%. $f_{1\text{-}12}$ are the fold number labels. $S_{1\text{-}12}$ are the layer labels.

corresponding to the Biot's wavelength contains almost all the energy of the folded surface. As strain increases, the amplitude corresponding to the second and third harmonic coefficients takes even more importance in the description of fold growth.

In the MRFB we observe two different shapes of fold: (1) folds 1-6 display cuspate-lobate geometry (ratio $b_3/b_1 \approx -0.167$), whereas (2) folds 7-12 exhibit sine-wave buckle folds (ratio $b_3/b_1 \approx 0$). These distinctive features develop from the contribution of the harmonic coefficients b_1, b_2 and b_3, which control the degree of hinge migration and limb rotation in the formation of these structures. For the first group of anticlines, where linear strain is the greatest (10-15%), the harmonic coefficients b_1, b_2 and b_3 introduce a positive interference in the core of the folding layers (Fig. 25). Here, limb rotation occurs primarily by flexural slip folding. Then, the folds eventually assume tight isoclinal geometries resembling lift-off folds (Mitra, 2002). The opposite occurs in the synclines, where destructive interference produce widening and the characteristic flat-bottomed geometry observed in the seismics. For the second group of anticlines, where linear strain is smaller (3-10%), only the harmonic coefficient b_1 takes relevance in the formation of folds (Fig. 26). Here, detachment folds originate with small wavelengths and hinge migration is the dominant deformation mechanism in their evolution (Dahlstrom, 1990).

4.6. Conclusions

The wavelength selection during folding instability derived from Fourier analysis is a powerful tool in the analysis of fold growth. Our results show, at a foldbelt scale, that the MRFB involves two dominant wavelengths. One is the Biot's wavelength of ~ 9.4 km, and another one is a closely related secondary wavelength of ~ 8.0 km.

At the individual structure scale, the harmonic coefficients b_1, b_3 control fold shape (ratios b_3/b_1). Additionally, we demonstrated the importance of the contribution of the harmonic coefficient b_2 in controlling fold shape. We found two different fold shapes evolved in the MRFB. Structures near the continental shelf correspond with cuspate-lobate anticlines, whereas structures in the continental slope, near the abyssal plain, correspond with sine-wave anticlines.

The main fold amplification mechanism for the first group of anticlines is limb rotation by flexural slip folding, leading to pinched crest structures. This might be attributed to the contribution of the harmonic coefficient b_2, whose influence grows with increasing linear strain and, on the other hand, hinge migration might be the dominant deformation mechanism in the evolution of the second group of anticlines, where none of the harmonic coefficients, b_2 nor b_3, contribute in the formation of the folds, and the linear strain is relatively low.

Finally, Fourier analysis results reveal that the amplitude increases along the axial trace following a linear relation between R_s and h. Similarly, it can be observed that amplitude increases linearly with strain. This is a growth law that arises from the conservation of mass. Yet, the selected wavelengths remain invariant with depth.

Chapter 5

General conclusions

5.1. Conclusions

We analyze a regional 2D seismic section of the Mexican Ridges foldbelt (MRFB), western Gulf of Mexico, and construct excess-area diagrams for each of the structures comprising the foldbelt to estimate shortening, the onset of folding, and the degradation of the folded seafloor. From the chronostratigraphy we derive rates of tectonic and superficial mass transport and illustrate how they change across the MRFB.

The resulting tectonic transport in the MRFB is 11.8 km forming a train of twelve buckle folds above a detachment at a depth of ~6s of two-way travel time, with an average strain of ~10%. The fold train grew at a mean uplift rate of ~0.21 mm/yr. Cross-sectional balancing demonstrates shortening balances the down-slip motion of the Quetzalcoatl extensional system (QES), suggesting horizontal compaction, volume loss, and other penetrative deformation mechanisms are negligible.

By assuming steady-state denudation, we are able to distinguish sediments derived locally from sediments transported from distant sources. The constant of mass diffusivity, a parameter controlling the degradation rate is ~0.42 m^2/yr, which is characteristic of rapid, episodic superficial mass movements. The combined sedimentation rate from both, local and distal sources is ~0.23 mm/yr. Those values are not constant; structures proximal to the continental shelf are rising rapidly and are being degraded more intensely than those in the distal part of the MRFB, where sedimentation outweighs tectonic uplift.

Our results indicate deformation initiated up to 3 Myr earlier than estimated from stacking patterns. Moreover, we find deformation started synchronously during the Late Miocene throughout the MRFB and not in two episodes as the stacking relations suggest. The discrepancy can be explained by a delay in the sedimentary response to folding. During early fold growth, nearly constant thickness strata are deposited before a

progressive unconformity and other converging geometries develop. The development of growth strata is fast in the folds near the QES, which are being uplifted rapidly and degraded vigorously. Under these conditions, the stratigraphic relations give only a broad estimate of the pre-tectonic/syntectonic limit when compared to the excess-area method. On the other hand, the development of growth strata took twice as much time for folds near the abyssal plain, which are being uplifted at a slower rate and where degradation is less intense. Consequently, the delay takes there more time, and the use of stratigraphic relations introduces an even more pronounced bias toward younger ages in the identification of the onset of folding.

The wavelength selection during fold growth derived from Fourier analysis show the MRFB involves two dominant wavelengths. One is the Biot's wavelength of ~ 9.4 km, and another one is a closely related secondary wavelength of ~ 8.0 km. The Fourier analysis carried out to each structure of the MRFB independently shows the harmonic coefficients b_1, b_2 and b_3 control fold shape. Initially, folds have low dip-angle limbs with a small amplitude-wavelength ratio. As strain increases, ductile rocks flow toward the core of the structures, giving way to limb rotation and hinge migration, which results in an increase of the dip-angle limbs, from the basal layer to the crest of the fold. We concluded two different fold shapes evolved out in the MRFB. On one hand, the structures developed near the continental shelf correspond with cuspate-lobate anticlines, in which the main fold amplification mechanism is limb rotation by flexural slip folding, the linear strain is relatively high, and the contribution of the harmonic coefficient b_2 takes relevance in the formation of the folds. On the other hand, the structures raised in the continental slope, near the abyssal plain, correspond with sine-wave anticlines, in which hinge migration might be the dominant deformation mechanism, the linear strain is relatively low, and where none of the harmonic coefficients, b_2 nor b_3, contribute in the formation of the folds.

Harmonic analysis is a powerful tool in the analysis of fold growth. Our results reveal that the amplitude increases along the axial trace following a linear relation between R_s and h. Similarly, it can be observed that amplitude increases linearly with strain. This is a growth law that arises from the conservation of mass. Yet, the selected wavelengths remain invariant with depth.

List of bibliographic references

Allen, P. A., and Heller, P. L. (2012). Dispersal and preservation of tectonically generated alluvial gravels in sedimentary basins. *Tectonics of Sedimentary Basins: Recent Advances*, 111-130. doi: 10.1002/9781444347166.ch6

Allmendinger, R. W. (1998). Inverse and forward numerical modeling of trishear fault‐propagation folds. *Tectonics*, *17*(4), 640-656.

Alzaga-Ruíz, H., Granjeon, D., Lopez, M., Seranne, M., and Roure, F. (2009). Gravitational collapse and Neogene sediment transfer across the western margin of the Gulf of Mexico: Insights from numerical models. *Tectonophysics*, *470*(1), 21-41. doi: 10.1016/j.tecto.2008.06.017

Bastida, F., Aller, J., and Bobillo-Ares, N. C. (1999). Geometrical analysis of folded surfaces using simple functions. *Journal of structural geology*, *21*(7), 729-742.

Biot, M. A. (1961). Theory of folding of stratified viscoelastic media and its implications in tectonics and orogenesis. *Geological Society of America Bulletin*, *72*(11), 1595-1620. doi: 10.1130/0016-7606(1961)72[1595:TOFOSV]2.0.CO;2

Bryant, W. R., Antoine, J., Ewing, M., and Jones, B. (1968). Structure of Mexican continental shelf and slope, Gulf of Mexico. *AAPG Bulletin*, *52*(7), 1204-1228.

Buchanan, P. G., and Warburton, J. (1996). The influence of pre-existing basin architecture in the development of the Papuan fold and thrust belt: implications for petroleum prospectivity. In *Petroleum exploration, development, and production in Papua New Guinea: PNG [Papua New Guinea] Chamber of Mines and Petroleum, PNG Petroleum Convention, 3rd, Port Moresby* (pp. 89-109).

Buffler, R.T., Shaub, F.J., Watkins, J.S. and Worzel, J.L. (1979). Anatomy of the Mexican Ridges, southwestern Gulf of Mexico, in J.S. Watkins et al, eds., Geological and geophysical investigations of continental margins: *AAPG Memoir* 29, p. 319-327.

Bulnes, M., and Poblet, J. (1999). Estimating the detachment depth in cross sections involving detachment folds. *Geological Magazine*, *136*(04), 395-412.

Butler, R. W. H., and Paton, D. A. (2010). Evaluating lateral compaction in deepwater fold and thrust belts: How much are we missing from “nature’s sandbox”?. *GSA Today*, *20*(3), 4-10.

Carson, M. A., and Kirkby, M. J. (1972). Hillslope form and process. Cambridge University Press, Cambridge.

Chamberlin, R. T. (1910). The Appalachian folds of central Pennsylvania. *The Journal of Geology*, 18(3), 228-251.

Chapple, W. M. (1968). A Mathematical Theory of Finite–Amplitude Rock–Folding. *Geological Society of America Bulletin*, *79*(1), 47-68.

Contreras, J., and Suter, M. (1990). Kinematic modeling of cross‐sectional deformation sequences by computer simulation. *Journal of Geophysical Research.* 21913-21929. doi: 10.1029/JB095iB13p21913

Contreras, J. (1991). Kinematic modeling of cross-sectional deformation sequences by computer simulation: coding and implementation of the algorithm. *Computers & Geosciences*, *17*(9), 1197-1217. doi: 10.1016/0098-3004(91)90024-8

Contreras, J. (2002). FBF: a software package for the construction of balanced cross-sections. *Computers & Geosciences*, *28*(8), 961-969. doi: 10.1016/S0098-3004(02)00019-5

Contreras, J. (2010). A model for low amplitude detachment folding and syntectonic stratigraphy based on the conservation of mass equation. *Journal of Structural Geology*, *32*(4), 566-579. doi: 10.1016/j.jsg.2010.03.006

Culling, W. E. H. (1963). Soil creep and the development of hillside slopes. *The Journal of Geology*, 71(2), 127-161.

EPARD, J. L., and GROSHONG JR, R. H. (1993). Excess area and depth to detachment. *AAPG Bulletin*, *77*(8), 1291-1302.

Dahlstrom, C. D. (1990). Geometric Constraints Derived from the Law of Conservation of Volume and Applied to Evolutionary Models for Detachment Folding: Geologic Note:(1). *AAPG Bulletin*, *74*(3), 336-344.

Davidson, J. P., and Davis, P. M. (1997). *Exploring earth: an introduction to physical geology*. Prentice Hall.

Erslev, E. A. (1991). Trishear fault-propagation folding. *Geology, v. 19*, p. 617–620.

Fiduk, J. C., Weimer, P., Trudgill, B. D., Rowan, M. G., Gale, P. E., Phair, R. L., and Queffelec, T. A. (1999). The Perdido Fold Belt, northwestern deep Gulf of Mexico, part 2: seismic stratigraphy and petroleum systems. *AAPG bulletin*, *83*(4), 578-612.

Fossen, H. (2010). *Structural geology*. Cambridge University Press.

Franco, S.I., Canet, C., Iglesias, A., and Valdéz-González, C. (2013). Seismic activity in the Gulf of Mexico. A preliminary analysis. *Bol. Soc. Geol. Mex*, *65*(3), 447-455.

Garrison, L. E., and Martin, R. G. (1973). *Geologic structures in the Gulf of Mexico basin* (p. 85). US Government Printing Office, Whashington.

González-Mieres, R., and Suppe, J. (2006). Relief and shortening in detachment folds. *Journal of Structural Geology*, *28*(10), 1785-1807. doi: 10.1016/j.jsg.2006.07.001

González-Mieres, R., and Suppe, J. (2011). Shortening histories in active detachment folds based on area-of-relief methods. In K. McClay, J. H. Shaw, & J. Suppe (Eds.), *Thrust fault-related folding* (pp. 39-67). AAPG Memoir 94. Tulsa, American Association of Petroleum Geologists. doi:10.1306/13251332M943428

Groshong JR, R. H., and Epard, J. L. (1994). The role of strain in area-constant detachment folding. *Journal of Structural Geology*, *16*(5), 613-618. doi: 10.1016/0191-8141(94)90113-9

Groshong JR, R. H., Withjack, M. O., Schlische, R. W., and Hidayah, T. N. (2012). Bed length does not remain constant during deformation: Recognition and why it matters. *Journal of Structural Geology*, *41*, 86-97. doi:10.1016/j.jsg.2012.02.009

Harbaugh, J.W., Preston, F.W., 1965. Fourier series analysis in geology. 6th Symposium on Computer Applications in Mineral Exploration, Tuscon, Ariz., R1-R46.

Hardy, S., and Poblet, J. (1995). The velocity description of deformation. Paper 2: sediment geometries associated with fault-bend and fault-propagation folds. *Marine and Petroleum Geology*, *12*(2), 165-176. doi: 10.1016/0264-8172(95)92837-M

Hardy, S., and Ford, M. (1997). Numerical modeling of trishear fault propagation folding. *Tectonics*, *16*(5), 841-854.

Hatcher JR, R. D. (2007). Confirmation of Thin-skinned Thrust Faulting in Foreland Fold-Thrust Belts and Its Impact on Hydrocarbon Exploration: Bally, Gordy, and Stewart, Bulletin of Canadian Petroleum Geology, 1966. *American Association of Petroleum Geologists Article*, *70034*(4).

Holl, J. E., and Anastasio, D. J. (1993). Paleomagnetically derived folding rates, southern Pyrenees, Spain. *Geology*, *21*(3), 271-274. doi: 10.1130/0091-7613(1993)021<0271:PDFRSP> 2.3.CO;2

Hubert‐Ferrari, A., Suppe, J., Gonzalez‐Mieres, R., &and WANG, X. (2007). Mechanisms of active folding of the landscape (southern Tian Shan, China). *Journal of Geophysical Research. 112*(B3). doi: 10.1029/2006JB004362

Hudleston, P. J. (1973). Fold morphology and some geometrical implications of theories of fold development. *Tectonophysics*, *16*(1), 1-46.

Jamison, W. R. (1987). Geometric analysis of fold development in overthrust terranes. *Journal of structural Geology*, *9*(2), 207-219.

Krueger, A., and Gilbert, E. (2009). Deepwater fold-thrust belts: Not all the beasts are equal. *AAPG Search and Discovery Article*, *30085*.

Laubscher, H. P. (1971). The large-scale kinematics of the western Alps and the northern Apennines and its palinspastic implications. *American Journal of Science*, *271*(3), 193-226. doi: 10.2475/ajs.271.3.193

Laubscher, H. P. (1977). Fold development in the Jura. *Tectonophysics*, *37*(4), 337-362. doi: 10.1016/0040-1951(77)90056-7

Le Roy, C., and Rangin, C. (2008). Cenozoic crustal deformation of the offshore Burgos basin region (NE Gulf of Mexico). A new interpretation of deep penetration multichannel seismic reflection lines. *Bulletin de la Societe Geologique de France, 179*(2), 161-174. doi:10.2113/gssgfbull.179.2.161

Le Roy, C., Rangin, C., Le Pichon, X., Ngoc, H. N. T., Andreani, L., and Aranda-Garcia, M. (2008). Neogene crustal shear zone along the western Gulf of Mexico margin and its implications for gravity sliding processes. Evidences from 2D and 3D multichannel seismic data. *Bulletin de la Societe Geologique de France*, *179*(2), 175-193. doi:10.2113/gssgfbull.179.2.175

Martin, Y., and Church, M. (1997). Diffusion in landscape development models: on the nature of basic transport relations. Earth Surface Processes and Landforms, vol 22, 273–279.

Mitra, S. (2002). Fold-accommodation faults. *AAPG Bulletin*, *86*(4), 671-694.

Morley, C. K. (2007). Development of crestal normal faults associated with deepwater fold growth. *Journal of Structural Geology*, *29*(7), 1148-1163. doi:10.1016/j.jsg.2007.03.016

Morley, C. K., King, R., Hillis, R., Tingay, M., and Backe, G. (2011). Deepwater fold and thrust belt classification, tectonics, structure and hydrocarbon prospectivity: a review. *Earth-Science Reviews*, *104*(1), 41-91.

Nemcok, M., Schamel, S., and Gayer, R. (2009). *Thrustbelts: Structural architecture, thermal regimes and petroleum systems*. Cambridge University Press.

Norris, D.K., 1963. Shearing strain in simple folds in layered media. *Geological Society of Canada Paper 63*, 26-27.

Poblet, J., McClay, K., Storti, F., and Muñoz, J. A. (1997). Geometries of syntectonic sediments associated with single-layer detachment folds. *Journal of Structural Geology*, *19*(3), 369-381. doi: 10.1016/S0191-8141(96)00113-7

Poblet, J., Bulnes, M., Mcclay, K., and Hardy, S. (2004). Plots of crestal structural relief and fold area versus shortening — A graphical technique to unravel the kinematics of thrust-related folds, in K. R. McClay, (Ed.), *Thrust tectonics and hydrocarbon systems* (pp. 372–399). AAPG Memoir 82. Tulsa, American Association of Petroleum Geologists.

Poblet, J. (2012). 2D Kinematic Models of Growth Fault-Related Folds in Contractional Settings. In C. Busby & A. Azor (Eds.), *Tectonics of Sedimentary Basins: Recent Advances* (pp. 538-564). John Wiley & Sons, Chichester. doi: 10.1002/9781444347166.ch27

Rangin, C., Le Pichon, X., Martinez-Reyes, J., and Aranda-Garcia, M. (2008). Gravity tectonics and plate motions: The western margin of the Gulf of Mexico Introduction. *Bulletin de la Societe Geologique de France, 179*(2), 107-116. doi:10.2113/gssgfbull.179.2.107.

Ramsay, J. G. (1967). *Folding and fracturing of rocks*. McGraw-Hill Companies.

Román-Ramos, J. R., Salomón-Mora, L. E., Aranda-García, M., Rosas-Lara, C. and Cárdenas-Dominguez, T. (2001). Structural styles and gasiferous potential at the western slope of the Gulf of Mexico (abs.): Cuarta Conferencia Internacional Conjunta Asociacio´n Mexicana de Geo´ logos Petroleros and AAPG, Veracruz, México, 6 p.

Román-Ramos, J. R., Salomón-Mora L. E., Rosas-Lara, C., Aranda-Garcia, M., Morales-Marin, J., Flores-Zamora, J. C., Sandoval-Solís, E. and Rosas-Lara, K. (2004). Depositional systems and traps of shallow and deep-water central Gulf of Mexico (abs.): AAPG Search and Discovery, http://www.searchanddiscovery.net/documents/abstracts/2004intl_cancun/index.htm #qr (accessed August 27, 2009).

Roure, F., Alzaga-Ruiz, H., Callot, J. P., Ferket, H., Granjeon, D., Gonzalez-Mercado, G. E., and Seranne, M. (2009). Long lasting interactions between tectonic loading, unroofing, post-rift thermal subsidence and sedimentary transfers along the western margin of the Gulf of Mexico: Some insights from integrated quantitative studies. *Tectonophysics*, *475*(1), 169-189.

Rowan, M. G. (1997). Three-dimensional geometry and evolution of a segmented detachment fold, Mississippi Fan foldbelt, Gulf of Mexico. *Journal of Structural Geology*, *19*(3), 463-480. DOI: 10.1016/S0191-8141(96)00098-3.

Rowan, M. G., Jackson, M. P., and Trudgill, B. D. (1999a). Salt-related fault families and fault welds in the northern Gulf of Mexico. *AAPG bulletin*, *83*(9), 1454-1484.

Rowan, M.G., Trudgill, B.D.,Weimer, P., and Fiduk, J.C., (1999b). Comparison of the Mississippi fan and Perdido deep water, salt-cored fold belt, northern Gulf of Mexico. *AAPG Bulletin*, *83*(8), 1296–1346.

Rowan, M. G., Peel, F. J., and Vendeville, B. C. (2004). Gravity-driven fold belts on passive margins.

Salomon-Mora, L. E., Aranda-Garcia, M., and Roman-Ramos, J. R. (2009). Contractional growth faulting in the Mexican Ridges, Gulf of Mexico. In C. Bartolini and J. R. Román Ramos (Eds.), *Petroleum systems in the southern Gulf of Mexico* (pp. 93-115). AAPG Memoir 90. Tulsa, American Association of Petroleum Geologist. doi:10.1306/13191080M903332

Salvador, A. (1991). Origin and development of the Gulf of Mexico basin. *The gulf of Mexico basin*, 389-444.

Schlische, R. W., Groshong JR, R. H., Withjack, M. O., and Hidayah, T. N. (2014). Quantifying the geometry, displacements, and subresolution deformation in thrust-ramp anticlines with growth and erosion: From models to seismic-reflection profile. *Journal of Structural Geology, 69, 304-319. In press.* doi: 10.1016/j.jsg.2014.07.012.

Shiner, P., Beccacini, A., and Mazzoli, S. (2004). Thin-skinned versus thick-skinned structural models for Apulian carbonate reservoirs: constraints from the Val d'Agri Fields, S Apennines, Italy. *Marine and Petroleum Geology*, *21*(7), 805-827.

Singh, R. A., and Gairola, V. K. (1992). Fold shape analysis in the vicinity of North Almora Thrust in district Chamoli, Garhwal Himalaya. *Journal of Himalayan Geology*, *3*, 121-129.

Smith, R. B. (1979). The folding of a strongly non-Newtonian layer. *American Journal of Science*, *279*(3), 272-287.

Srivastava, V. and Gairola, V. K. (1997). Classification of multilayered folds based on harmonic analysis: Example from central India. *Journal of Structural* Geology, 19(1), 107–112.

Stabler, C. L. (1968). Simplified Fourier analysis of fold shapes. *Tectonophysics*, *6*(4), 343-350.

Stowe, C. W. (1988). Application of Fourier analysis for computer representation of fold profiles. *Tectonophysics*, *156*(3), 303-311.

Suppe, J., Chou, G. T., and Hook, S. C. (1992). Rates of folding and faulting determined from growth strata. In K. R. McClay (Ed.), *Thrust tectonics* (pp. 105-121). Chapman & Hall, London.

Suppe, J. (2011). Mass balance and thrusting in detachment folds.

Suter, M. (1981). Strukturelles Querprofil durch den nordwestlichen Faltenjura, Mt-Terri-Randüberschiebung-Freiberge. *Eclogae geologicae Helvetiae* 74, 255-275.

Suter, M. (1991). State of stress and active deformation in Mexico and western Central America. *Neotectonics of North America*, *1*, 401-421.

Tripathi, A., and Gairola, V. K. (1999). Fold symmetry—a quantitative description. *Journal of structural geology*, *21*(7), 719-727.

Tharp, T. M., and Scarbrough, M. G. (1994). Application of hyperbolic stress-strain models for sandstone and shale to fold wavelength in the Mexican Ridges foldbelt. *Journal of Structural Geology*, *16*(12), 1603-1618. doi:10.1016/0191-8141(94)90130-9

Trudgill, B. D., Rowan, M. G., Fiduk, J. C., Weimer, P., Gale, P. E., Korn, B. E., Phair, R. L., Gafford, W.T., Roberts, G.R., and Dobbs, S. W. (1999). The Perdido Fold Belt, Northwestern Deep Gulf of Mexico, Part 1: Structural Geometry, Evolution and

Regional Implications1. *AAPG Bulletin*, *83*(1), 88-113.

Tucker, G. E., and Slingerland, R. (1996). Predicting sediment flux from fold and thrust belts. *Basin Research*, *8*(3), 329-349. doi: 10.1046/j.1365-2117.1996.00238.x

Vazquez-Meneses, M. E. (2005). *Gravity tectonics, Western Gulf of Mexico* (Doctoral dissertation, Royal Holloway, University of London).

Whipple, K. X. (2001). Fluvial landscape response time: how plausible is steady-state denudation?. *American Journal of Science*, *301*(4-5), 313-325. doi: 10.2475/ajs.301.4-5.313

Whitten, E.H.T., 1966. Structural Geology of Folded Rocks, 3rd ed. Rand McNally, Chicago.

Wiltschko, D. V., and Groshong, R. H. (2012). The Chamberlin 1910 balanced section: context, contribution, and critical reassessment. *Journal of Structural Geology*, *41*, 7-23.

Willett, S. D., and Brandon, M. T. (2002). On steady states in mountain belts. *Geology*, *30*(2), 175-178. doi: 10.1130/0091-7613(2002) 030<0175:OSSIMB> 2.0.CO;2

Yilmaz, Ö. (2001). Seismic data analysis (Vol. 1, pp. 288-318). Tulsa: Society of Exploration Geophysicists.